The Dissertation Committee for Senthil Prakash Theppakuttai Kom Certifies that this is the approved version of the following dissertation:

Laser Micro/Nano Scale Processing of Glass and Silicon

Committee:

Shaochen Chen, Supervisor

Michael F. Becker

John R. Howell

Li Shi

Gennady Shvets

Laser Micro/Nano Scale Processing of Glass and Silicon

by

Senthil Prakash Theppakuttai Kom, B.S.; M.S.

Dissertation

Presented to the Faculty of the Graduate School of
The University of Texas at Austin
in Partial Fulfillment
of the Requirements
for the Degree of

Doctor of Philosophy

The University of Texas at Austin
May 2006

Dedication

To my parents

Acknowledgements

First I would like to express sincere gratitude to my research advisor, Dr. Shaochen Chen, for his guidance, encouragement, and caring financial support throughout my graduate study at The University of Texas at Austin. To me, he has been more than an advisor: his vision, inspiration, support and helps in many ways have made my study here successful.

I would also like to thank Dr. Becker, Dr. Howell, Dr. Shi and Dr. Shvets for agreeing to serve in my dissertation committee and for their valuable feedback and comments. It has been a great pleasure to work and interact with my fellow graduate students of Dr. Chen's group. My appreciation goes to all the past and current students of Nano Optical Bio Engineering Laboratory.

I am deeply indebted to my parents and other family members for their love, blessing and understanding. They have always offered unconditional support and encouragement for my endeavors. Rather than simply appreciating their support, I would like to dedicate this dissertation to them.

Laser Micro/Nano Scale Processing of Glass and Silicon

Publication No._____________

Senthil Prakash Theppakuttai Kom, Ph.D.
The University of Texas at Austin, 2006

Supervisor: Shaochen Chen

The revolutionary progress in semiconductor, communication, and information industries based on electronic and photonic technologies demands for the development and enhancement of new laser processes to support micro and nanotechnologies. This dissertation is aimed at exploring the use of lasers for micro and nano scale processing of glass and silicon, the most commonly used materials in the IC industry. The objective of the dissertation is two fold: a) use lasers for locally micro bonding glass and silicon wafers, and b) use lasers for nanopatterning glass and silicon substrates by circumventing the diffraction limit of light.

In the first part of the thesis, glass and silicon wafers are bonded locally in microscale by a pulsed Nd:YAG laser. Glass is transparent to the wavelength used and hence the laser beam passes through the glass wafer and is absorbed by silicon. As a result, silicon is melted and upon resolidification bonding is realized between the two substrates. The transient melting and resolidification of the substrates is studied experimentally and compared to the simulation results of a finite element numerical model. The bonded areas are studied in detail using a scanning electron microscope and a chemical analysis is done to understand the bonding mechanism.

In the second part of the thesis, nanopatterns are created on glass and silicon substrates by circumventing the diffraction limit of light. The nanofeatures are created by irradiating silica and gold nanospheres deposited on a substrate. In case of silica spheres, features approximately half the diameter of the sphere were obtained by utilizing the optical field enhancement around the spheres. In case of gold spheres, features as small as 40 nm were realized by the excitation of coherent resonant electron plasma oscillations. The effect of sphere size, laser wavelength, polarization, incident angle, and energy were studied experimentally. Finally, these experimental results are compared with the numerical results from a multidimensional, heat transfer model.

Table of Contents

List of Tables

List of Figures

Chapter 1: Introduction

The beginnings of laser material processing dates back to the writings of science fiction such as '*The War of the Worlds*' by H.G. Wells, which was first published in 1898. Such stories sowed the seeds of a possible 'death ray' and after Einstein in 1916 had proved mathematically that stimulated emission was possible, the race was on to develop a 'death ray machine' or at least a device using stimulated emission. The military potential, sadly was the main driving force for research whose reward came in 1960 when Maiman invented the first working laser [1].

Soon after the invention of the first laser, several different types followed and they can be divided into different subgroups according to the principal type of operation and construction. From the material processing point of view, the solid-state lasers, like the Nd:YAG and the ruby laser, and gas lasers, like the helium-neon (HeNe), the argon-ion laser, the XeCl excimer laser, and high-power CO_2 lasers are the most important types. The remaining types, semiconductor lasers, liquid lasers, chemical lasers, color-center lasers, free-electron lasers and x-ray lasers, have more significance in the field of scientific research rather than in practical applications [2].

Laser processing of materials has become a field of growing importance with applications in mechanical engineering, such as drilling, cutting, bending, welding, cleaning, hardening, alloying and surface treatment; in electrical engineering and materials science, such as photolithography, ablation, thin film deposition, doping, annealing, recrystallization, defect scanning and mapping; in chemical engineering such as laser induced reaction, dissociation, photo-ionization; and in bioengineering, such as tissue cleaning and tissue removal.

1.1 LASER BEAM CHARACTERISTICS

As a light source, a laser beam offers several unique features for material processing. Monochromaticity is one of the unique characteristics of laser light. Perfectly monochromatic light cannot be produced even by a laser, but laser light is many times more monochromatic than the light from any other source. Since the absorption coefficient of different materials is highly wavelength dependent, by selecting the laser beam wavelength from deep ultra-violet to infrared, one can precisely control the material processing. Moreover, the processing depth can be controlled because the optical penetration depth depends on the wavelength, according to

$$L_{op} = \frac{\lambda}{4\pi k}, \tag{1.1}$$

where λ is the wavelength, L_{op} is the optical penetration depth and k is the extinction coefficient of the solid material [3]. This wavelength effect in beam focusing can be utilized to obtain a better focus of the laser beam without compromising too much on the depth of focus [4].

Coherent light waves all travel in the same direction (spatial coherence) at the same frequency and in phase (temporal coherence). This gives rise to a very narrow beam and intense, pure light that characterizes laser. The spatial coherence allows one to focus the beam very tightly. For a high-powered laser, this results in a very high energy density for laser ablation and thin film deposition [5] or material redistribution [6]. The ability to focus the laser beam down to micron level provides the means for precise laser processing in extremely small dimensions [7, 8]. For a low power probing laser beam, tighter focusing makes it possible to achieve “point detection” in surface diagnostics, providing a fine spatial resolution [9].

Another important characteristic of the laser beam is its very small divergence in the order of milliradians. The beam divergence determines the spot size. Higher the divergence higher is the spot size and vice versa. Arrangements of lenses are usually used to minimize divergence. The spot size is given by,

$$S = \theta f \tag{1.2}$$

where S is the spot size, θ is the beam divergence, and f is the focal length of the lens.

Moreover, the laser material interaction process is a non-invasive and clean "particle"-photon process. The non-contact nature permits non-vacuum processes which simplify the process itself, and enhances cost-effective manufacturing competitiveness. Robust processing can be achieved in laser micro-processing based on this non-contact nature. Since photons are primarily involved in laser processing, contamination from foreign particles, which are used as the principal etching source in other non-laser-based microfabrication techniques, and the possible contamination from machining tools and measurement errors due to the contacting elements is, greatly reduced [10].

The fact that lasers have found many applications in micro-scale processing is not only attributed to the above mentioned advantages, but also to the nature of the physical phenomenon driven by short pulse laser radiation. For most engineering materials used for laser processing, laser light is absorbed in a layer of a few nanometers to a fraction of a micron in thickness close to the surface. The absorbed energy is then dissipated into the material with a thermal diffusion length, *l*, according to: $l \sim \sqrt{\alpha \Delta t}$, where α is thermal diffusivity of the material and Δt is the laser pulse duration. Thus, shorter pulses will confine the thermal energy closer to the surface. By adjusting the pulse width, Δt, one can define the processing depth, which is very useful in microelectronics and microelectronics fabrication design.

With its unique ability to control micro-processing in lateral and depth dimensions, the pulsed lasers hold great promise in micro-manufacturing. Contrary to mechanical tools, laser micro-processing is not subject to wear and tear. In microelectronics and optoelectronics, pulsed lasers have been employed to deposit multi-element thin films such as YBCO superconductors and other oxides [11]. Pulsed laser annealing of ion implanted polysilicon films enhances electronic properties of TFT (Thin Film Transistor) devices [12]. Due to its localized nature, where the high temperature region is only confined in a very thin layer close to the surface, pulsed laser micro-processing is a low-substrate-temperature process which has tremendous attractiveness for applications in flat panel display and III-V optoelectronic devices. The short time scales lead to non-equilibrium processing of materials.

Pulsed lasers have also been used in submicron patterning [13], dry etching [14] and surface oxidation [15]. In micromechanics, with a very fast etching speed up to 30μm/s which is several orders higher than that by conventional plasma etching and wet etching, pulsed laser can be an efficient and cost effective tool for three-dimensional structuring of micro-mechanical devices such as micro-motors and micro-tweezers used in automobile and biomedical applications [16]. It is precisely because of this advantage that pulsed lasers can compete with many conventional etching technologies used in bulk micro-machining. On the other hand, even though X-ray micromachining is capable of generating aspect ratios as high as 1:1000 [17], X-ray 3D structuring can not provide a cost effective solution and convenience to industrial users since the operation has to be carried out in cyclotrons and exposure time is of the order of hours. The excimer laser, however, may provide an alternative method for high aspect ratio micromachining with acceptable industrial cost and fast operation even enough currently achieved aspect ratios are limited to 1:20, which is sufficient for many applications. In biomedical engineering, pulsed lasers have been successfully applied for corneal surgery [18] and intraocular surgery [19] taking great advantage of the accurate pulsed laser process control.

1.2 LASER MATERIAL INTERACTION

The fundamental understanding of laser interaction with materials has been a goal of intense research for the last few decades [20-22]. For metallic materials, the absorption of laser light is mainly dominated by free electrons, which are the non-localized outermost electrons shared by the positive ion lattice system. Free electron gas theory has been used to describe both optical and electronic properties of metallic materials. For insulators and semiconductors, the conduction band does not contain an appreciable population of free electrons as in metallic materials. Therefore, electrons in the valence band are expected to contribute to the electronic and optical response. The bandgap energy, E_g, between the conduction and valence bands defines the amount of energy needed to excite an electron from the highest level of the valence band to the lowest level of the conduction band. Insulators have larger E_g than that of semiconductors; however no distinct line can be drawn in terms of E_g for the two materials. For a single photon energy larger than the bandgap, i.e. $E_p > E_g$, electronic excitation can be realized by a valence electron absorbing a photon to become a conduction electron. For the photon energy lower than the bandgap, the laser beam will be either transmitted or reflected without substantial absorption, depending on the real part of the material's optical refractive index.

However, it should be pointed out that the above electronic excitation is limited to energy transfer only, which is the case for direct bandgap semiconductors such as GaAs and insulators where the conduction band minimum and valence band maximum are at the same point in k-space. There is no need to consider momentum transfer in direct bandgap materials since the electronic transition does not involve momentum changes between these two states. For indirect bandgap materials such as silicon where the conduction band minimum and valence band maximum are not at the same point in k-space, unless the laser photon energy is large enough to directly induce electronic excitation from the maximum level of the valence band to a level in the conduction band at the same value of momentum, electronic excitation from the maximum level of valence band to minimum level of conduction band requires both energy and momentum transfer. Even though a photon carries a quantum of energy, it does not have significant momentum, which is essential for the electronic transition in indirect bandgap materials. Additional momentum can be provided through quantized lattice vibration or "phonons", which are functions of lattice temperature. This phonon-assisted laser absorption is clearly influenced by the material temperature during processing.

Non-linear optical absorption is possible if new absorption sites are generated after the primary absorption has occurred. Multiphoton absorption can be realized at very high laser intensity, i.e. large photon density, where an electron absorbs two or more photons simultaneously and is thereby excited to the conduction band. Multiphoton absorption is desired in laser processing of wide band-gap semiconductor materials, where the photon energy is smaller than bandgap.

After absorbing a laser photon, excited electrons have to relax from higher energy level to lower energy level, usually through three paths. First, if the excitation leads to an energy level that is above the dissociation energy, materials will be dissociated at the very next vibration within a pico-second time scale. This is the so-called photo-chemical process which is most likely to happen for higher photon energy, i.e. shorter laser wavelength. In the second route, an excited electron relaxes through internal energy conservation to ground state. The electronic energy is rapidly (within order of 10^{-12} s) converted to vibrational or rotational energy in the lattice system, causing heating of the materials. This heating leads to thermal decomposition through melting and/or vaporization on the material surface, which has been referred to as the photo-thermal mechanism in laser interactions with materials. The third mechanism, the thermal-assisted photochemical process, is a combination of the above mentioned two mechanisms. Electrons are initially excited to excited states, where the energy level is not above the dissociation energy. A fraction of the excited electrons undergo photo-thermal process where their electronic energy is converted to thermal energy causing the temperature rise in materials. Other excited electrons can be further excited to higher energies than the dissociation energy by absorbing energetic photons generated by photo-thermal conversion, leading to thermal-assisted photo-dissociation. However, laser interactions with materials are complicated not only by the electronic structure, but also by the characteristics of the laser light, such as wavelength and polarization. In order to have a complete picture of laser interactions with specific materials, it is essential to understand fundamental interactions among photons, electrons and phonons in the specific material system.

1.3 MATERIALS OF CHOICE: GLASS AND SILICON

The excellent mechanical strength of silicon combined with the electrical insulation, chemical durability, and optical transparency of glass makes the silicon-glass couple the most employed material combination in MEMS. Another reason for this combination is the very small difference in coefficient of thermal expansion between glass and silicon [23].

The most widely used material in the semiconductor industry is Silicon, despite having the highest material cost per unit area. Silicon with or without passivating layers, due to its extreme flatness and well established coating procedures, often is the preferred substrate especially for thin films [24]. Silicon exhibits no plastic deformation of creep below 800^0C; therefore, silicon sensors are inherently very insensitive to fatigue failure when subjected to high cyclic loads. Silicon sensors have actually been cycled in excess of 100 million cycles with no observed failures. Silicon because of its intrinsic mechanical stability and the feasibility of integrating sensing and electronics on the same substrate is an excellent substrate of choice for many mechanical sensor applications [25]. Although the silicon band–gap is relatively narrow, by employing silicon on insulator (SOI) wafers, high temperature sensors can be fashioned [26]. For the latter application, heavily doped silicon which is relatively linear in its temperature coefficient of resistance and sensitivity over a wide range is used. Monocrystalline silicon has a high peizoresistivity and, combined with its excellent mechanical and electronic properties, makes a superb material for conversion of mechanical deformation into an electrical signal. In fact, the history of silicon-based sensors started with the discovery of the peizoresistance effect in Si and Ge more than four decades ago [27].

After silicon, glass is the second most widely used material in MEMS fabrication. The development of glass science and technology has not been merely a series of responses to the requirements of engineers. Scientific studies have led to the discovery of many new glass-forming systems, to a clearer understanding of the mechanisms of nucleation and crystal growth in glass-forming melts, and to some insight into the difficult problem of glass structure. Also, new methods of making glasses and of treating glass articles in a variety of ways to greatly modify their properties have been developed. As a result, material properties like mechanical robustness, chemical resistance, heat resistance, electrical isolation, biocompatibility, large optical transition range and optical transparency have been improved, and this has led to the large scale usage of glass for micro mechanical, micro fluidic and micro optical devices.

The classical piezoresistive pressure sensor chip is, in general bonded on a glass substrate to reduce the stress induced during the packaging process [28, 29]. The very first accelerometer [30] had the mechanical movable parts in sealed cavities and used the bulk micromachined glass to control the damping and to prevent breakdown. For RF-MEMS, glass is an excellent substrate due to its electrical isolation properties. Most bio-chips are fabricated on glass due to its optical transparency and biocompatibility: a micro flow cell for single molecule handling of DNA [31], micro-injectors for DNA mass spectrometry [32], micro-PCR devices for DNA amplification [33], bioanalytical devices such as capillary electrophoresis [34], or dielectrophoresis [35].

1.4 DIFFRACTION LIMIT OF LIGHT

The revolutionary progress in semiconductor, communication, and information industries based on electronic and photonic technologies demands for the development and enhancement of new laser processes to support micro- and nano-technologies. The trend for “smaller size and higher speed” is evident in integrated microchips for computers, micro-optics, and micro-electro-mechanical systems. The ability to optimize the lens design with computers and machine the optics to better specifications have somewhat helped in focusing the laser beam to smaller spot sizes. However, even while acceptably overcoming spherical and chromatic aberrations in lens systems, the diffraction limit still restricts higher resolutions.

The diffraction limit, no matter how good the optical system is will still limit the ability to resolve small objects. This limit arises from the wave nature of light. Light waves interfere and this causes diffraction of light. The diffraction limit of light can be understood by considering two treatments of the problem. This was first treated by Abbe who considered diffraction from a grating. For light of wavelength λ diffracted off of a grating with spacing d and observed through an aperture subtending an angle of 2θ, the minimum spacing for which maxima will be observed is given by the formula,

$$d_{\min} = \frac{\lambda}{\sin\theta} \tag{1.3}$$

Thus, when viewed through an aperture or a lens with a finite collection angle, the resolvable feature separation is limited by the wavelength of light and the solid angle of light collected.

A better estimate of the resolution limit can be obtained by considering the diffraction of light from closely spaced point sources. The light from the point sources, when viewed at a plane in the far field, will produce Airy disk diffraction patterns, consisting of a bright central disk surrounded by concentric rings of lesser intensity. The Rayleigh's criterion for resolving power is that two such spots are resolvable if the distance between the centers of the two Airy disks is equal to the radius of the disks. For two sources in a material of index n, this criterion gives a minimum spacing of

$$d_{\min} = \frac{0.61\lambda}{NA} \tag{1.4}$$

where NA is the numerical aperture of the lens system. The numerical aperture describes the light collection ability of the lens system and can be defined as $n\sin\theta$, where n is the refractive index of the media in which the lens is located and 2θ is the angle collected by the objective. From both these treatments it is obvious that the resolution can only be improved by either increasing the numerical aperture (collection angle), or refractive index of the medium, or reducing the wavelength of light.

Several attempts have been made to get to shorter wavelengths with some success. However, it is becoming more difficult and complicated to use the short optical wavelengths to reach the desired feature sizes. For example, the use of wavelengths in the deep-ultraviolet [36], the extreme-ultraviolet [37], or the x-ray regime [38] requires significantly difficult adjustments to the process, including development of new light sources, and optics. The most serious limitation arises from the fact that the material properties at EUV wavelengths are very different from their properties at UV, visible, and IR wavelengths, such as the strong absorption in almost all materials preventing the use of refractive elements [39, 40]. Although the introduction of light sources with shorter-wavelength and wave-front engineering techniques should help to maintain the current rate of device miniaturization for several more years, it seems that a point will be reached at which the traditional approaches of shortening the exposure wavelength will no longer be able to produce the required feature sizes.

The other approach to improve the diffraction limited resolution of focused light is by increasing the index of refraction at the focus. With an oil immersion lens [41], the space between the lens and sample can be filled with oil, and this shrinks the focused spot size. This technique is limited by the refractive index of the oil, which typically results in a NA~1.4. If a solid is used in place of a liquid, the high refractive index of solids can be harnessed to improve the spatial resolution without significant loss of optical throughput. In analogy to oil immersion, this technique is called solid immersion lens and the best NA = 2.0 was achieved by using GaP SIL [42]. Here the diffraction-limited size of the focused spot is reduced in proportion to the refractive index of the lens placed in close proximity to the substrate. The deciding factor for high optical resolution is the large angle components in the optical system. However there are practical limits to increasing the numerical aperture, as NA is inversely proportional to the depth of focus according to Rayleigh scaling. Also high NA lenses are not amenable to mass-fabrication or microfabrication, rendering beam delivery optics too large and expensive for many applications in education and research [43].

To overcome the diffraction limit and to spatially-control matter on a nanometer scale, several fabrication techniques based on near-field optics have been recently employed. In one such technique, nanostructuring is realized by delivering a laser beam through a hollow near-field tip or illuminating the tip of a scanning probe microscope with a pulsed laser [44, 45]. A strong local optical field is established between the sample surface and the sharp tip when the surface-to-tip gap is a few nanometers. Structures with lateral dimensions below 30 nm, and therefore well below the minimal resolvable feature size of half a wavelength of the light, were produced underneath the tip. However, this kind of near-field nanolithography technique has rarely been used in an industrial setting due to its limited throughput, hollow tip blockage and difficulty in process control.

Instead of tips, nanospheres can be used for creating nanostructures by utilizing the near-field radiation created around a nanosphere by the laser radiation. When the laser beam is incident on the top surface of spheres, there is a field enhancement around the sphere. This optical field enhancement by nanospheres can be explained by Rayleigh and Mie scattering theories [46]. Such optical enhancement can lead to local melting or even vaporization of the substrate materials for nanoscale surface patterning. By using nanospheres, I have circumvented the diffraction limit of light and created nanofeatures on both silicon and glass. In case of gold spheres, features as small as 40 nm ($\lambda/15$) have been realized on silicon.

1.5 THESIS ORGANIZATION

This dissertation is aimed at exploring the use of lasers for micro and nano scale processing of advanced materials like silicon and glass. The objective of the dissertation is two fold: a) use lasers for locally micro bonding glass and silicon wafers, and b) use lasers for nanopatterning glass and silicon. In the first part, glass and silicon wafers are bonded locally in microscale by laser transmission joining technique, and in the second part nanoscale processing is accomplished by circumventing the diffraction limit of light by the use of nanospheres.

In chapter 2, a discussion of bonding glass and silicon wafers locally using a 1064 nm pulsed Nd:YAG laser is presented. The transient melting and re-solidification of the joining substrates are studied experimentally by probing with a 633 nm He-Ne laser. The bonded areas are then studied using a scanning electron microscope (SEM) and a chemical analysis is done to understand the bonding mechanism. Numerical simulation is also carried out using the finite element method to predict the local temperature change of both the glass wafer and the silicon wafer during laser heating. In order to validate the bonding mechanism, the experimental results are compared with the numerical results.

In chapter 3, an array of nanofeatures is created on silicon by using a pulsed Nd:YAG laser. When microspheres are irradiated with a laser beam, there is an optical field enhancement around the spheres as explained by Mie theory. This enhanced field is confined to a very small area and decays nonlinearly in the radial direction. Utilizing this optical near field, nanofeatures are realized on silicon. The experiment is performed for various laser wavelengths, laser energies, and sphere sizes, and the resulting features are characterized using a scanning electron microscope. Finally, these experimental results are compared with the numerical results from a multidimensional, heat transfer model built by Heltzel et al. [47] to simulate the heat transfer through silicon. The experimental results correlate well with the predicted results.

In chapter 4, the nano-scale surface modification of borosilicate glass is reported. Silica nanospheres are deposited and are irradiated with an Nd:YAG laser. At very low energy densities, sub-micron ripples are created on the glass surface. The ripples thus obtained do not satisfy Rayleigh's diffraction condition in that a) the ripple spacing is different from the value predicted by the classical model, b) the spacing is independent of the incident angle, and c) the orientation is not always perpendicular to the laser polarization. Also, the ripple characteristics are not dependent on the diameter of the spheres used and the ripples have almost the same periodicity irrespective of the experimental parameters. However, at higher energy densities hexagonally arranged nanofeatures 350 nm in diameter are formed on the substrate instead of the ripples.

In Chapter 5, nano-scale surface modification of silicon using surface plasmons is presented. The localized optical excitation is achieved by shining a 532 nm pulsed Nd:YAG laser beam on 40 nm gold spheres. Due to the excitation of coherent resonant electron plasma oscillations, there is a strong local enhancement of the electromagnetic field around the spheres. As a result of this enhancement, surface modification occurs by the melting and subsequent resolidification of silicon. Since this excitation is confined to a very small area, nanofeatures ranging from 30-40 nm in diameter are realized. These nanofeatures which are smaller than the laser wavelength ($\lambda/15$) are realized because the gold spheres interact strongly with visible light when resonantly excited at their surface plasmon frequency. The study is conducted on Silicon, polyimide and PMMA substrates. Nanofeatures were observed on silicon and polyimide, as the absorption of PMMA at this wavelength is very minimal.

Chapter 6 is a summary of the thesis and the main results are reiterated. In this chapter the significance of the experimental results is discussed and an outlook for future work and applications of lasers in nanomanufacturing is provided.

1.6 REFERENCES

1. Maiman, T.H., "Stimulated optical radiation in ruby", *Nature*, **187,** 493, (1960).
2. Svelto, O., *Principles of lasers*, Plenum Press, New York, 1989.
3. Duley, W.W., *Laser processing and analysis of materials*, Plenum Press, New York, 1983.
4. Born, W., and Wolf, E., *Principles of optics*, 6th edition, Pergamon, Oxford, 1980.
5. Zhang, X., Grigoropoulos, C. P., Kranjnovich, D. J., and Tam, A. C., "Excimer laser projection micromachining of polyimide thin films annealed at different temperatures", *IEEE Transactions on Components, Packaging and Manufacturing Technology: Part C (Manufacturing)*, **119,** 201-213, (1996).
6. Wood, R.F., White, C.W., and Young, R.T., *Semiconductors and semimetals*, Academic Press, Orlando, 1984.
7. Zergioti, I., Mailis, S., Fotakis, C., Chen, S.C., and Grigoropoulos, C.P., "Microdeposition of metals by femtosecond excimer laser", *Applied Surface Science*, **127-129,** 601-605, (1998).
8. Park, H.K., Xu, X., Grigoropoulos, C. P., Do, N., Klees, L., Leung, P. T., and Tam, A. C., "Transient optical transmission measurement in excimer laser irradiation of amorphous silicon films", *Transactions of ASME Journal of Heat Transfer*, **115,** 178-183, (1993).
9. Williams, E.W., *The cd-rom and optical disc recording systems*, Oxford University Press, Oxford, 1994.
10. Tam, A.C., Leung, W.P., Zapka, W., and Ziemlich, W., "Laser cleaning techniques for removal of surface particulates", *Journal of Applied Physics*, **71,** 3515-3523, (1992).
11. Nakata, Y., Kumuduni, W.K.A., Okada,T., and Maeda, M., "Plume-substrate interaction in pulsed-laser deposition of high-temperature superconducting thiin films", *Applied Physics Letters*, **64,** 2599-2601, (1994).
12. Fogarassy, E., Pattyn, H., Elliq, M., Slaoui, A., Prevot, B., Stuck, R., Unamuno, S., and Mathe, E. L., "Pulsed laser cystallization and doping for the fabrication of high quality poly-si tfts", *Applied Surface Science*, **69,** 231-241, (1993).
13. Endert, H., Galvanauskas, A.,Sucha, G., Patel, R., and Stock, M., "Novel ultrashort pulse fiber lasers for micromachining applications", *RIKEN Review*, **43,** 23-27, (2002).
14. Matz, R., Weber, H., and Weimann, G., "Laser-induced dry etching of integrated inp microlenses", *Applied Physics A: Materials Science & Processing*, **65,** 349-353, (1997).

15. Lu, Y.F., Takai, M., Komuro, S., Shiokawa, T., and Aoyagi, Y., "Surface cleaning of metals by pulsed-laser irradiation in air", *Applied Physics A: Materials Science & Processing*, **59,** 281-288, (1994).

16. Sato, S., Inaba, H., "Optical trapping and manipulation of microscopic particles and biological cells by laser beams", *Optical and Quantum Electronics* **28,** 1-16, (1996).

17. Malek, C.K., Saile, V., "Applications of liga technology to precision manufacturing of high-aspect-ratio micro-components and systems: A review", *Microelectronics Journal*, **35,** 131-143, (2004).

18. Kitai, M.S., Popkopv, V.L., Semchishen, V.A., and Kharizov, A.A., "The physics of uv laser cornea ablation", *IEEE Journal of Quantum Electronics*, **27,** 303-307, (1991).

19. Vogel, A., Schweiger, P., friieser, A., Asiyo, M.N., and Birngber, R., "Intraocular nd:Yag laser surgery: Light-tissue interaction, damage, and reduction of collateral effects", *IEEE Journal of Quantum Electronics*, **26,** 2240-2260, (1990).

20. Boyd, I.W., *Laser processing of thin films and microstructures.*, Springer-Verlag, Berlin, 1987.

21. Fann, W.S., Storz, R., Tom, H.W.K., and Bokor, J., "Direct measurement of non-equilibrium laser-heated gold films", *Physical Review Letters*, **68,** 2834-2837, (1992).

22. Fujimoto, J.G., Liu, J.M., and Ippen, E.P., "Femtosecond laser interaction with metallic tungsten and non-equilibrium electron and lattice temperatures", *Physical Review Letters*, **53,** 1837-1840, (1984).

23. Rogers, T. and Kowal, J., "Selection of glass, anodic bonding conditions and material compatibility for silicon-glass capacitive sensors", *Sensors and Actuators a-Physical*, **46,** 113-120, (1995).

24. Carabe, J., Gandia, J.J., "Thin-film-silicon solar cells", *Opto-Electronics Review*, **12,** 1-6, (2004).

25. Wilson, A.R., Olsson-Jacques, C., Muscat, R.F. *Adhesive bond degradation sensor*. in *Proceedings of the SPIE - The International Society for Optical Engineering*. 2002.

26. Zhang S., Z., W., Zhang, S.C., Yao, S., "The research status of soi high-temperature pressure sensor", *Journal of Hebei University of Technology*, **34,** 14-19, (2005).

27. Smith, C.S., "Piezoresistance effect in germanium and silicon", *Physical Review*, **94,** 42-49, (1954).

28. Kim. C., a.K.Y., "Micro xy-stage using silicon on a glass substrate", *Journal of Micromechanics and Microsystems*, **12,** 103-107, (2002).

29. Madou, M.J., *Fundamentals of microfabrication*, 2nd edition, CRC Press, Boca raton, FL, 2002.

30. Roylance, L., Angell. J. *A miniature integrated circuit accelerometer*. in *Solid State Circuits Conference*. 1978.

31. Rusu, C., "Direct integration of micromachined pipettes in a flow channel for single DNA molecule study by optical tweezers," *Journal of Micromechanical Systems*, **10,** 238-246, (2001).

32. Luginbuhl, P. *Micromachined injector for DNA mass spectrometry*. in *Proceedings of Transducers '99*. 1999.

33. Zheng, W.a.C., S.C. *Continuous flow, submicroliter scale pcr chip for DNA amplification*. in *Proceedings of SPIE - the International Society for Optical Engineering*. 2001.

34. Simpson, P.C., Woolley, A.T., and Mathies, R.A., "Microfabrication technology for the production of capillary array electrophoresis chips", *Biomedical Microdevice*, **1/1,** 7-25, (1998).

35. Iliescu, C., "Fabrication of a dielectrophoretic chip with 3d silicon electrodes", *Journal of Micromechanics and Microsystems*, **15/3,** 494-500, (2005).

36. Rothschild, M., Bloomstein, T.M., Curtin, J.E., Downs, D.K., Fedynyshyn, T.H., Hardy, D.E., Kunz, R.R., Liberman, V., Sedlacek, J.H.C., Uttaro, R.S., Bates, A.K., and Van Peski, C., "157 nm: Deepest deepultraviolet yet", *Journal of vacuum Science and Technology B*, **17,** 3262-3266, (1999).

37. Gwyn, C.W., Stulen, R., Sweeney, D., and Attwood, D., "Extreme ultraviolet lithography", *Journal of Vacuum Science and Technology B*, **16,** 3142-3149, (1998).

38. Silverman, J.P., "Challenges and progress in x-ray lithography", *Journal of Vacuum Science and Technology B*, **16,** 3137-3141, (1998).

39. Gwyn, C. *Euv llc program status and plans*. in *1st EUVL Workshop*. 2001. Tokyo.

40. Hector, S.D. *Euvl masks: Requirements and potential solutions*. in *Emerging Lithographic technologies VI, SPIE Proceedings*. 2002.

41. Gibson, S.F., and Lanni, F., "Experimental test of an analytical model of aberration in an oil-immersion objective lens used in three-dimensional microscopy", *journal of Optical Society of America*, **8,** 1601-1613, (1991).

42. Hirota, K., Milster, T.D., Shimura, K., Zhang, Y., and Jo, J.S., "Near-field phase change optical recording using a gap hemispherical lens", *Japanese Journal of Applied Physics Part I - Regular Papers, Short Notes & review Papers*, **39,** 968-972, (2000).

43. Okazaki, S., "Resolution limits of optical lithography", *Journal of Vacuum Science and Technology*, **B9,** 2829-2833, (2001).

44. Ohtsu, M., and Hori, H., *Near-field nano-optics*, Kluwer Academic, New York, 1999.

45. Betzig, E. and Trautman, J.K., "Near-field optics - microscopy, spectroscopy, and surface modification beyond the diffraction limit", *Science*, **257,** 189-195, (1992).

46. Munzer, H.J., Mosbacher, M., Bertsch, M., Zimmermann, J., Leiderer, P., and Boneberg, J., "Local held enhancement effects for nanostructuring of surfaces", *Journal of Microscopy-Oxford*, **202,** 129-135, (2001).

47. Heltzel, A.J., Theppakuttai, S., Howell, J.R., and Chen,S.C., "Analytical and experimental investigation of laser-nanosphere interaction for nanoscale surface modification", *Journal of Heat Transfer*, **127,** 1231-1235, (2005).

Chapter 2: Laser Bonding of Glass and Silicon

2.1 ABSTRACT

In this chapter, silicon and glass wafers are bonded directly using a localized laser heating technique. A 1064 nm pulsed Nd:YAG laser of 12 ns pulse width is used for the bonding process. As glass is transparent to this wavelength, the laser beam passes through the glass wafer and is absorbed by silicon. As a result, silicon is melted and upon resolidification, bonding is realized between the two wafers. The transient melting and resolidification of silicon is studied by probing with a 633 nm continuous wave He-Ne laser. This transmission joining process is performed locally while the entire wafer is maintained at a low temperature. The bonded areas are studied in detail using a scanning electron microscope (SEM) and a chemical analysis is done to understand the bonding mechanism. Numerical simulation is also carried out using finite element method to predict the local temperature change of both the glass wafer and the silicon wafer during laser heating. In order to validate the bonding mechanism, the experimental results are compared with the numerical results.

2.2 NOMENCLATURE

c = specific heat (J/kg.K)
h = specific enthalpy (J/m^3)
I = intensity (W/m^2)
J_0 = pulse energy (J)
k = thermal conductivity (W/mK)
Q_{ab} = heat generation (J/m^3)
R = reflectivity
r = cylindrical coordinate

T = temperature (K)

t = time (s)

z = coordinate along propagation (m)

α = absorption coefficient (m^{-1})

ρ = density (kg/m^3)

Subscript

g = glass

p = pulse

Si = silicon

2.3 INTRODUCTION

Wafer bonding, also termed direct bonding or fusion bonding, has increasingly become a technology of choice for material integration in various areas of microelectronics, optoelectronics, and microelectromechanical systems (MEMS). Wafer bonding refers to the phenomenon wherein mirror-polished, flat, and clean wafers of almost any material, when brought into contact at room temperature, are locally attracted to each other by Van der Waals forces and adhere or bond to each other [1]. In most, but by far not all cases, the wafers involved in actual applications are typical single crystal semiconductors such as silicon or gallium arsenide. However, the wide availability of chemical mechanical polishing in integrated circuit fabrication and a variety of precision thinning approaches has led to a widespread and diverse use of wafer bonding. The application areas range from microelectronic devices, power devices, high voltage devices, non-linear optics devices, and MEMS including pressure and acceleration sensors, optical switches, BioMEMS and micro fluidics [1-4].

The first report on the sticking of flat glass plates can be found in a 1638 book by Galileo [5]. Though he did not study direct-bonding, he made this discovery while studying the attractive forces between sliding bodies. In the 17th century, bonding was observed by Sir Isaac Newton during his experiments with sunlight. He noticed that as soon as a flat and a convex optically transparent element of the same refractive index were stuck together, i.e. brought in '*optical contact*' a reflection free '*back spot*' was seen at the tangent position, that is, there was no interference at the touching interface. Newton was astonished by the fact that at the '*black spot*' no optical reflection occurred at all, and therefore, named it a '*black spot*' seen in '*optical contact*' [6]. Later on, it was observed around 1900 in the then newly developing optical industry that glass pieces polished to optical quality tend to stick to each other. The adherence of optically flat pieces of glass and fused quartz was considered mostly a nuisance rather than an advantage. In these cases, the pieces adhering to each other were usually bulk pieces (like prisms) and nowhere as thin as typical wafers now used for wafer bonding.

The first systematic investigation of room-temperature adherence of silica was reported by Lord Rayleigh [7]. The interaction of surfaces was later investigated and interaction energies of two curved surfaces were measured and attributed to Van der Waals forces either between the contacting solids themselves or between monolayers of molecules with high dipole moments such as water layers [8]. The first bonding of silicon to appropriate sodium-containing glasses of a similar thermal expansion coefficient, which requires the application of high voltages at temperatures around 500°C, was introduced in 1969 by Wallis & Pommerantz [9]. The excellent mechanical strength of silicon combined with the electrical insulation, chemical durability, and optical transparency of glass makes the silicon-glass couple the most employed material combination in MEMS. Another reason for this combination is the very small difference in coefficient of thermal expansion between glass and silicon [10]. The various types of bonding techniques used throughout history are explained below.

The first instance of any form of bonding can be found as early as 2nd or 1st millennium B.C. Cold welding or plasticity bonding is the adhesive joining of a malleable metal into recesses of a hard metal, under ambient conditions by shock pressure (hammering), where by the reconstructed surface layers of the hard and malleable metal are plastically transferred to a metallic bond. The Mycenaean civilization excelled in the cold welding of gold and silver, for example, both separately or in combination, as shown in Figure 2.1, or hammered into shape in bronze utensils or weapons [11].

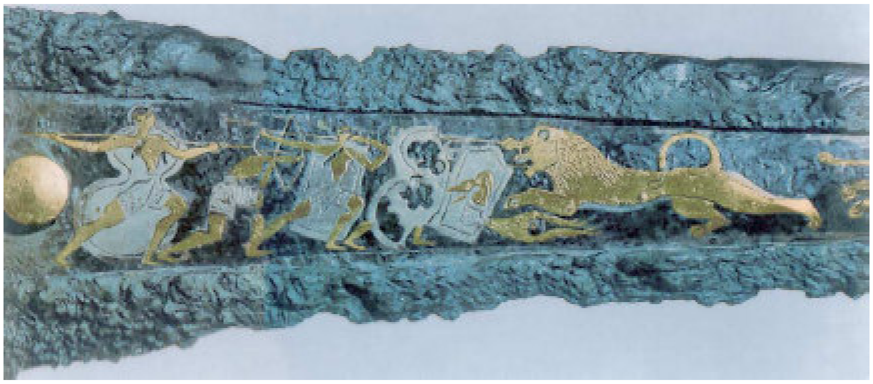

Figure 2.1: Bronze dagger blade with cold-welded gold and silver decorations. From Mycena, Greece.

Enameling or melt bonding results in a *fused bond*, and it is the adhesive joining of a metal (noble otherwise) and a glass by melting a glass frit paste which fuses to a chemical (covalent) bond. Though this technology dates back to ancient times, it is still extensively applied in decorative arts. Figure 2.2a, a Chinese Moonvase is a magnificent example of this type of bonding and belongs to the 17th century [12].

Figure 2.2: (a) Fusion bonding - 17th century Chinese Moonvase., (b) Melt bonding - gold-glass medallion from Alexandria (Egypt), 375 A.D.

Fusion bonding is a technology based on coalescence and diffusion. It is characterized by the cohesive/adhesive joining of two solid bodies, clamped together or even direct-bonded, and annealed in a specific atmosphere at a specific temperature, up to an atomic mobility level at which the reconstructed surface layers of the two elements are chemically (covalently) united. The first application of fusion bonding can be found in the so-called gold-glass technology applied between 300 and 600 A.D. [13]. Figure 2.2b, from 375 A.D., Egypt shows a gold-glass medallion in which the gold and silver foils were fusion bonded to a black, non-transparent glass, and then stippled/dotted and covered with a thin layer of a transparent glass. More recently, fusion bonding has become an important step in upgrading direct bonding by Van der Waals forces to covalent chemical forces. This annealing step is almost always a prerequisite in direct-bonded silicon technology, and in such cases it is often called '*bond-strengthening*'.

TABLE 2.1: A SURVEY OF THE MOST FREQUENTLY ENCOUNTERED CONTACT BONDING TYPES

Name	Period of Invention	Characteristic features
Cold welding	1st and 2nd millennium B.C; Middle East, Europe	Adhesive plasticity metallic bonding; ambient conditions; reconstructed surface layer plastically resolved
Fused bond (general); Fusion bonding	1st and 2nd millennium B.C; Greece, Middle East, Celtic Europe	Adhesive melt-bonding; melt temperature of one of the components (glass paste); reconstructed surface layer resolved, fused
Direct bonding	17th & 18th century 19th and 20th century	Seen as a non-reflective optical contact; ambient conditions Cohesive and adhesive (Van der Waals) bonding; ambient conditions
Direct bonding + bond strengthening	20th century	Cohesive and adhesive (Van der Waals) bonding; elevated temperature applied; transfer to covalent bonding; reconstructed surface layer resolved
Silicon fusion bonding	1960s to present day	Cohesive and adhesive (Van der Waals) bonding; ambient conditions + annealing; transfer to covalent bonding; reconstructed surface layer resolved
UHV bonding	1960 (quartz); 1995 (silicon) to present-day	Cohesive and adhesive covalent bonding; ambient temperature in UHV; covalent bond; pure reconstructive surface layer bonding; free dangling bonds; lateral solid-phase epitaxial growth

A compendious survey of the most frequently encountered contact bonding types is presented in Table 1. Of all the above mentioned bonding types, anodic bonding [14-17] and silicon fusion bonding [18, 19] are the most common techniques used for bonding silicon-glass and silicon-silicon wafers respectively. The main utility of the anodic bonding process stems from the relatively low process temperature. Since glass and silicon remain rigid during anodic bonding, it is possible to attach glass to silicon surfaces, preserving the etched features in either the glass or silicon. Bonding can be accomplished on a hot plate in atmosphere or vacuum at temperatures between 180 and 500 ^{o}C. However, the high electric field used in the process (about 1000 V), and the migration of Sodium make anodic bonding of glass to silicon a rather difficult technology. In addition, the viscous behavior of glass results in degraded long-term stability of components.

Silicon fusion bonding has the ability to bond two silicon wafers without an intermediate layer or applying an electric field. As a result many devices are fabricated using this method. However, since fusion bonding is done in a furnace at temperatures as high as 1100 ^{o}C, it therefore tends to damage the pre-fabricated microelectronics or pre-seeded biomolecules and thus exclude the use of thermally sensitive materials for micro- and meso-devices. Also, the high residual stress and stringent requirements for the surface quality of wafers impose serious limitation on the flexibility of this technique. Furthermore in cases where hermetic sealing is desired, the residual gases trapped in the hermetic cavity can induce plastic deformation in thin silicon membranes as the gases expand due to the high temperature associated with the bonding process [20]. Moreover, both anodic and fusion bonding are conducted along the entire wafer and so they do not provide an effective solution to integrating discrete micro or nano-structures onto a chip to realize lab-on-a-chip or other integrated micro-systems.

As high temperatures and high electric fields are undesirable, another type of bonding to avoid these difficulties was developed. Intermediate thin film bonding [21, 22], employs thin films as bonding media, instead of bonding the wafers directly. The thin films can either be low temperature sealing materials, such as organic materials or solder alloy, or high temperature sealing materials, such as metal films or gas frit. However, the use of an intermediate layer is undesirable in many applications, as it increases the size of the device and complicates the fabrication of many devices and this severely limits the scope of this approach.

As a result, researchers have been trying to find reliable bonding processes that can be conducted under a low temperature [23-25], and without using an intermediate layer. Unfortunately, these new processes are highly dependent on the bonding materials, surface treatment, and surface flatness [26, 27]. Due to the diverse applications mentioned earlier, the bonding process has to fulfill several key requirements: low bonding temperature, little or no electric fields, no intermediate layer, low cost, and high reliability to provide large yield and long term stability.

To overcome the above mentioned difficulties, a new bonding technique has been introduced recently. This technique is based on the concept of localized heating [28, 29], and it satisfies all the above requirements. In early works, resistive micro-heaters were used to provide the localized heating. The main disadvantage with this process is the lack of flexibility. Since this technique is based on Joule heating, the response time is slow.

Lasers with their selectivity, precision and low heat distortion are an attractive choice for providing localized heating. The first application is in the joining of thermoplastics, and the technique is known as laser transmission welding [30, 31]. In laser transmission welding of thermoplastics, the laser beam penetrates the upper, transparent joining part and is completely absorbed by the lower, dark surface. The radiation is converted into localized heat and melting takes place. The heat required to melt the transparent joining part is received from the thermal conduction of the absorbing part. Strong welding of both parts occurs under external compression and the internal joining pressure, arising from local warming and expansion. Nearly all thermoplastics and elastomers can be welded using this technique. This technique can be extended to the bonding of glass and silicon, and in this case it is called laser transmission joining.

Laser transmission joining is a non-contact, fast and single-step process with “direct-write” capability. This approach makes it possible to bond micro-structures and pre-immobilized biomolecules for sensing, actuation, and even computing in BioMEMS. Other advantages include tight control on time and temperature window for processing, and the opportunity to select various suitable wavelengths depending on the wafer materials to be bonded. Infrared to ultraviolet and pulsed to continuous wave lasers can be employed for localized laser bonding [32-36].

In one of the previous laser bonding works, a pulsed 355 nm excimer laser was used for glass-to-silicon bonding in the presence of indium as an intermediate layer. In order to achieve selective bonding, a masking material was also used [37]. Both pulsed and continuous wave 1064 nm lasers have been employed for the bonding process in the presence of aluminum or gold as an intermediate bonding layer [38, 39]. In all these works, a low temperature intermediate bonding layer is used and melting and resolidification of this layer results in the desired bond. As explained earlier, the presence of an intermediate layer is undesirable and it is the objective of this work to achieve joining with lasers without an intermediate layer. Also a lot of work has been done in characterizing the bond quality and strength, but very little work has been done to investigate the physical mechanism of the laser bonding process for micro- and meso-systems, and this is the second objective of my work.

In this work, a 1064 nm pulsed nanosecond laser is employed for the bonding process in the absence of an intermediate layer. The laser beam is focused to a small spot and direct joining of glass and silicon is achieved by using a single laser pulse. The bonding area is probed for obtaining more information about the melting process. A low powered continuous wave He-Ne laser is used for the in-situ monitoring to obtain information about the melting time, based on the change in reflectivity of silicon. This is accomplished by using a photo detector attached to an oscilloscope. Numerical simulation is also carried out using finite element method to predict the local temperature change of both glass and silicon wafers during laser heating. The melting duration information obtained experimentally is then compared with the simulation results.

2.4. EXPERIMENTAL SETUP

The samples used for bonding are silicon (Nova Electronic Materials, Texas) and Pyrex glass (Bullen Ultrasonics, Ohio) wafers of thickness 500 μm. The surface roughness of the silicon and glass samples to be joined is in the nanometer scale (< 2 nm), as the wafers are well polished. Before loading the samples, care is taken to ensure that the samples are clean and free of any contaminants. For this reason, they are first cleaned in ethanol solution followed by rinsing in deionized water. The samples are then dried with nitrogen gas. The clean samples are then loaded in between two aluminum plates with an opening in the center, and pressure is applied continuously till the end of bonding process, by bolting the plates together. The tight contact of both the joining partners caused by the pressing device ensures elimination of small air gaps as well as good heat conduction to the glass. When locally heated by the laser radiation, glass is softened due to heat conduction from the silicon surface and after cooling, the adhesion of the joint compounds results in a tight joining.

The schematic of the experimental setup is shown in Figure 2.3. A 1064 nm pulsed Nd:YAG laser of 12 ns pulse width is used for the bonding process. The output of the laser beam passes through an aperture and a beam splitter which is used to split the incident laser beam into two - one part to be used for bonding and the other for measuring the energy of pulses used for bonding. The sample is mounted on a 3-D stage and the laser beam is focused to a spot size of 800 μm diameter by using a plano-convex lens (diameter = 2.54 cm and focal length = 5.08 cm). By adjusting the working distance between the lens and the sample, the bonding area can be varied.

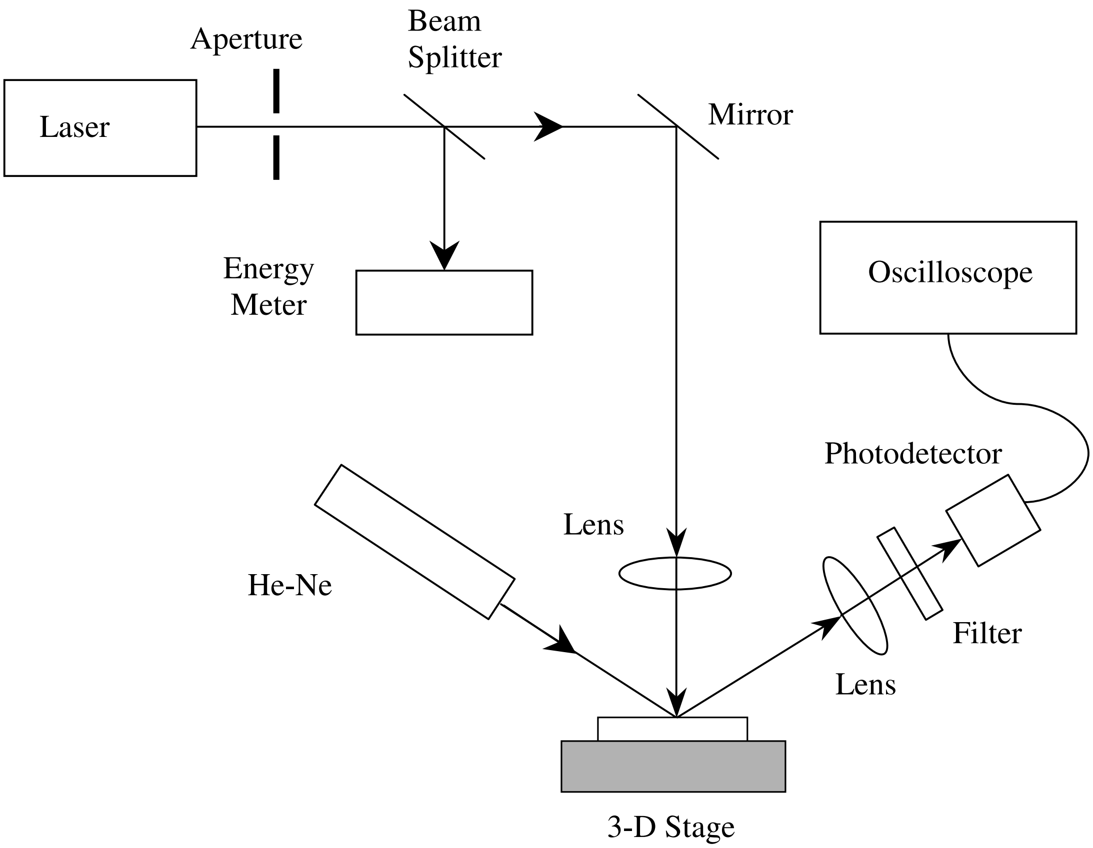

Figure 2.3: Schematic of the experimental setup

The bonding process depends on the melting area as well as the melting duration of silicon and the subsequent heat conduction to glass. Therefore to ensure proper bonding between the substrates, an *in-situ* monitoring of the melting process is very important. A low powered 633 nm continuous wave He-Ne laser (20 mW) is used as a probing beam for on-line monitoring [40, 41]. In order to make sure the measurement of melting time is accurate, the detection beam is focused on to the heating area. This is achieved by expanding the He-Ne beam using a beam expander and focusing it using a plano-convex lens with a shorter focal length.

The incident probing beam reflected by the silicon sample is collected by a fast silicon PIN photodiode with 1 ns rise/fall time. The photodiode is connected to a digitizing oscilloscope with 500 MHz bandwidth and 1 GSa/s sampling rate operated at single-shot acquisition mode (1 ns time resolution). To eliminate the emission signal and other reflected wavelengths from the heated silicon surface, optical filters were used which only transmit the probing laser wavelength. The heating laser pulse is used as a trigger to capture the reflected detecting beam. Upon heating, the reflectivity of silicon changes and this results in a change in the intensity of signal captured by the oscilloscope, which provides melting duration information during bonding.

2.5 NUMERICAL SIMULATION

The laser heating process is a highly nonlinear phenomenon due to the Gaussian distribution of laser energy in time and space. In addition, material properties like thermal conductivity and optical properties such as absorption coefficient are strong nonlinear functions of temperature. As a result, an analytical solution of the heat transfer and melting problem is less practical and numerical results were sought instead.

The heat conduction process during and after laser irradiation has been studied before [42-44]. Previous researchers have shown that the Fourier heat conduction equation is still valid for nanosecond laser processing in micrometer regimes [45]. In line with this, the Fourier heat conduction equation is used in this work to find the temperature distribution. In earlier works, one-dimensional heat conduction models were employed [42-44] and surface heat flux boundary conditions were used [45]. However, to study the localized heating effect in this work, the temperature profile along the direction perpendicular to the incident direction has to be considered and thus a two-dimensional, transient heat conduction model is established. A volumetric heat generation source with an exponentially decaying distribution in the propagation direction and with Gaussian distribution in the lateral direction is used to more accurately study the local temperature distribution. The absorption coefficient of silicon at 1064 nm is small and this justifies the assumption of volumetric heat generation.

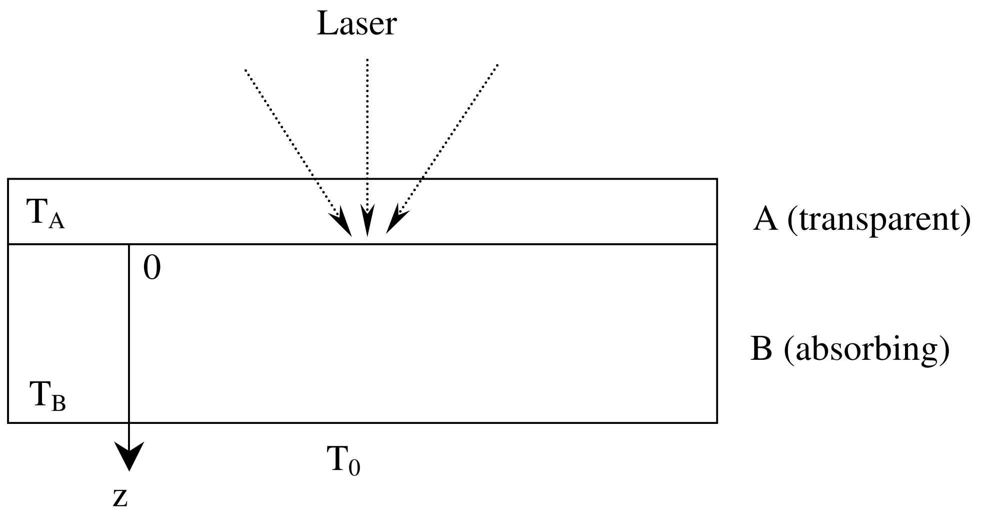

Figure 2.4: Schematic of the heat transfer through glass (A) and silicon (B).

The schematic of the heat transfer through glass-silicon is shown in Figure 2.4. Pyrex glass is virtually transparent to the laser beam at the wavelength considered. Thus the incident laser beam is primarily absorbed by silicon. Heat is conducted to glass from the molten silicon, thereby softening the glass at the silicon-glass interface. Upon solidification, bonding is realized between the two layers.

The governing heat conduction equation in the glass layer is described as:

$$\rho c \frac{\partial T}{\partial t} = k\left[\frac{\partial^2 T}{\partial z^2} + \frac{\partial^2 T}{\partial r^2} + \frac{1}{r}\frac{\partial T}{\partial r}\right] \tag{1}$$

The governing equation in silicon during laser irradiation is:

$$\rho c\frac{\partial T}{\partial t}=\frac{\partial}{\partial z}(k\frac{\partial T}{\partial z})+\frac{\partial}{r\partial r}(kr\frac{\partial T}{\partial r})+Q_{ab}(z,r,t) \tag{2}$$

The energy absorption Q_{ab} in silicon is related to the incident laser intensity I_i, which is defined as:

$$I_i(r,t)=I_0\exp(-\frac{r^2}{r_p^2})\exp(-\frac{t^2}{t_p^2}) \qquad (-\infty<t<+\infty) \tag{3}$$

where I_0 is the maximum intensity of the laser pulse in the center at time t = 0. After reflection, the laser energy distribution in the silicon substrate is characterized as:

$$I=(1-R)I_i\exp(-\alpha z) \tag{4}$$

The laser energy is attenuated in the medium and results in heat generation:

$$Q_{ab}=-\frac{\partial I}{\partial z}=(1-R)\alpha I_i\exp(-\alpha z) \tag{5}$$

The laser pulse energy is related to I_0, t_p and r_p by:

$$J_0=\int_{-\infty}^{\infty}\int_0^{\infty}I_i(r,t)2\pi r dr dt=I_0 t_p r_p^2\pi^{3/2} \tag{6}$$

The contact thermal resistance between silicon and glass is ignored since silicon and glass are in close contact by the application of force. Thus the boundary condition at the interface is:

$$(k\frac{\partial T}{\partial z})_g = (k\frac{\partial T}{\partial z})_{Si} \tag{7}$$

At the outer surface of the bi-layer system the heat loss is assumed to be negligible since the heat loss is many orders of magnitude smaller compared to the heat generation [42]:

$$\frac{\partial T}{\partial z} = 0 \tag{8}$$

Because of the symmetry due to laser heating with a Gaussian-type intensity distribution, an adiabatic boundary condition is used at r = 0:

$$\frac{\partial T}{\partial r} = 0 \tag{9}$$

Initially the temperature is uniformly distributed as

$$T(z, r, 0) = 300K \tag{10}$$

Although the exact temperature of the bonding area during laser heating is unknown, it is reasonable to believe that it reaches or even exceeds the melting point of silicon. Thus modeling phase change processes is necessary to predict the temperature in the bonding area. The phase change modeling of silicon is achieved via an enthalpy method. Before phase change the temperature change is related to enthalpy change by: $dh = \rho c dT$ while at phase change, additional enthalpy change includes the latent heat of fusion, which is 1.8×10^6 J/kg for silicon.

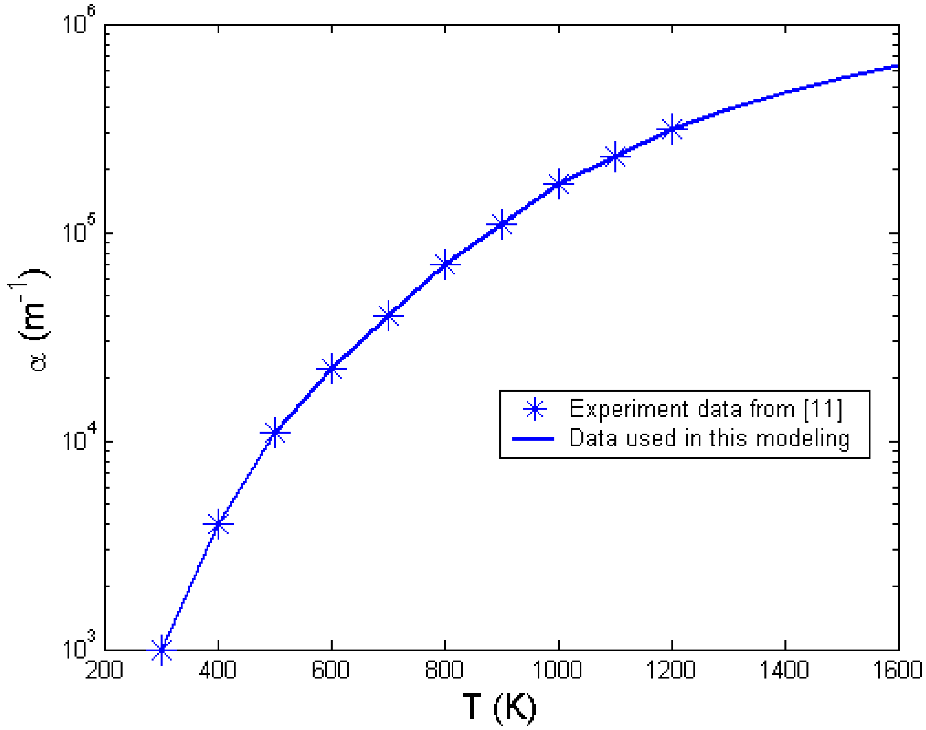

Figure 2.5: The absorption coefficient of silicon at 1064 nm at different temperatures

At room temperature, the penetration depth at 1064 nm is in the order of a few hundred micrometers, which ensures a volumetric heat generation over the whole thickness of the silicon substrate. However as shown in Figure 2.5, at temperatures over 1000 K the absorption coefficient goes up to around 2×10^5 m^{-1} [46] and the penetration depth reduces to a few micrometers. The increasing temperature results in stronger absorption in a much thinner layer, which in return greatly increases the local temperature. This effect is considered in our modeling and approximated by iteration. The absorption data at even higher temperatures are extracted from the available literature data extrapolated linearly for use in our modeling. Previous work has shown that the thermal conductivity of silicon as a function of temperature is approximately exponential until the melting point at 1687 K. The thermal conductivity data of silicon as a function of temperature used in simulation in this paper is shown in Figure 2.6. The thermal conductivity of silicon increases after melting due to the increased mobility of molecules and is assumed temperature-independent.

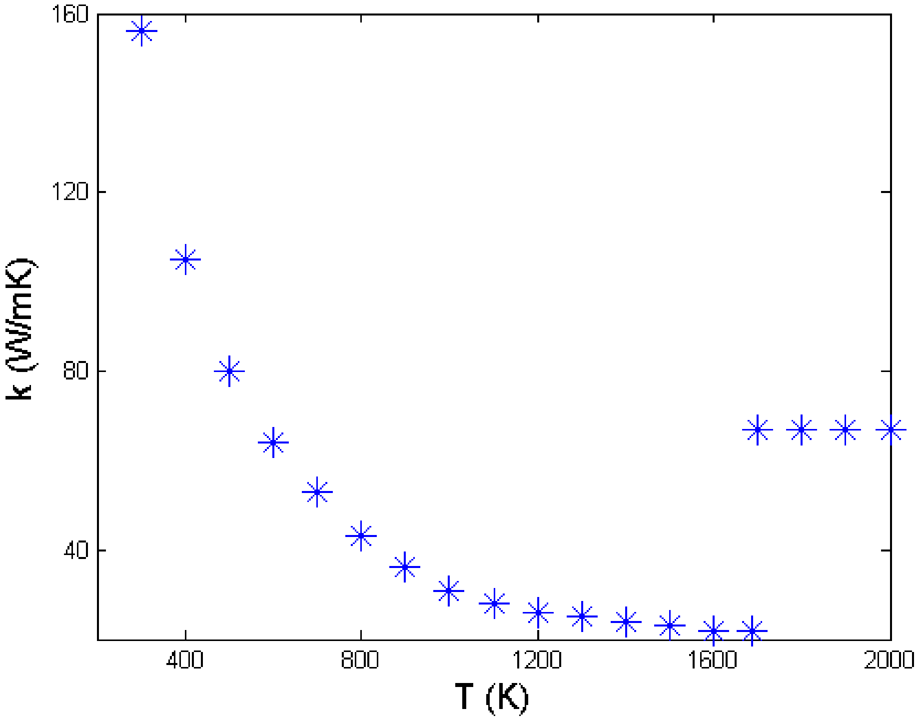

Figure 2.6: Thermal conductivity of silicon at different temperatures (data in [44])

2.6 RESULTS AND DISCUSSION

The glass and silicon samples to be bonded are loaded onto the sample holding device and pressure is applied to ensure a firm contact between the samples. A single laser pulse focused to a spot size of 800 µm is used for bonding and the corresponding pulse energy is measured using an energy meter (Nova Display, Ophir Optronics, Inc). The continuous wave He-Ne laser used for probing is aligned with the heating spot using an alignment paper and focused to a spot of diameter 250 µm. The silicon sample is melted due to absorption of the heating laser irradiation and this result in a change in the intensity of He-Ne laser beam reflected by the silicon sample. This is due to the change in reflectivity of silicon upon heating, as reflectivity depends both on the phase as well as temperature. A signal captured by the photo detector and oscilloscope during the bonding process is shown in Figure 2.7.

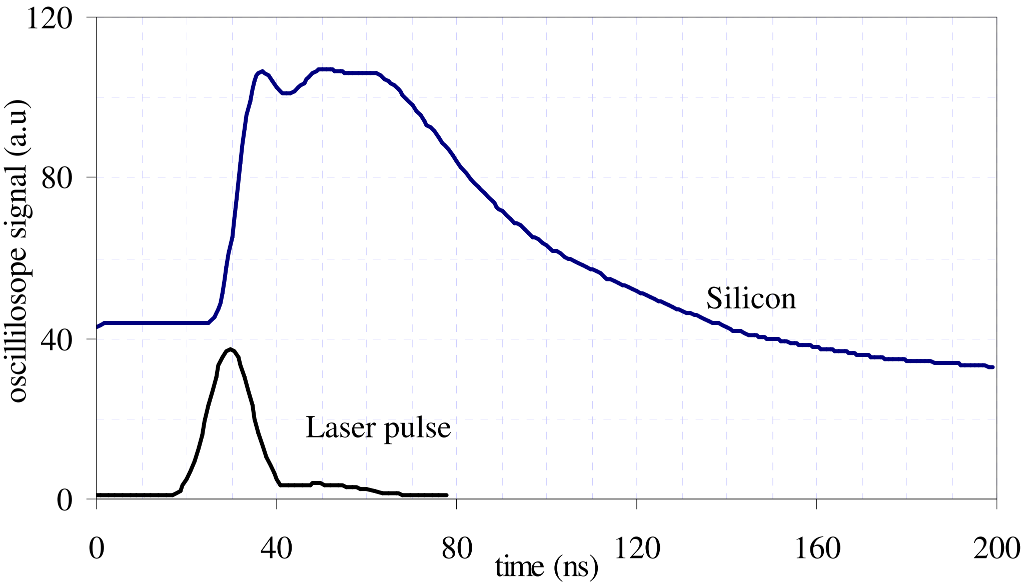

Figure 2.7: Change in reflectivity of silicon during laser heating measured in-situ

The black colored line represents the Nd:YAG laser pulse (pulse width 12 ns) used for melting, and the blue colored line is the He-Ne beam reflected from the silicon surface. From the figure it is clear that the reflectivity of silicon starts to increase almost at the end of the heating laser pulse and continues increasing until reaching a constant value. This increase in reflectivity is due to the phase change from solid to liquid as it dominates the change due to increase in temperature. In the liquid phase, silicon acts like a metal and the reflectivity is over 90%, which is almost thrice that of solid silicon.

After about 40 ns, the liquid silicon starts to solidify and the reflectivity decreases gradually depending on the cooling rate. At this juncture, heat conduction to glass results in the softening of glass, and the subsequent joining of both substrates. Comparing the reflectivity values before and after melting, it can be see that the reflectivity values after bonding are slightly lower. This could be due to the change in surface morphology at the interface of both silicon and glass due to melting and resolidification.

The melting duration and the temperature of silicon are calculated numerically for heating by a single laser pulse (65 mJ energy and 800 μm spot size). Figure 2.8 shows the temperature history at different locations of the heating area. From the simulation, the melting time calculated for an area of diameter 280 μm ($0.35R_0$) is found to be 35 ns.This compares well with the experimental value of 40 ns for a detecting area of diameter 250 μm.

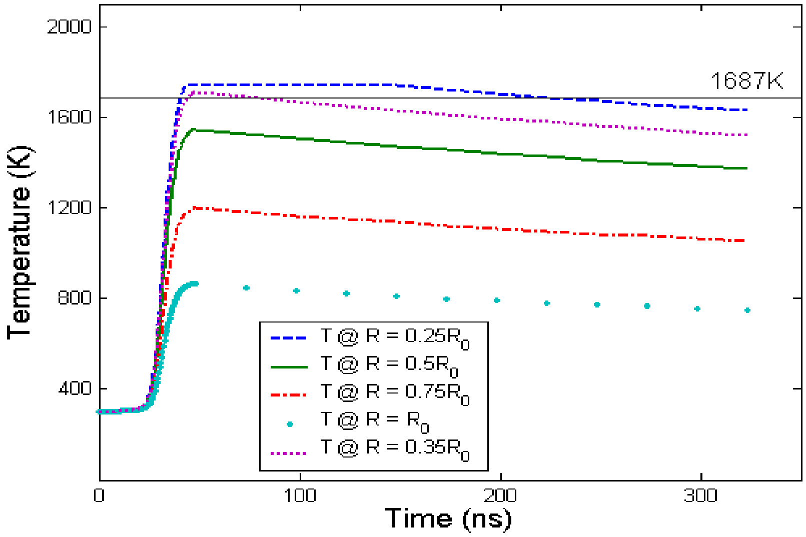

Figure 2.8: Silicon surface temperature history at different locations after a single laser pulse (wavelength = 1064 nm, pulse width = 12 ns, energy = 65 mJ, beam diameter = 800 µm)

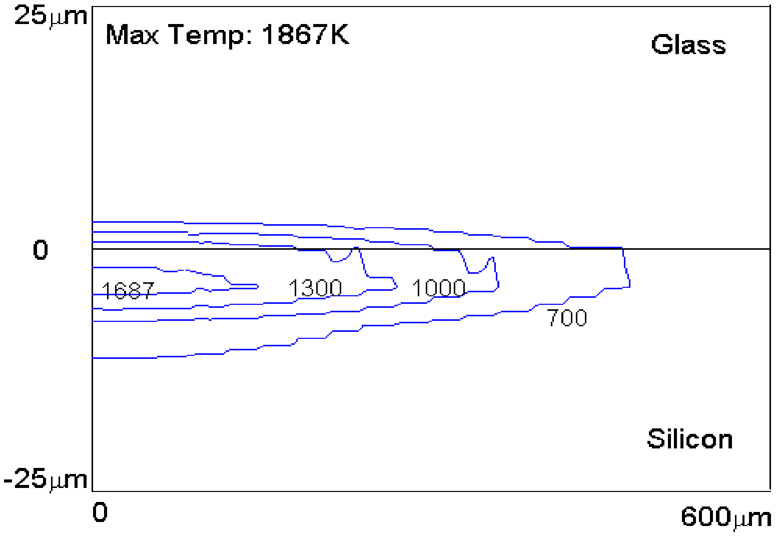

Figure 2.9: Temperature contour right after a single laser pulse (same as before)

The temperature distribution calculated for the entire heating area immediately after a single pulse is given in Figure 2.9. The center of the heating area of silicon attains a maximum temperature of 1867 K whereas at the periphery it is only about 700 K. This is due to the Gaussian energy distribution of the heating laser beam. From the figure it is clear that about 40% of the heating area reaches a temperature above the melting point of silicon which is about 1687 K.

Figure 2.10 shows the temperature distribution 300 ns after heating by a single pulse. At this time only the center of silicon remains molten, whereas on the glass side almost a third of the heating area is at a temperature higher than the glass transition temperature, which is around 1100 K [47, 48]. This means that glass remains molten for a longer duration than silicon due to the difference in thermal conductivity.

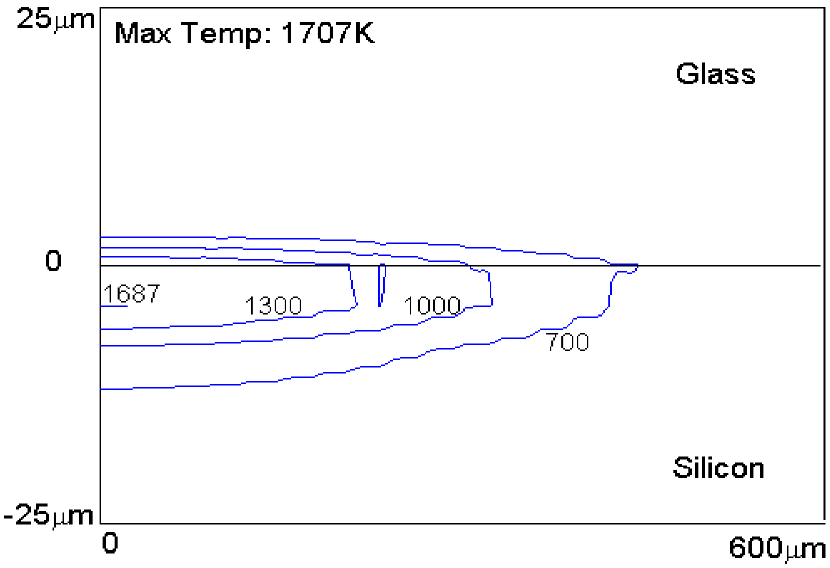

Figure 2.10: Temperature contour 300 ns after a single laser pulse (same as before)

Figure 2.11a shows the schematic of a glass wafer on top of silicon wafer. The laser heating was performed right on the edge of the glass sample to study the cross section of the bonded area. Here, half of the laser beam is within the glass wafer while another half is outside the glass wafer. The microscopic image, Figure 2.11b shows the melting of silicon in the laser processed area, outside the glass sample.

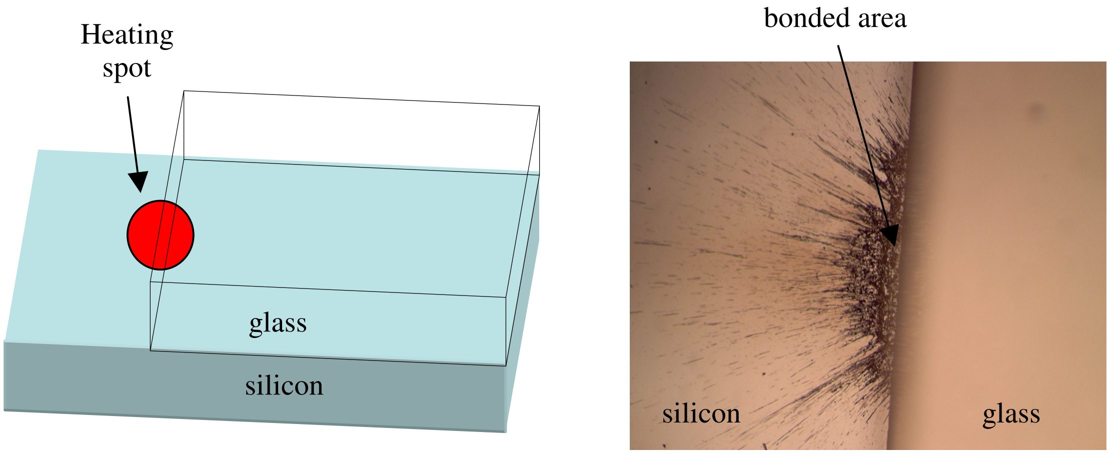

Figure 2.11: a) Schematic showing the bonded area at the edge of the glass sample. b) Corresponding optical microscopic image of the bonded area

To show the gap between the bonded substrates, the experiment is repeated and Figure 2.12a is a microscopic image of the bonded interface and this image clearly shows the joining of both silicon and glass at the bonding area. Figure 2.12b is an SEM micrograph showing the glass-silicon interface. Due to the pressure applied on both samples, the molten silicon is splashed at the interface and this can be seen on the sides of the glass sample. Also, the side walls of both the substrates are not flat because of scribing with a diamond tip in order to cut the samples into smaller pieces. As a result, it appears as if there is a gap between the both the bonded substrates.

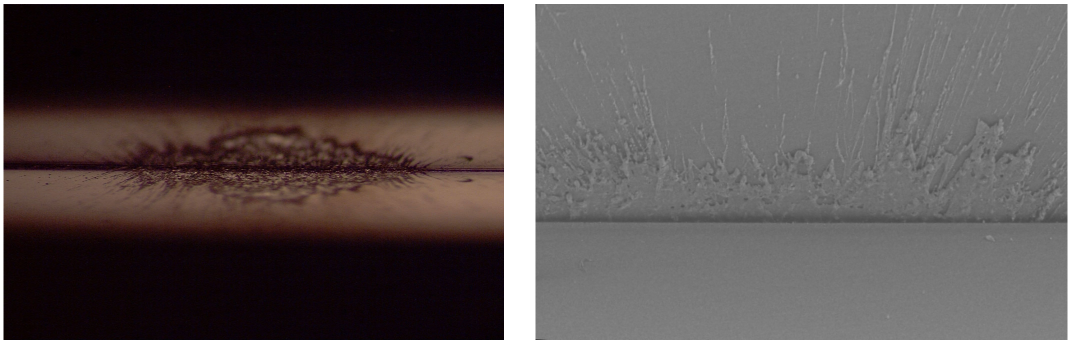

Figure 2.12: a) Optical microscopic image of the bonded area at the glass-silicon interface. b) SEM micrograph of the glass-silicon interface.

In order to study the bonding process in detail, the experiment is repeated for various laser pulse energies, and the bonded glass-silicon sample is separated and observed under an SEM. The heating laser beam is focused to a spot size of 400 μm diameter and the rest of the experimental parameters are kept constant. From the results shown in Figure 2.13, it can be seen that for the highest energy used in the experiment, the entire laser exposed area is melted, and the resulting bonding area is also maximum. As the energy is reduced, the melted zone and the corresponding bonding area also gradually decrease. The bonding area continues to decrease with energy to a point where little or no bonding is realized.

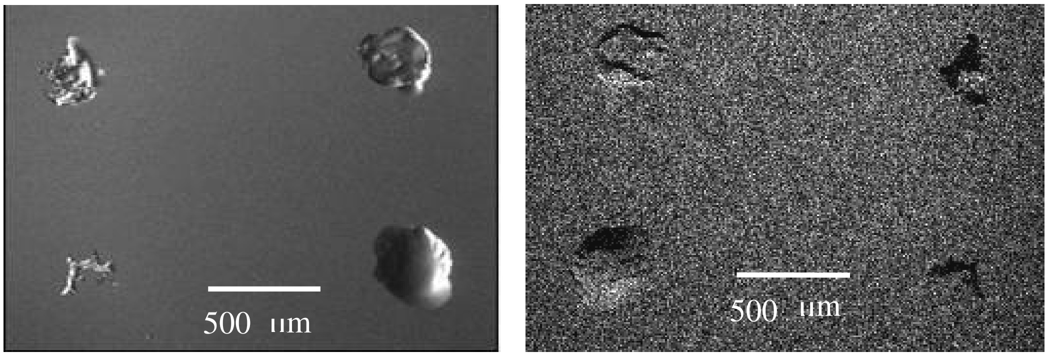

Figure 2.13: SEM micrograph of the bonded area after separation: a) glass b) silicon

An energy dispersive spectroscopy (EDS) chemical analysis was performed on the silicon sample to see if there is any diffusion from glass and the result is presented in Figure 2.14. The analysis shows the presence of Al and Na only in the bonded area of the silicon sample thereby confirming the diffusion of Al and Na components from glass into silicon during solidification. This is because of the longer melting duration of glass which is still in the molten state when silicon starts to solidify. This shows that melting of both silicon and glass is essential for the bonding of glass and silicon.

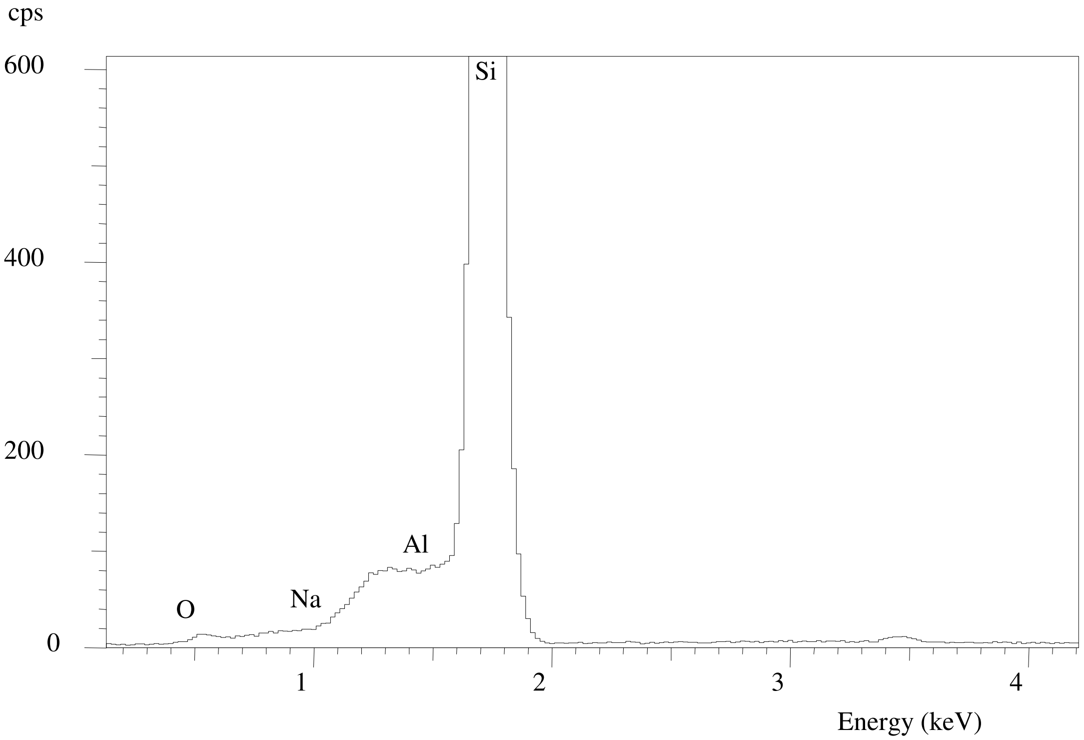

Figure 2.14: Chemical analysis of the bonded area at the silicon interface.

2.7 CONCLUSIONS

Glass and silicon wafers were joined together by using a pulsed Nd:YAG laser in the absence of an intermediate layer. This localized laser transmission joining technique provides a high temperature in a selected and localized region to achieve bonding while maintaining the whole wafer still at room temperature. A continuous wave He-Ne laser was used to provide on-line monitoring of the transient melting process of silicon upon pulsed laser heating. The on-line monitoring system is non-intrusive and gives reliable information about the melting and subsequent resolidification process. Estimates of the bonding time based on a finite element model compares well with the experimental results. Temperature profiles obtained during and after bonding suggest temperatures greater than the melting temperature and glass transition temperature of silicon and glass respectively, at the bonding interface. The chemical analysis shows the presence of Al and Na in bonded areas of silicon. The diffusion of these components from glass is due to the longer melting duration of glass compared to silicon.

2.8 REFERENCES

1. Gosele, U., and Tong, Q. Y., "Semiconductor wafer bonding", *Annual Review of Materials Science,* **28**, 215-241, (1998).
2. Gosele, U. et al., "Fundamental issues in wafer bonding", *Journal of Vacuum Science & Technology A,* **17**, 1145-1152, (1999).
3. Gosele, U., Tong, Q. Y., Schumacher, A., Krauter, G., Reiche, M., Plossl, A., Kopperschmidt, P., Lee, T. H., and Kim, W. J., "Wafer bonding for microsystems technologies", *Sensors and Actuators a-Physical,* **74**, 161-168, (1999).
4. Haisma, J., Spierings, B. A. C. M., Biermann, U. K. P., and Vangorkum, A. A., "Diversity and Feasibility of Direct Bonding - a Survey of a Dedicated Optical-Technology", *Applied Optics,* **33**, 1154-1169, (1994).
5. Galileo Galilei, *Discorsi E DimostrazioniMatematiche* (1638).
6. Haisma, J., and Spierings, G. A. C. M., "Contact bonding, including direct-bonding in a historical and recent context of materials science and technology, physics and chemistry - Historical review in a broader scope and comparative outlook", *Materials Science & Engineering R-Reports,* **37**, 1-60, (2002).
7. Rayleigh., L., *Proceedings of Physical Society A,* **156**, 326-349, (1936).
8. Israelachvili, J., *Intermolecular and Surface Forces* (Academic, London, 1991).
9. Pomerantz, G. W. a. D. I., "Field Assisted Glass-Metal Sealing", *Journal of Applied Physics,* **40**, 3946-3949, (1969).

10. Rogers, T., and Kowal, J., "Selection of Glass, Anodic Bonding Conditions and Material Compatibility for Silicon-Glass Capacitive Sensors", *Sensors and Actuators a-Physical,* **46**, 113-120, (1995).

11. Savage, G., *A Concise History of Bronzes* (Thomes & Hudson, London, 1968).

12. Wolf, D., "Should All Surfaces Be Reconstructed", *Physical Review Letters,* **70**, 627-630, (1993).

13. Hanfmann, G. M. A. (New York Graphic Society, Greenwitch, CT, USA).

14. Chen, M. X., Yi, X. J., Gan, Z. Y., and Liu, S., "Reliability of anodically bonded silicon-glass packages", *Sensors and Actuators a-Physical,* **120**, 291-295, (2005).

15. Aljancic, U., Resnik, D., Vrtacnik, D., Mozek, M., and Amon, S., "Silicon-glass anodic bonding", *Informacije Midem-Journal of Microelectronics Electronic Components and Materials,* **34**, 168-173, (2004).

16. Xing, Q. F., Yoshida, M., and Sasaki, G., "TEM study of the interface of anodic-bonded Si/glass", *Scripta Materialia,* **47**, 577-582, (2002).

17. Gerlach, A., Maas, D., Seidel, D., Bartuch, H., Schundau, S., and Kaschlik, K., "Low-temperature anodic bonding of silicon to silicon wafers by means of intermediate glass layers", *Microsystem Technologies-Micro-and Nanosystems-Information Storage and Processing Systems,* **5**, 144-149, (1999).

18. Yousefpour, A., Hojjati, M., and Immarigeon, J. P., "Fusion bonding/welding of thermoplastic composites", *Journal of Thermoplastic Composite Materials,* **17**, 303-341, (2004).

19. Xiao, Z. X., Wu, G. Y., Li, Z. H., Zhang, C. B., Hao, Y. L., and Wang, Y. Y., "Silicon-glass wafer bonding with silicon hydrophilic fusion bonding technology", *Sensors and Actuators a-Physical,* **72**, 46-48, (1999).

20. Henmi, H., Shoji, S., Shoji, Y., Yoshimi, K., and Esashi, M., "Vacuum Packaging for Microsensors by Glass Silicon Anodic Bonding", *Sensors and Actuators a-Physical,* **43**, 243-248, (1994).

21. Kutchoukov, V. G., Laugere, F., van der Vlist, W., Pakula, L., Garini, Y., and Bossche, A., "Fabrication of nanofluidic devices using glass-to-glass anodic bonding", *Sensors and Actuators a-Physical,* **114**, 521-527, (2004).

22. Goustouridis, D., Minoglou, K., Kolliopoulou, S., Chatzandroulis, S., Morfouli, P., Normand, P., and Tsoukalas, D., "Low temperature wafer bonding for thin silicon film transfer", *Sensors and Actuators a-Physical,* **110**, 401-406, (2004).

23. Chiao, M., and Lin, L. W., "Hermetic wafer bonding based on rapid thermal processing", *Sensors and Actuators a-Physical,* **91**, 398-402, (2001).

24. Chiao, M., and Lin, L. W., "Accelerated hermeticity testing of a glass-silicon package formed by rapid thermal processing aluminum-to-silicon nitride bonding", *Sensors and Actuators a-Physical,* **97-8**, 405-409, (2002).

25. Wei, J., Nai, S. M. L., Wong, C. K. S., Sun, Z., and Lee, L. C., "Low temperature glass-to-glass wafer bonding", *Ieee Transactions on Advanced Packaging,* **26**, 289-294, (2003).

26. Bower, R. W., and Chin, F. Y. J., "Low temperature direct silicon wafer bonding using argon activation", *Japanese Journal of Applied Physics Part 2-Letters,* **36**, L527-L528, (1997).

27. Bower, R. W., Ismail, M. S., and Roberds, B. E., "Low-Temperature Si3n4 Direct Bonding", *Applied Physics Letters,* **62**, 3485-3487, (1993).

28. Lin, L. W., "MEMS post-packaging by localized heating and bonding", *Ieee Transactions on Advanced Packaging,* **23**, 608-616, (2000).

29. Cheng, Y. T., Lin, L. W., and Najafi, K., "Localized silicon fusion and eutectic bonding for MEMS fabrication and packaging", *Journal of Microelectromechanical Systems,* **9**, 3-8, (2000).

30. Kagan, V. A., Bray, R. G., and Kuhn, W. P., "Laser transmission welding of semi-crystalline thermoplastics - Part I: Optical characterization of nylon based plastics", *Journal of Reinforced Plastics and Composites,* **21**, 1101-1122, (2002).

31. Kagan, V. A., and Pinho, G. P., "Laser transmission welding of semicrystalline thermoplastics - Part II: Analysis of mechanical performance of welded nylon", *Journal of Reinforced Plastics and Composites,* **23**, 95-107, (2004).

32. Lin, L. W., "Thermal challenges in MEMS applications: phase change phenomena and thermal bonding processes", *Microelectronics Journal,* **34**, 179-185, (2003).

33. Jee, Y., and Woodard, O. C., "Laser Application in Packaging of Very Large-Scale Integrated Chips", *Journal of Vacuum Science & Technology B,* **8**, 1789-1793, (1990).

34. Hayward, J. D., "Optimization and Reliability Evaluation of a Laser Inner Lead Bonding Process", *Ieee Transactions on Components Packaging and Manufacturing Technology Part B-Advanced Packaging,* **17**, 547-553, (1994).

35. Tao, Y., Malshe, A. P., and Brown, W. D., "Investigation of laser-assisted bonding for MEMS packaging", *International Journal of Nonlinear Sciences and Numerical Simulation,* **3**, 427-431, (2002).

36. Kim, J., and Xu, X. F., "Excimer laser fabrication of polymer microfluidic devices", *Journal of Laser Applications,* **15**, 255-260, (2003).

37. Luo, C., and Lin, L. W., "The application of nanosecond-pulsed laser welding technology in MEMS packaging with a shadow mask", *Sensors and Actuators a-Physical,* **97-8**, 398-404, (2002).

38. Mescheder, U. M., Alavi, M., Hiltmann, K., Lietzau, C., Nachtigall, C., and Sandmaier, H., "Local laser bonding for low temperature budget", *Sensors and Actuators a-Physical,* **97-8**, 422-427, (2002).

39. Wild, M. J., Gillner, A., and Poprawe, R., "Locally selective bonding of silicon and glass with laser", *Sensors and Actuators a-Physical,* **93**, 63-69, (2001).

40. Hatano, M., Moon, S., Lee, M., Suzuki, K., and Grigoropoulos, C. P., "Excimer laser-induced temperature field in melting and resolidification of silicon thin films", *Journal of Applied Physics,* **87**, 36-43, (2000).

41. Xu, X., Grigoropoulos, C. P., and Russo, R. E., "Nanosecond-time-resolution thermal emission measurement during pulsed excimer-laser interaction with materials", *Applied Physics a-Materials Science & Processing,* **62**, 51-59, (1996).

42. Chen, G., and Tien, C. L., "Thermally-Induced Optical Nonlinearity During Transient Heating of Thin-Films", *Journal of Heat Transfer-Transactions of the Asme,* **116**, 311-316, (1994).

43. Abraham, E., and Halley, J. M., "Some Calculations of Temperature Profiles in Thin-Films with Laser-Heating", *Applied Physics a-Materials Science & Processing,* **42**, 279-285, (1987).

44. Bloisi, F., Vicari, L., Cavaliere, P., Martellucci, S., Quartieri, J., Mormile, P., and Pierattini, G., "Laser-Induced Thermal Profiles in Thermally and Optically Thin-Films", *Applied Physics B-Photophysics and Laser Chemistry,* **47**, 67-69, (1988).

45. Burgener, M. L., and Reedy, R. E., "Temperature Distributions Produced in a 2-Layer Structure by a Scanning Cw Laser or Electron-Beam", *Journal of Applied Physics,* **53**, 4357-4363, (1982).

46. Jellison, G. E., and Lowndes, D. H., "Optical-Absorption Coefficient of Silicon at 1.152-Mu at Elevated-Temperatures", *Applied Physics Letters,* **41**, 594-596, (1982).

47. Schmidt, H., Scholze, H., and Kaiser, A., "Contribution to the Kinetics of Glass-Formation from Solutions", *Journal of Non-Crystalline Solids,* **48**, 65-77, (1982).

48. Bansal, C., and Srinivasan, V., "Microscopic Theory for the Glass State", *Physics Letters A,* **75**, 420-422, (1980).

Chapter 3: Nanoscale Processing of Silicon with Optical Near Field

3.1 ABSTRACT

In this chapter, an experimental investigation on the sub micron features created on silicon by the irradiation of microspheres on the substrate surface, with a pulsed laser is presented. Silica microspheres of 1.76 μm diameter are deposited on the silicon substrate and are irradiated with a pulsed Nd: YAG laser of wavelength 532 nm. The experiment is performed for various laser wavelengths, laser energies, and sphere sizes, and the resulting features are characterized using a scanning electron microscope. Finally, these experimental results are compared with the numerical results from a multidimensional, heat transfer model built by Heltzel et al. [1] to simulate the heat transfer through silicon. The experimental results correlate well with the predicted results.

3.2 INTRODUCTION

The discovery of the unique properties of silicon and the development of silicon electronics has been one of the most important technical events of the second half of the twentieth century. The review paper by Petersen in 1982 [2] led to widespread acceptance of micromachined silicon as a structural material. The basic mechanical properties of single-crystal silicon were collectively assembled in the paper, which also provided a number of examples of structures to illustrate the potential for MEMS.

The early MEMS applications established single-crystal silicon as a robust mechanical material; its Young's modulus is directionally dependent and near that of stainless steel, and it has a Knoop hardness twice that of iron and very high tensile strength. Compared to single-crystal silicon which is brittle and fractures without yielding, polycrystalline silicon has shown a tighter spread in fracture-stress distribution than single-crystal silicon. As a result, industrially prepared polycrystalline silicon proves to be more controllable than single-crystal material, and it has already demonstrated low coefficients of variation in a manufacturing environment [3-5]. Some of the important physical properties of silicon [6] are shown in Table 3.1.

TABLE 3.1: PHYSICAL PROPERTIES OF SILICON [6].

Crystal structure	Cubic, diamond lattice
Density	2.3 g cm^{-3}
Atomic density	5 x 10^{22} cm^{-3}
Yield strength (breaking)	1000 MPa
Elastic modulus	160 GPa
Piezoresistive coefficient	-120...+120
Thermal conductivity	150 W mK^{-1}
Thermal expansion	2.5 x 10^{-6} K^{-1}
Thermoelectric coefficient c-Si	800-1100 μV K^{-1}

The industrial demand for smaller structures required for the manufacture of quantum devices, high-density recording media, etc., have resulted in the need for fabrication technology at the nanometer scale. Thus a variety of structuring techniques have been investigated in the past for micro/nano fabrication of silicon. The technologies used for structuring should be sufficient to fulfill the needs posed by the great variety of functions of most devices, the specificity of surroundings in which they will operate, and the optimum cost/performance ratio for the targeted application.

One of the structuring techniques that employ ions for surface modification is the focused ion beam (FIB) patterning [7-9]. Here, a finely focused beam of gallium ions is used for milling [10], direct material sputtering [11-13], and initiation of chemical reactions for etching [14] or deposition [15]. Another variation in the ion beam patterning technique is the ion projection lithography (IPL), in which ions extracted from a source and collimated through a mask with the imaging pattern are accelerated through a series of electrostatic lenses that project the ions onto a wafer substrate, where the ions penetrate and modify the substrate materials [16, 17]. However the main disadvantage with this technique is its inability for large area fabrication and high manufacturing costs.

Another technique that employs electrons instead of the ions is the e-beam lithography [18]. One-dimensional silicon nanowire structures were made by using the proximity and accumulation effects of electron-beam [19]. To minimize the proximity effect, porous silicon was patterned at moderate electron beam energies, and this allows the possibility of direct lateral structuring, a key factor in the realization of high quality devices for photonics [20]. Again, this technique suffers from the fact that it is a slow serial process with high manufacturing costs. Another disadvantage is that, these are high-energy processes which can cause radiation damage, leading to the possibility of interface states or deep levels in quantum devices. Thus, a low-energy patterning process is an important technological challenge for the fabrication of nanostructure devices.

Recently, atomic force microscopy (AFM) with low tip voltages (~10 V) under a controlled humidity environment has been used to locally structure silicon [21-24]. The oxide feature size is typically on a scale of tens of nanometers [25]. Nanoelectronic devices using AFM oxidation have been fabricated on silicon [26], metal [27], and gallium arsenide [28]. However, the controlled humidity and oxidation of the substrate may be undesirable depending on the type of device and functionality. So another technique based on scanning probe microscopy (SPM) was introduced [29, 30]. Nanostructuring is accomplished by the local tip induced compression of porous silicon layers [31]. In another work, nanopatterning of organic monolayers on silicon was achieved by the selective chemisorption of norbornadiene. This concept served as the basis for creating spatially resolved templates to initiate chemical reactions with other chemical species in the presence of hydrogen-passivated silicon [32]. Even though this technique is capable of producing nanometer sized features, the physical contact of the tip with substrate results in unwanted stress and surface damage. As a result, non invasive structuring techniques were explored and lasers prove to be an excellent choice.

The continuing development of pulsed laser materials processing positions it as a key enabling technology in providing high-resolution, high accuracy, high-speed and flexible production. As a result lasers are increasingly used not only for cutting, drilling, welding, surface hardening, annealing, recrystallization, and glazing; but also for micro/nano patterning and extended area processing by laser induced etching, material deposition, chemical transformation etc [33-38]. However, the diffraction limit of light is one major hurdle in employing lasers for nano manufacturing. Due to this diffraction limit, the smallest feature that can be obtained employing lasers is comparable to half the laser wavelength used for structuring.

To overcome the diffraction limit and to spatially-control matter on a nanometer scale, several fabrication techniques based on near-field optics have been recently employed. The physics of evanescent electromagnetic waves, which is the central concept used in near-field optics dates back to Newton when he first recognized the phenomenon of total internal reflection. But the importance of such waves was ignored for a long time in optical and surface physics until the existence of an exponentially decaying field near the exit of an aperture was proved [39]. The branch of near-field optics has come a long way since then, due to its enormous potential for applications in super-fine optical microscopy, high-resolution photofabrication, single-molecule detection and local spectral analysis.

In one such technique based on near-field optics, nanostructuring is realized by delivering a laser beam through a hollow near-field tip or illuminating the tip of a scanning probe microscope with a pulsed laser [40, 41]. A strong local optical field is established between the sample surface and the sharp tip when the surface-to-tip gap is a few nanometers. Structures with lateral dimensions below 30 nm, and therefore well below the minimal resolvable feature size of half a wavelength of the light, were produced underneath the tip. However, this kind of near-field nanolithography technique has rarely been used in an industrial setting due to its limited throughput, hollow tip blockage and difficulty in process control.

Instead of tips, nanospheres can be used for creating nanostructures by utilizing the near-field radiation created around a nanosphere by the laser radiation. The accidental discovery of particle induced damage during dry laser cleaning of irregularly shaped Al_2O_3 particles on glass [42] have led to this exciting yet simple technique. When spherical colloidal particles like silica (SiO_2) and polystyrene were used as contaminants on silicon wafers, features with diameters of 200-400 nm and depths of 10-80 nm depending on the irradiation conditions, were found at the former position of the particles. Nanosphere based fabrication [43, 44] induced by the optical near-field was first employed for patterning a urethane-urea copolymer containing a push-pull type azobenzene. In this kind of polymers, the surface deformation is attributed to the gradient force of the optical near-field [45]. Thus, if nanospheres are arranged in a periodic monolayer on the substrate, massively parallel nanostructuring could be realized [46].

When the laser beam is incident on the top surface of spheres, there is a field enhancement around the sphere. This optical field enhancement by nanospheres can be explained by Rayleigh and Mie scattering theories [47]. Rayleigh scattering takes place when the diameter of the sphere is less than the wavelength of the light. In this case, the sphere is treated as a dipole radiator and the electric field enhancement is at its sides along the direction of polarization of the incident light and there is hardly any focusing. In contrast, when the diameter of the sphere is equal to or greater than the laser wavelength, light is scattered elastically and the field is enhanced several times at the exit side of the spheres. Mie theory calculations show that this enhancement is due to both near-field and scattering effects [48]. Such optical enhancement can lead to local melting or even vaporization of the substrate materials for nanoscale surface patterning. It has been reported that the intensity distribution changes dramatically with the size of the sphere and also the distance between the sphere and the substrate [49].

In this chapter, I report a massively parallel nanopatterning method for creating nanofeatures on silicon by depositing a monolayer of silica nanospheres. Silica nanospheres of 1.76 μm diameter are deposited on the silicon substrate and irradiated with a pulsed Nd: YAG laser of wavelength 532 nm. The resulting features are characterized using a scanning electron microscope. In order to understand the feature forming mechanism in detail, the wavelength of laser radiation is varied from 532 nm to 355 nm. Also the effect of sphere diameter is studied by using two different spheres - 1.76 μm and 640 nm respectively. The laser fluence is varied for each case and the effect of polarization is also studied experimentally. Finally, these experimental results are compared with the numerical results from a multidimensional, heat transfer model built by Heltzel et al., to simulate the heat transfer through silicon.

3.3 EXPERIMENTAL PROCEDURE

3.3.1 Sample Preparation

The first report in which ordered monolayers of colloidal particles were systematically utilized for the fabrication of submicroscopic surface structures was published in 1981 [50]. In their work, they simply applied a suspension of colloidal particles with a diameter of 312 nm onto a glass plate and allowed it to evaporate. Afterwards, a small portion of the glass plate was covered with a monolayer of hexagonally arranged spheres. The experiments carried out by [51] revealed for the first time the mechanism of the self-assembly process that eventually leads to hexagonally close packed arrays of colloidal particles. Array formation proceeds in two steps: First, a nucleus is formed when the thickness of the solvent layer (generally water) approaches the diameter of the particles. When the tops of the particles protrude from the water surface, it is deformed and, due to surface tension effects, the spheres are pulled together. Theoretical calculations have shown that these lateral capillary forces can exceed the thermal energy k_BT of the particles by many orders of magnitude [52, 53]. In the second step, evaporation of the solvent from within the micromenisci between the spheres causes water influx from outside, which is related to convective particle transport towards the nucleus.

The aforementioned method is simple but results in poorly organized monolayer. Since the quality of the resulting patterns strongly depends on the properties of the substrate as well as on how homogeneous the process of evaporation is, I focused my efforts on obtaining an efficient treatment to clean the substrate and, at the same time, I controlled the temperature and the humidity of the system by means of common tools.

The sample used for patterning is a 500 μm thick *n*-type (100) polished silicon wafer with a surface roughness of less than a few nanometers (< 2 nm). For cleaning purposes, the silicon substrates were ultra-sonicated in water and subsequently in isopropyl alcohol for at least 1 hour. The silicon wafer was preserved in ethanol until used. This type of silicon wafer has a native oxide layer with a stoichiometry close to SiO_2 and a thickness of 2–3 nm, which makes the surface hydrophilic. The hydrogen terminated silicon wafer with no surface oxidized layer was prepared by dissolving SiO_2 layer in diluted HF solution. The silicon wafers were used immediately after they were prepared.

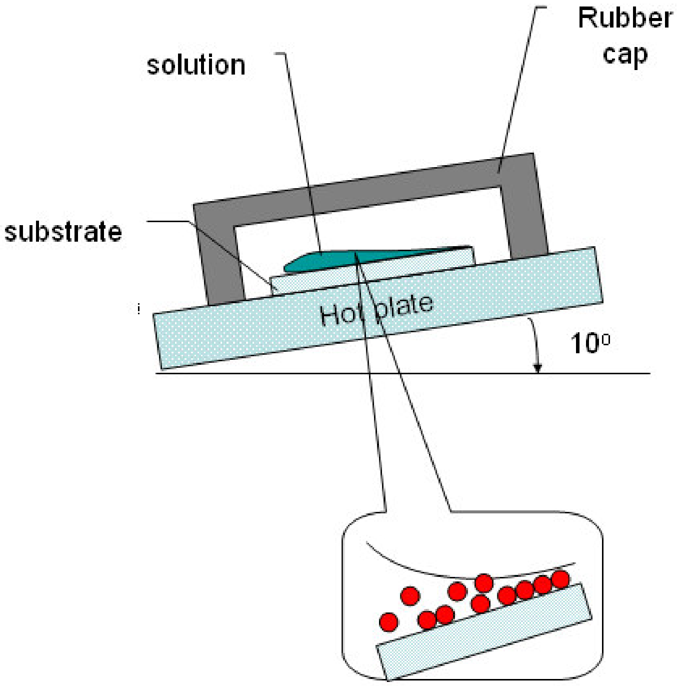

Figure 3.1: The apparatus used for making the monolayer of silica spheres on silicon.

A simple chamber consisting of a hot-plate and a rubber lid was used to control the temperature and humidity. As shown in Figure 3.1, the sample substrate was placed on the hot-plate and covered by the rubber lid. The set-up was tilted about 10°. The rubber lid provided a relatively good thermal stability as well as protected the surface from the external air flow, which could disturb the self arrangement. A few drops of 1 % (w/v) colloids of silica spheres (diameter = 1.76 µm, index of refraction = 1.58, Bangs Lab, PA) were applied onto the silicon substrate.

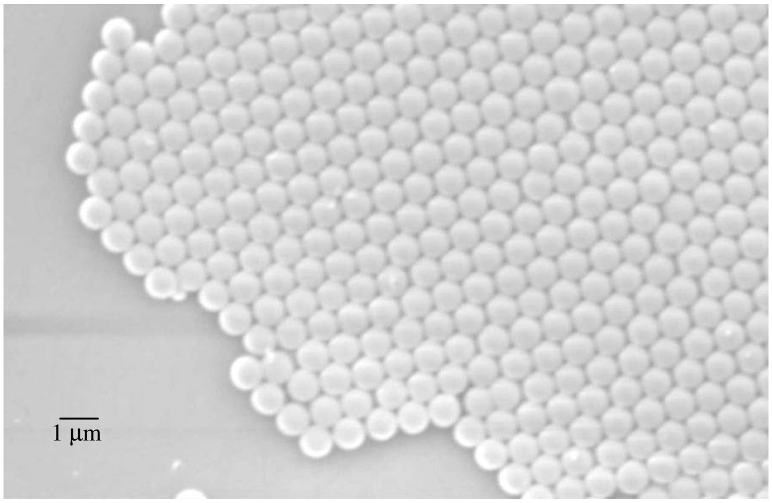

Figure 3.2: Scanning electron micrograph of the hexagonally closed pack monolayer of 640 nm silica spheres on silicon.

As the whole setup is tilted at an angle of 10°, the evaporation starts from the top of the sample and progressively moves to the bottom of the sample until it is completely dry. The speed of evaporation and the quality of the resulting sample depends on this angle; 10° was used on all samples presented here. The deposition on the silicon substrate covered about 1 cm^2, but only around half of the area was covered by monolayers, which included a variety of defects that arise as a result of nanosphere poly-dispersity, site randomness, point defects, and line defects. The other half was the one where the evaporation took place at last, at the bottom of the sample. We believe that in such regions the remaining water concentrated impurities and the excess particles, creating multilayers and clusters. A scanning electron microscope image of the hexagonal close packed arrangement of 1.76 μm spheres are shown in Figure 3.2.

3.3.2 Experimental Setup

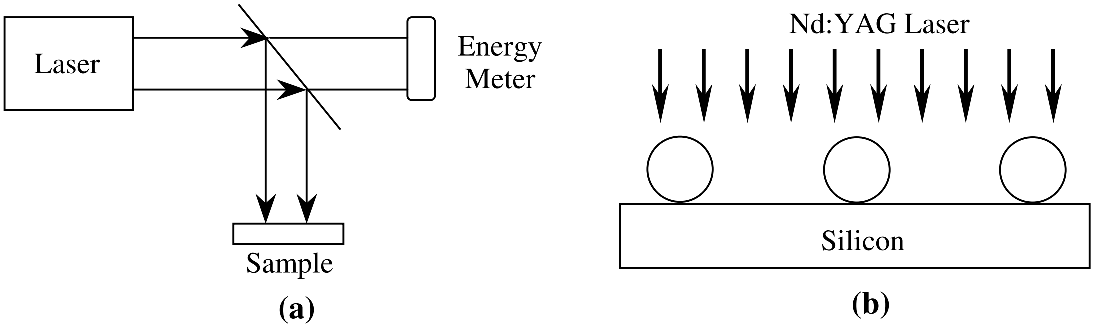

Figure 3.3: Laser irradiation of disperse silica spheres on silicon substrate: a) Schematic of the experimental setup, b) Schematic of silica microspheres on silicon

The schematic of our experimental setup is shown in Figure 3.3a. The output from a pulsed Nd:YAG laser passes through a beam splitter, which splits the incident laser beam into two - one part for patterning and the other for measuring the laser energy. The sample is mounted on a 3-D stage and the laser beam is focused onto the sample by using a plano-convex lens. A single pulse from the laser is incident on the spheres as shown in Figure 3.3b. Since the sphere is immediately on top of the substrate, the incident laser beam induces a near-field around the sphere. This enhanced field is responsible for the formation of nanofeatures on silicon. The features thus obtained were characterized using an SEM and are presented in the results and discussion section of the paper.

3.4 RESULTS AND DISCUSSION

The experiment is performed with two different spheres (1.76 µm and 640 nm diameter), two different laser wavelengths (532 nm and 355 nm) and various laser fluences and the scanning electron microscope images of the resulting features are presented and explained below.

3.4.1 Effect of Laser Energy

The experiment is performed using 1.76 μm SiO_2 spheres irradiated by a single 532 nm laser pulse at four fluences: 50, 100, 200, and 300 mJ/cm^2. The features thus created are characterized using an SEM. The experimental results are then compared with the simulation results. There are essentially two points of comparison between the SEM micrographs and the simulation results: the size of the surface damage, and the threshold energy below which no damage occurs.

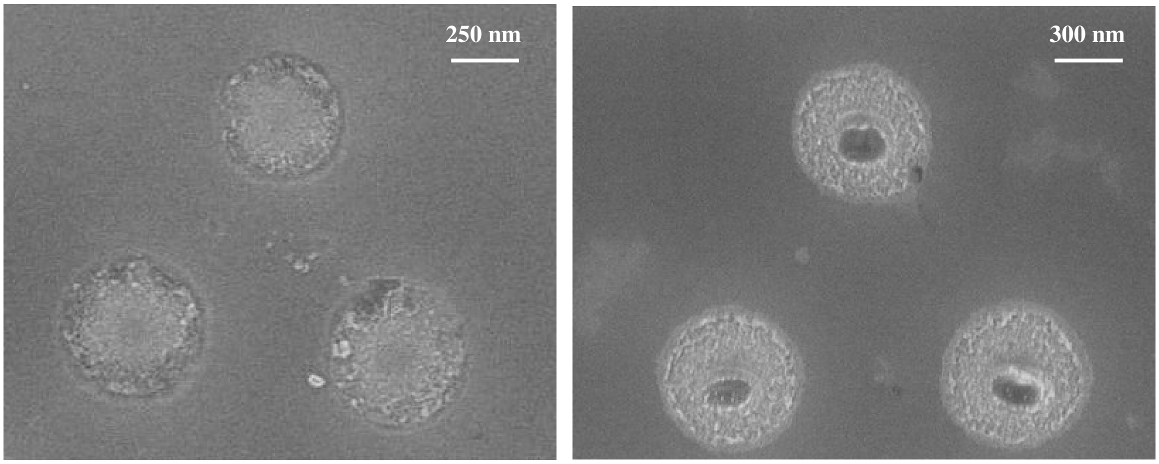

Figure 3.4: SEM micrograph of 1.76 μm SiO_2 spheres irradiated by 532 nm laser at a fluence of (a) 50 mJ/cm^2, (b) 100 mJ/cm^2.

Figure 3.4a is an SEM micrograph of the silicon substrate after irradiation with 50 mJ/cm^2 laser fluence. The diameter of the features obtained at this fluence is approximately 600 nm, and observing the extent of surface damage it is evident that the substrate barely reaches the melting temperature. This is confirmed by the numerical model (Appendix – 1), which predicts a melt zone of only a few nm wide, and a mushy or heat-affected zone approximately 430 nm wide. Figure 3.4b is an SEM picture of the 700 nm features obtained at a fluence of 100 mJ/cm^2. At this fluence, the model predicts a melt zone approximately 332 nm in diameter, with a total heat affected region of 548 nm diameter. At these low fluences, there is a 20% disagreement in feature diameters obtained experimentally and numerically. This could be due to fluctuations in the laser energy used in the experiments.

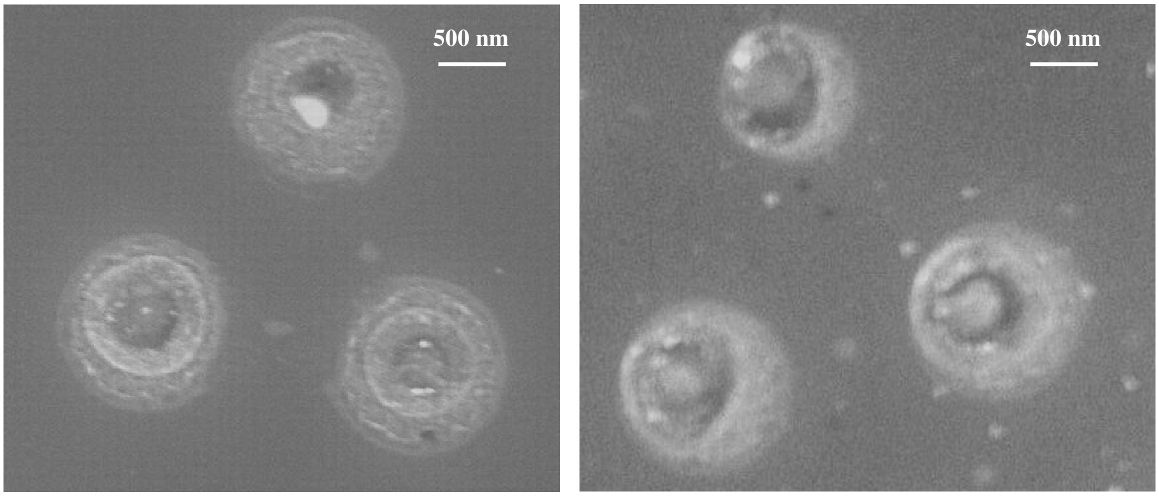

Figure 3.5: SEM micrograph of 1.76 μm SiO_2 spheres irradiated by 532 nm laser at a fluence of (a) 200 mJ/cm^2, and (b) 300 mJ/cm^2.

However, the agreement between the experimental and numerical results improved significantly at higher laser fluences. The diameter of the features obtained experimentally is approximately 1000 nm at 200 mJ/cm^2 and 300 mJ/cm^2, and an SEM image of this is shown in Figure 3.5. At 200 mJ/cm^2, the numerical model predicts a melt zone approximately 528 nm in diameter, with a heat affected region 939 nm in diameter. According to the model, at 300 mJ/cm^2, the diameter of the melt zone increases to approximately 645 nm, with a total heat affected zone of 958 nm in diameter. Also, it can be observed that some of the features obtained are not perfectly circular as predicted.

This is mainly because of the slight variation in the laser incident angle due to the beam delivery optics used in the experiment. A direct comparison of the feature diameters between the predicted and experimental results is shown in Figure 3.6.

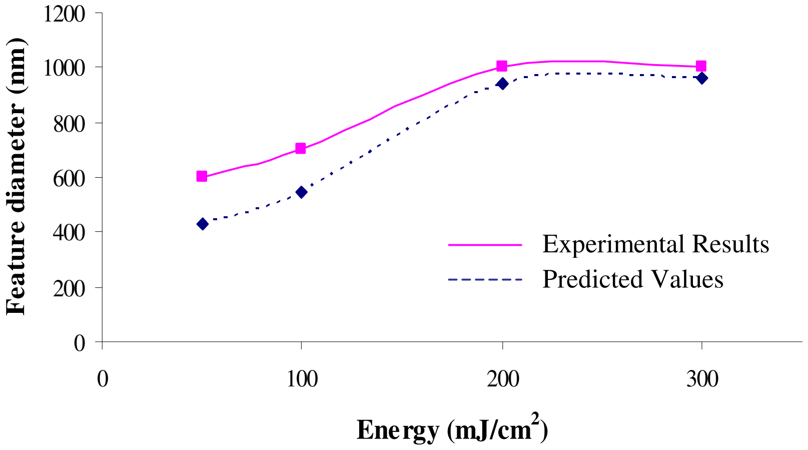

Figure 3.6: Comparison of the predicted and experimental feature diameters for 1.76 µm SiO_2 spheres irradiated by 532 nm laser at different laser fluences.

Both the extent of the surface modification and the damage threshold observed experimentally are very close to the predicted results. The experimental results show very little damage to the substrate when the particles are irradiated at a fluence of 50 mJ/cm^2, and by comparing with the modeling results it is evident that this energy is very close to the threshold below which no damage to silicon occurs. An additional comparison was made at a fluence of 40 mJ/cm^2, where the model predicted a peak temperature below the melting point of silicon. This is a strong indication that the level of enhancement obtained from the electromagnetic field calculations was accurate.

3.4.2 Effect of Laser Wavelength

In order to understand the effect of laser wavelength on the features formed on silicon, the experiment is performed with two different laser wavelengths – 532 nm and

355 nm respectively. As before a monolayer of 1.76 μm silica spheres are deposited on the silicon surface and irradiated with the laser beam of energy density 50 mJ/cm^2. Then the sample is cleaned in an ultra-sonicator to remove the left over spheres from the silicon substrate.

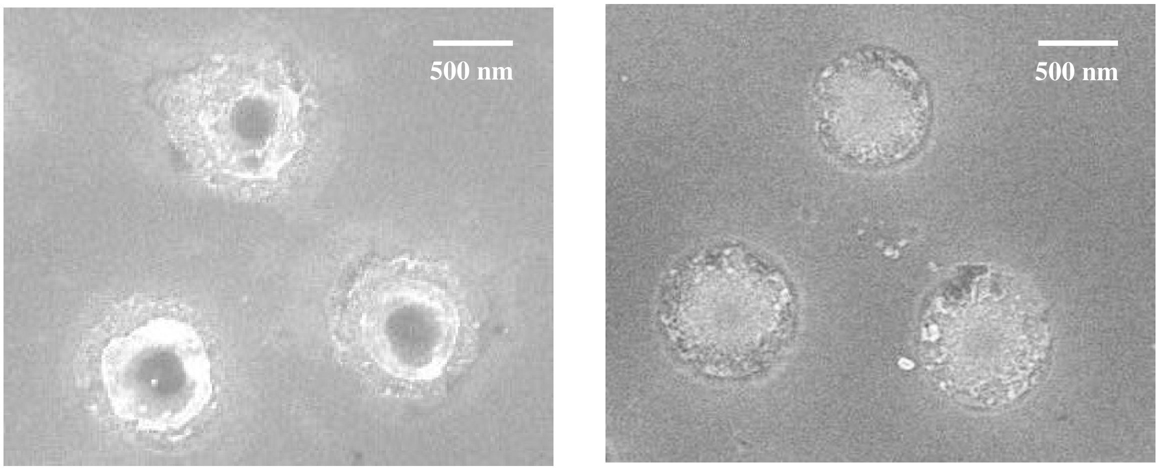

Figure 3.7: SEM micrograph of 1.76 μm SiO_2 spheres irradiated at a fluence of 50 mJ/cm^2 with a) 355 nm laser b) 532 nm laser.

Figure 3.7 is a scanning electron micrograph of the features obtained on silicon by irradiating 1.76 μm spheres with a 355 nm and 532 nm laser respectively. From the SEM images, it is obvious that the diameter of the features created remain the same in both cases. This clearly shows that the size of the sphere used in the experiment dictates the diameter of the features obtained. Since both the images are obtained with the same sphere sizes, the feature dimensions remained at around 650 nm.

However, the morphology of the features obtained is different in both cases. The features obtained with a 355 nm laser are well defined and deeper compared to that obtained with a 532 nm laser. This is mainly because of two reasons. The first reason is the higher absorption of silicon at 355 nm wavelength compared to 532 nm wavelength.

As a result more energy is absorbed in the case of 355 nm, and hence the resulting features are deeper. Also, Mie theory calculations show that the field enhancement is higher with 1.76 µm spheres and a 355 nm laser. So, more energy is deposited on to the silicon substrate. Higher field enhancement combined with higher absorption of silicon at 355 nm results in deeper features.

3.4.3 Effect of Sphere Size

Two different spheres of 640 nm and 1.76 µm are used to understand the effect of sphere size on the features obtained. A comparison of the features obtained with both 640 nm and 1.76 µm spheres using a 532 nm laser at a fluence of 200 mJ/cm^2 is shown in Figure 3.8. The diameter of the features obtained with 640 nm is around 300 nm, and with 1.76 µm spheres, the feature diameter is approximately 700 nm. In both cases the feature dimension is approximately half the diameter of the sphere used.

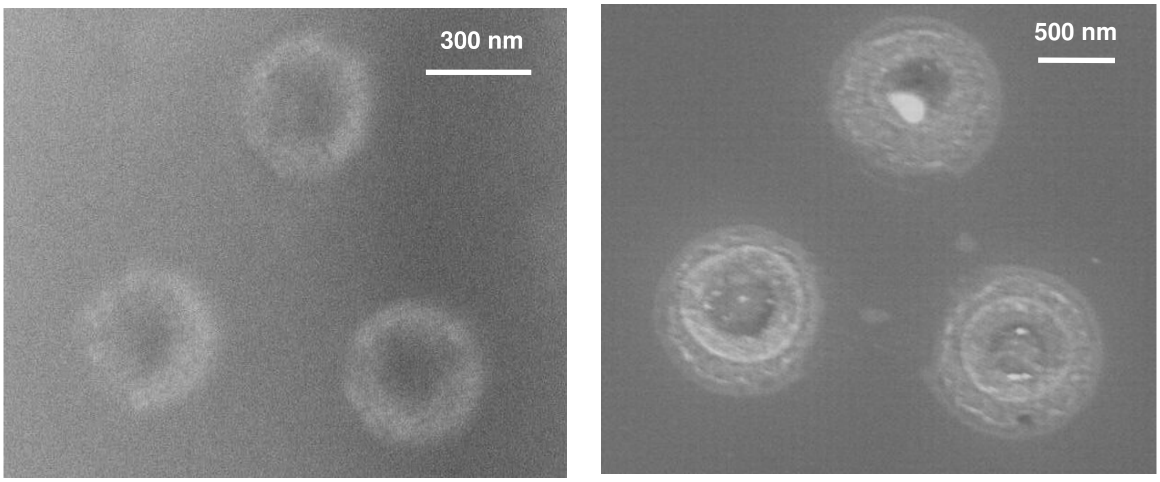

Figure 3.8: SEM micrograph of features obtained by the irradiation of a 532 nm laser at 200 mJ/cm2 fluence of a) 640 nm SiO_2 spheres, b) 1.76 µm SiO_2 spheres.

As the energy is increased to 300 mJ/cm^2, the same trend is observed, as shown in the SEM images of Figure 3.9. The diameter of the features increases slightly but is still approximately half the diameter of the spheres used in the experiment. Increasing the fluence further results in an increase in the heat affected zone and the features become irregular. Figure 3.10 is a plot showing the direct comparison of the feature dimensions obtained with a 532 nm laser at different fluences with both 640 nm and 1.76 µm spheres.

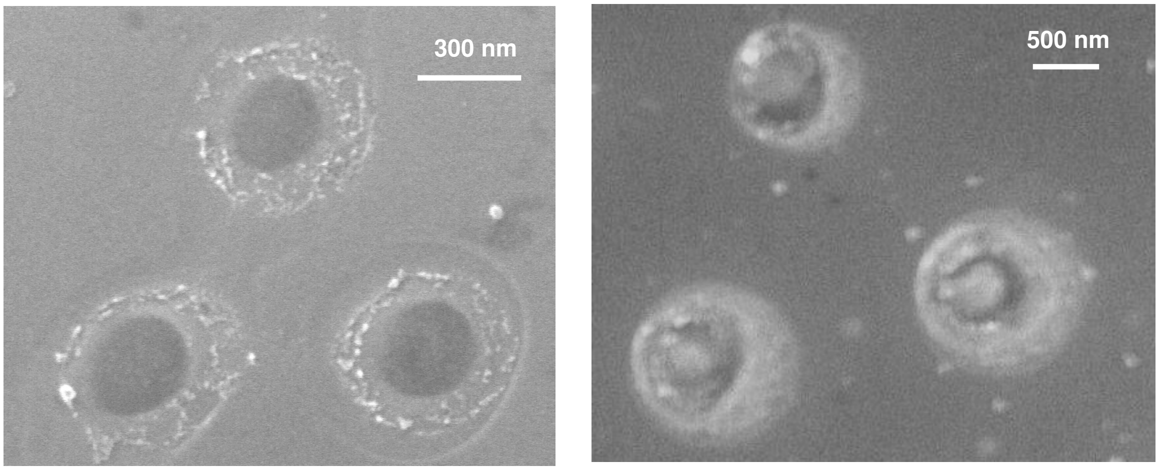

Figure 3.9: SEM micrograph of features obtained by the irradiation of a 532 nm laser at 300 mJ/cm2 fluence of a) 640 nm SiO_2 spheres, b) 1.76 µm SiO_2 spheres.

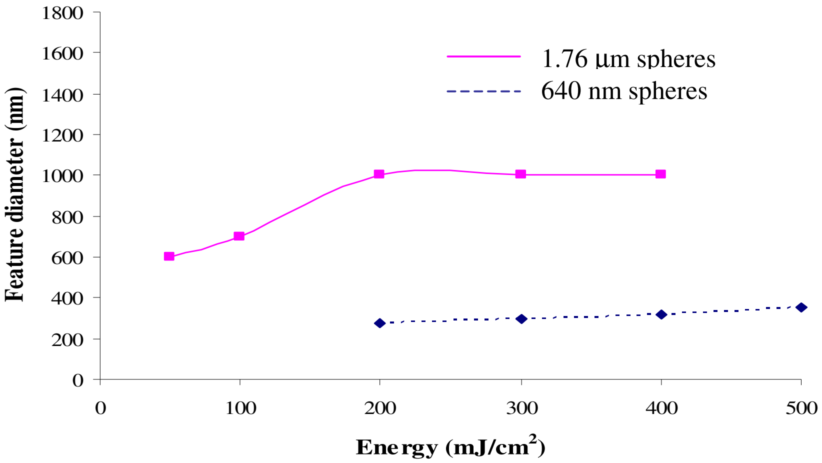

Figure 3.10: Comparison of the feature diameters obtained with a 532 nm laser at different fluences for 640 nm and 1.76 µm SiO_2 spheres.

3.4.4 Effect of Polarization

In order to study the effect of polarization on the features obtained, we used a half waveplate. Rotating the waveplate 45° changes the polarization from horizontal to vertical and vice versa. But changing the polarization did not have any effect on the features obtained. The morphology and size of the features remained the same.

3.5 CONCLUSIONS

Features created by the irradiation of microspheres on a silicon substrate surface with a pulsed laser have been presented. The features indicate an enhancement of the incident intensity in the near field due to the presence of nanospheres. The results of Mie theory calculations predict a strong enhancement directly under the sphere, which is assumed to be responsible for the substrate damage.

The experiments were performed for two different sphere sizes. It is found that the features obtained were approximately half the diameter of the spheres used. At a laser wavelength of 532 nm, approximately 1µm features were obtained with 1.76 µm spheres at laser fluences above 200 mJ/cm^2. However with 640 nm spheres, 300 nm features were obtained under the same laser wavelength and energy.

The effect of laser wavelength on the feature formation was also studied. Both 532 nm and 355 nm lasers were used to irradiate 1.76 µm spheres. The diameter of the features remained the same for both wavelengths. However, the depth of the features obtained with 355 nm was higher for the same energy. This is because of the higher absorption of silicon at 355 nm wavelengths and also due to the higher field enhancement with 355 nm laser and 1.76 µm spheres.

In order to study the effect of laser fluence on the features, various energy densities were used. For the irradiation of 1.76 µm spheres at 50 mJ/cm^2, the diameter of the features were approximately 700 nm and the diameter continued to increase with laser energy before reaching a maximum of 1000 nm. Further increase in energy resulted in more heat affected zone and disintegration of the features. With 640 nm spheres, the feature sizes increased from 275 nm at 200 mJ/cm^2 to 340 nm at 500 mJ/cm^2. As before with further increase in energy, the heat affected zone increased. Also, the polarization of the laser beam did not seem to have any effect on the features obtained. Both the morphology and size of the features obtained remained the same.

The experimental results are compared with the numerical results from a multidimensional, heat transfer model built by Heltzel et al. [1] to simulate the heat transfer through silicon. The experimental results correlate well with the predicted results. Also the threshold energy required to damage the substrate with the presence of nanospheres matches the level of enhancement predicted by the Mie theory calculations.

3.6 REFERENCES

1. Heltzel, A., Theppakuttai, S., Howell, J., Chen, S., "Analytical and Experimental Investigation of Laser-Microsphere Interaction for Nanoscale Surface Modification", *Journal of Heat transfer, in press*, (2005).
2. Petersen, K. E., "Silicon as a Mechanical Material", *Proceedings of the Ieee,* **70**, 420-457, (1982).
3. Yuan, B., and Sharpe, W. N., "Mechanical testing of polysilicon thin films with the ISDG", *Experimental Techniques,* **21**, 32-35, (1997).
4. Sharpe, W. N., Yuan, B., and Edwards, R. L., "A new technique for measuring the mechanical properties of thin films", *Journal of Microelectromechanical Systems,* **6**, 193-199, (1997).
5. Sharpe, W. N., Vaidyanathan, R., Yuan, B., Bao, G., and Edwards, R. L., "Effect of etch holes on the mechanical properties of polysilicon", *Journal of Vacuum Science & Technology B,* **15**, 1599-1603, (1997).
6. Lang, W., "Silicon microstructuring technology", *Materials Science & Engineering R-Reports,* **17**, 1-55, (1996).
7. Weller, D. et al., "Ion induced magnetization reorientation in Co/Pt multilayers for patterned media", *Journal of Applied Physics,* **87**, 5768-5770, (2000).
8. Terris, B. D., Weller, D., Folks, L., Baglin, J. E. E., Kellock, A. J., Rothuizen, H., and Vettiger, P., "Patterning magnetic films by ion beam irradiation", *Journal of Applied Physics,* **87**, 7004-7006, (2000).

9. Reyntjens, S., and Puers, R., "A review of focused ion beam applications in microsystem technology", *Journal of Micromechanics and Microengineering,* **11**, 287-300, (2001).

10. Rubanov, S., and Munroe, P. R., "FIB-induced damage in silicon", *Journal of Microscopy-Oxford,* **214**, 213-221, (2004).

11. Ali, M. Y., and Hung, N. P., "Surface roughness of sputtered silicon. II. Model verification", *Materials and Manufacturing Processes,* **16**, 315-329, (2001).

12. Ali, M. Y., and Hung, N. P., "Surface roughness of sputtered silicon. I. Surface modeling", *Materials and Manufacturing Processes,* **16**, 297-313, (2001).

13. Gago, R., Vazquez, L., Cuerno, R., Varela, M., Ballesteros, C., and Albella, J. M., "Nanopatterning of silicon surfaces by low-energy ion-beam sputtering: dependence on the angle of ion incidence", *Nanotechnology,* **13**, 304-308, (2002).

14. Schmidt, B., Bischoff, L., and Teichert, J., "Writing FIB implantation and subsequent anisotropic wet chemical etching for fabrication of 3D structures in silicon", *Sensors and Actuators a-Physical,* **61**, 369-373, (1997).

15. Prestigiacomo, M., Roussel, L., Houel, A., Sudraud, P., Bedu, F., Tonneau, D., Safarov, V., and Dallaporta, H., "Studies of structures elaborated by focused ion beam induced deposition", *Microelectronic Engineering,* **76**, 175-181, (2004).

16. Melngailis, J., Mondelli, A. A., Berry, I. L., and Mohondro, R., "A review of ion projection lithography", *Journal of Vacuum Science & Technology B,* **16**, 927-957, (1998).

17. Tseng, A. A., "Recent developments in nanofabrication using ion projection lithography", *Small,* **1**, 594-608, (2005).

18. Dial, O., Cheng, C. C., and Scherer, A., "Fabrication of high-density nanostructures by electron beam lithography", *Journal of Vacuum Science & Technology B,* **16**, 3887-3890, (1998).

19. Hu, S. F., Weng, W. C., and Wan, Y. M., "Fabrication of silicon nanowire structures based on proximity effects of electron-beam lithography", *Solid State Communications,* **130**, 111-114, (2004).

20. Borini, S., Rossi, A. M., Boarino, L., and Amato, G., "Patterning of porous silicon by electron-beam lithography", *Journal of the Electrochemical Society,* **150**, G311-G313, (2003).

21. Snow, E. S., and Campbell, P. M., "Fabrication of Si Nanostructures with an Atomic-Force Microscope", *Applied Physics Letters,* **64**, 1932-1934, (1994).

22. Bo, X. Z., Rokhinson, L. P., Yin, H. Z., Tsui, D. C., and Sturm, J. C., "Nanopatterning of Si/SiGe electrical devices by atomic force microscopy oxidation", *Applied Physics Letters,* **81**, 3263-3265, (2002).

23. Ara, M., Graaf, H., and Tada, H., "Atomic force microscope anodization of Si(111) covered with alkyl monolayers", *Japanese Journal of Applied Physics Part 1-Regular Papers Short Notes & Review Papers,* **41**, 4894-4897, (2002).

24. Santinacci, L., Djenizian, T., and Schmuki, P., "Atomic force microscopy-induced nanopatterning of Si(100) surfaces", *Journal of the Electrochemical Society,* **148**, C640-C646, (2001).

25. Campbell, P. M., Snow, E. S., and McMarr, P. J., "AFM-based fabrication of Si nanostructures", *Physica B,* **227**, 315-317, (1996).

26. Snow, E. S., Campbell, P. M., and McMarr, P. J., "AFM-based fabrication of free-standing Si nanostructures", *Nanotechnology,* **7**, 434-437, (1996).

27. Matsumoto, K., Takahashi, S., Ishii, M., Hoshi, M., Kurokawa, A., Ichimura, S., and Ando, A., "Application of Stm Nanometer-Sire Oxidation Process to Planar-Type Mim Diode", *Japanese Journal of Applied Physics Part 1-Regular Papers Short Notes & Review Papers,* **34**, 1387-1390, (1995).

28. Held, R., Vancura, T., Heinzel, T., Ensslin, K., Holland, M., and Wegscheider, W., "In-plane gates and nanostructures fabricated by direct oxidation of semiconductor heterostructures with an atomic force microscope", *Applied Physics Letters,* **73**, 262-264, (1998).

29. Salling, C. T., "Direct patterning of Si(001) surfaces by atomic manipulation", *Journal of Vacuum Science & Technology B,* **14**, 1322-1326, (1996).

30. Iwasaki, H., Yoshinobu, T., and Sudoh, K., "Nanolithography on SiO_2/Si with a scanning tunnelling microscope", *Nanotechnology,* **14**, R55-R62, (2003).

31. Dumas, P., Gu, M., Syrykh, C., Hallimaoui, A., Salvan, F., and Gimzewski, J. K., "Nanostructuring of Porous Silicon Using Scanning-Tunneling-Microscopy", *Journal of Vacuum Science & Technology B,* **12**, 2067-2069, (1994).

32. Abeln, G. C., Lee, S. Y., Lyding, J. W., Thompson, D. S., and Moore, J. S., "Nanopatterning organic monolayers on Si(100) by selective chemisorption of norbornadiene", *Applied Physics Letters,* **70**, 2747-2749, (1997).

33. Oishi, T., Goto, A., Pihosh, Y., Kasahara, A., and Tosa, A., "Silicon microstructure fabricated by laser micro-patterning method combined with wet etching process", *Applied Surface Science,* **241**, 223-226, (2005).

34. Mucklich, F., Lasagni, A., and Daniel, C., "Laser interference metallurgy-periodic surface patterning and formation of intermetallics", *Intermetallics,* **13**, 437-442, (2005).

35. Mei, P., Boyce, J. B., Lu, J. P., Ho, J., and Fulks, R. T., "Pulsed laser crystallization and doping for thin film transistors", *Journal of Non-Crystalline Solids,* **266**, 1252-1259, (2000).

36. Huang, S. M., Hong, M. H., Luk'yanchuk, B. S., Lu, Y. F., Song, W. D., and Chong, T. C., "Sub-50 nm nanopatterning of metallic layers by green pulsed laser

combined with atomic force microscopy", *Journal of Vacuum Science & Technology B,* **20**, 1118-1125, (2002).

37. Li, L. P., Lu, Y. F., Doerr, D. W., Alexander, D. R., Shi, J., and Li, J. C., "Fabrication of hemispherical cavity arrays on silicon substrates using laser-assisted nanoimprinting of self-assembled particles", *Nanotechnology,* **15**, 333-336, (2004).

38. Huang, S. M., Hong, M. H., Lu, Y. F., Lukyanchuk, B. S., Song, W. D., and Chong, T. C., "Pulsed-laser assisted nanopatterning of metallic layers combined with atomic force microscopy", *Journal of Applied Physics,* **91**, 3268-3274, (2002).

39. Leviatan, Y., "Study of near-Zone Fields of a Small Aperture", *Journal of Applied Physics,* **60**, 1577-1583, (1986).

40. Betzig, E., and Trautman, J. K., "Near-Field Optics - Microscopy, Spectroscopy, and Surface Modification Beyond the Diffraction Limit", *Science,* **257**, 189-195, (1992).

41. Ohtsu M., a. H. H., *Near-field Nano-optics* (Kluwer Academic, New York, 1999).

42. Halfpenny, D. R., and Kane, D. M., "A quantitative analysis of single pulse ultraviolet dry laser cleaning", *Journal of Applied Physics,* **86**, 6641-6646, (1999).

43. Hasegawa, M., Ikawa, T., Tsuchimori, M., Watanabe, O., and Kawata, Y., "Topographical nanostructure patterning on the surface of a thin film of polyurethane containing azobenzene moiety using the optical near field around polystyrene spheres", *Macromolecules,* **34**, 7471-7476, (2001).

44. Watanabe, O., Ikawa, T., Hasegawa, M., Tsuchimori, M., Kawata, Y., Egami, C., Sugihara, O., and Okamoto, N., "Transcription of near-field induced by photo-irradiation on a film of azo-containing urethane-urea copolymer", *Molecular Crystals and Liquid Crystals,* **345**, 629-634, (2000).

45. Ikawa, T., Mitsuoka, T., Hasegawa, M., Tsuchimori, M., Watanabe, O., and Kawata, Y., "Azobenzene polymer surface deformation due to the gradient force of the optical near field of monodispersed polystyrene spheres", *Physical Review B,* **64**, -, (2001).

46. Lu, Y., Theppakuttai, S., and Chen, S. C., "Marangoni effect in nanosphere-enhanced laser nanopatterning of silicon", *Applied Physics Letters,* **82**, 4143-4145, (2003).

47. Moreno, F., and Gonzalez, F., *Light Scattering from Microstructures* (Springer, 1998).

48. Munzer, H. J., Mosbacher, M., Bertsch, M., Zimmermann, J., Leiderer, P., and Boneberg, J., "Local held enhancement effects for nanostructuring of surfaces", *Journal of Microscopy-Oxford,* **202**, 129-135, (2001).

49. Watanabe, O., Ikawa, T., Hasegawa, M., Tsuchimori, M., and Kawata, Y., "Nanofabrication induced by near-field exposure from a nanosecond laser pulse", *Applied Physics Letters,* **79**, 1366-1368, (2001).

50. Fischer, U. C., and Zingsheim, H. P., "Sub-Microscopic Pattern Replication with Visible-Light", *Journal of Vacuum Science & Technology,* **19**, 881-885, (1981).

51. Morita, M., Matsumoto, M., Usui, S., Abe, T., Denkov, N., Velev, O., and Ivanov, I. B., "Interfacial Properties and Emulsion Stability in Fluorinated Oil Nonfluorinated Oil Surfactant(S) Systems", *Colloids and Surfaces,* **67**, 81-93, (1992).

52. Velev, O. D., Denkov, N. D., Paunov, V. N., Kralchevsky, P. A., and Nagayama, K., "Capillary Image Forces .2. Experiment", *Journal of Colloid and Interface Science,* **167**, 66-73, (1994).

53. Kralchevsky, P. A., Paunov, V. N., Denkov, N. D., and Nagayama, K., "Capillary Image Forces .1. Theory", *Journal of Colloid and Interface Science,* **167**, 47-65, (1994).

Chapter 4: Nanoscale Processing of Glass with Optical Near Field

4.1 ABSTRACT

In this chapter, the nano-scale surface modification of borosilicate glass when irradiated by a nanosecond Nd:YAG laser (10 ns, 1064 nm), using silica nanospheres is reported. At very low energy densities, sub-micron ripples are created on the glass surface. The ripples thus obtained do not satisfy Rayleigh's diffraction condition in that a) the ripple spacing is different from the value predicted by the classical model, b) the spacing is independent of the incident angle, and c) the orientation is not always perpendicular to the laser polarization. Also, the ripple characteristics are not dependent on the diameter of the spheres used and the ripples have almost the same periodicity irrespective of the experimental parameters. However, at higher energy densities hexagonally arranged nanofeatures 350 nm in diameter are formed on the substrate instead of the ripples. Nonlinear absorption of the enhanced optical field between the spheres and glass sample is believed to be the primary reason for the creation of nano-features on the glass substrate.

4.2 INTRODUCTION

The enormous potential of borosilicate glasses has resulted in widespread applications in packaging and micro-technologies like micro-optics and biomedical devices [1]. In addition to their outstanding chemical, optical and mechanical properties, borosilicate glasses also have the thermo-mechanical stability necessary for replication processes. This has led to many investigations on the processing characteristics of these dielectric materials. In general, due to their inert nature, they are very difficult to machine by most conventional machining techniques. Laser micromachining is an attractive approach for the machining of glass materials. However, the linear absorption for glasses is very low in the visible range and the absorption edge is near 310 nanometers [2]. Therefore, high power UV and CO_2 lasers have to be used for processing glass materials. The mechanism of bulk damage by nanosecond pulses involves heating of conduction band electrons by the incident radiation and transfer of this energy to the lattice [3]. Damage occurs via conventional heat deposition resulting in melting and boiling of the dielectric material. Also, the very low absorption cross section of these large band-gap materials requires very high laser intensities in order to obtain sufficient energy absorption in the material to observe macroscopic material removal [4]. This high intensity leads to a large heat-affected zone and thermal stress build up which might even lead to cracking, eventually making this technique not suitable for micro-system technology.

A possible method to overcome this limitation is by employing ultrafast laser pulses for processing. Due to the short pulse duration, the heating time is less than the electron-phonon relaxation time, thereby improving the spatial resolution and reducing the heat-affected zone to a few micrometers [5]. Furthermore, it has been found that femtosecond infrared laser irradiation results in an increase in the refractive index at the focal point inside the glass substrate [6]. Other techniques such as laser-induced plasma-assisted ablation and laser induced backside etching [7] have also been recently used for processing transparent glasses.

A phenomenon frequently observed during the illumination of solid surfaces with a single uniform laser beam of sufficient intensity is the appearance of spontaneous periodic surface structures or ripples. These grating like damage patterns have been produced on the surfaces of a variety of materials [8, 9] as well as within the bulk of dielectrics using continuous wave (cw) to femtosecond laser sources operating over a wide range of wavelengths (0.17 - 10.6 μm). Very similar ripples are also observed in a large variety of experiments on laser-assisted film growth [10] laser etching [11, 12], photo-deposition [13, 14], and other laser material processing [15]. Quite frequently ripples are seen at incident laser energies just below the damage threshold for the material, indicating that high intensities are not necessary for ripple production. Due to the wide variety of experimental conditions under which these ripples have been produced, several mechanisms have been proposed to explain the observation of ripples. For example, suggestions have been put forward involving laser-acoustic-mode coupling [16], driven surface plasmons [17], or even Bose-Einstein condensation of bulk plasmons [18].

Although it is possible to form ripples with single pulses, the patterns so formed can be influenced by the presence of isolated defects or scratches. The observation of fringes near a scratch indicate that at least for a wide class of materials surface roughness is responsible for the symmetry breaking necessary to produce periodic surface damage. The ripple spacing is λ for semiconductors and metals, whereas those observed on wide bandgap dielectrics are spaced at λ / n for normal incidence, where λ is the wavelength of the laser, and n is the index of refraction [19]. Another model which takes into account the polarization charge induced on the boundaries of defects by the applied field has also been proposed. According to this model, linearly polarized radiation incident upon linear defects aligned perpendicular to the polarization direction produced the largest perturbation, while the perturbation was zero for defects running parallel to the incident polarization direction [20].

During laser surface melting and alloying, ripples have been observed on surfaces of metals and alloys. These ripples can result from the vapor pressure above the molten film depressing the film [21], surface tension of the molten film pushing the liquid film in a nonplanar meniscus shape, and the shear stresses on the molten film caused by gradients in surface tension of the liquid film [22]. In case of fused silica under normal incidence of linearly polarized light from a pulsed CO_2 laser, the fundamental mechanism of ripple formation is attributed to the generation of capillary waves owing to vapor recoil pressure and nonuniform removal of substance from the surface by evaporation [23].

Ripples have also been observed in photochemically deposited thin metal films. In photodeposited carbon films, the ripple generation is associated with irradiation near strong absorption bands of the parent and product compounds together with dipolar scattering [24]. However, it is generally agreed that in most metallic films, the ripple formation involves scattering of the incident waves into surface waves. The spatial modulation of optical intensity resulting from the interference between the incident wave and surface-plasma-waves (SPW) promotes the exponential growth of ripples, which increase the scattering into SPW thereby creating a positive feedback effect. The scattered spatial frequency component having the largest exponential gain ultimately dictates the final ripple structure upon solidification of the material [25].

In nearly all of the above mentioned work, the crests and valleys of the ripples are mostly found to run perpendicular to the incident electric field. The ripple period can be calculated with an accuracy of a few percent from Rayleigh's diffraction criterion as given by [8]

$$\Lambda = \frac{\lambda}{n_0[1 \pm \sin\theta]}, \tag{5.1}$$

where λ is the laser wavelength, n_0 is the refractive index of the medium and θ is the angle of incidence measured from the normal to the surface.

In this work, we observe sub-micron features when a monolayer of silica nanospheres are deposited on a glass substrate and exposed to laser radiation from the glass side. The experiments are performed for different laser energies, sphere sizes, varying the angle of incidence and laser polarization. Finally, a scanning electron microscope and an atomic force microscope are used to characterize the ripples.

4.3 EXPERIMENTAL SETUP

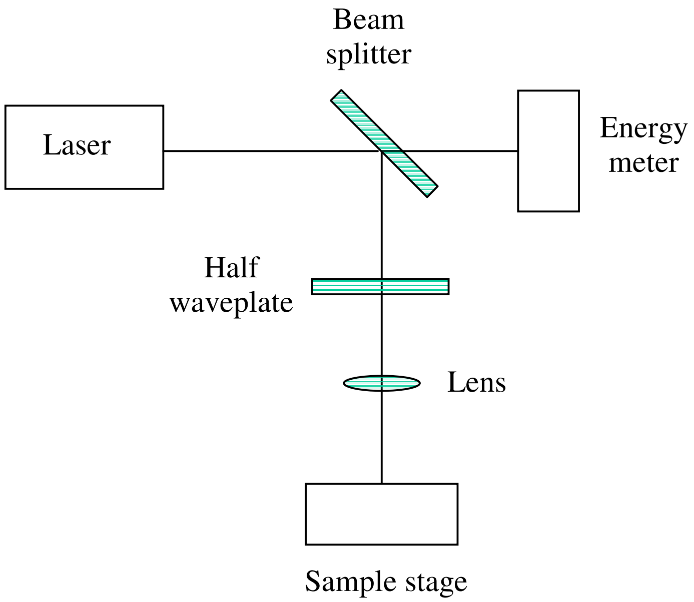

Figure 4.1: Schematic of the experimental setup.

The schematic of the experimental setup is shown in Figure 4.1. A 1064 nm Nd:YAG laser of 12 ns pulse width is used as the illumination source in the experiment. The output laser beam, which is s-polarized, is split into two beams by using a beam splitter. One part of the beam is used for measuring the laser energy with the help of an energy-meter and the other part is passed through a half waveplate mounted on a rotary mount. Rotating the waveplate changes the polarization of the incoming beam from s-polarization to p-polarization and vice versa. The laser beam coming out of the waveplate is then focused onto the sample, using a plano-convex lens. The sample is loaded on a 3-D stage capable of motion in all three directions.

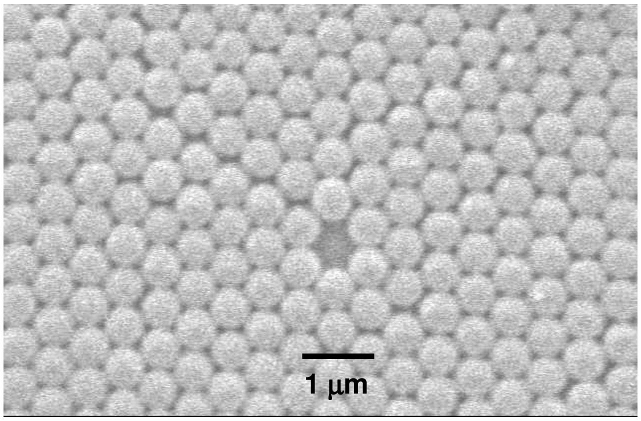

Figure 4.2: SEM micrograph of a monolayer of 640 nm silica nanospheres on glass substrate.

The sample used in the experiment is borosilicate glass of thickness 500 µm. The wafers are well polished and hence the surface roughness is in nanometer scale (< 2 nm). The samples are cleaned in ethanol solution followed by rinsing in deionized water to make sure the sample is clean and free of any contaminants. After the samples are dried with nitrogen gas, an aqueous solution of monodispersed silica nanospheres (1.76 µm and 640 nm diameter) diluted with deionized water is applied on the glass sample. After the evaporation of water, the nanospheres reorganize and form a hexagonally closed-packed monolayer on the glass substrate by means of a self-organizing process [26]. An SEM micrograph of the hexagonal arrangement of spheres is shown in Figure 4.2.

After confirming the hexagonal monolayer arrangement, the glass samples are exposed to the laser beam from the back side as shown in Figure 4.3. Borosilicate glass is transparent to the wavelength used in the experiment and hence the laser beam passes through the glass substrate and is incident on the bottom side of the monolayer of spheres. When the nanospheres are illuminated by the laser beam, the incident light intensity is enhanced and an optical near-field is produced around the spheres. As a result, periodic grating like structures are created on glass and the ripple characteristics are studied in detail using an optical microscope, SEM and AFM.

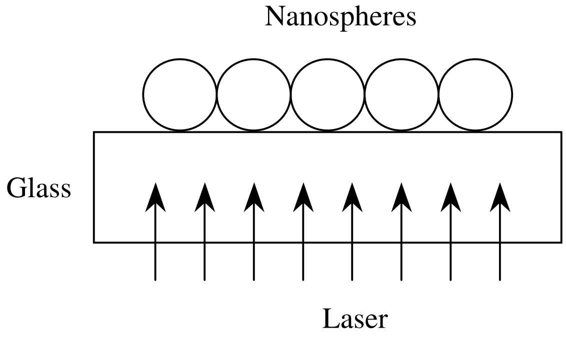

Figure 4.3: Schematic of the irradiation of silica spheres on glass from the backside

4.4 RESULTS AND DISCUSSION

The experiment is performed with two different sphere diameters (640 nm and 1.76 µm diameter), two different laser polarizations (s and p-polarization), various incident angles (0^o and 45^o) and various laser fluences in order to understand the role of each of these parameters. Then an atomic force microscope and a scanning electron microscope were used to characterize the features obtained and the resulting images are presented and explained below.

4.4.1 Effect of Sphere Size

A monolayer of 640 nm nanospheres was deposited on the glass substrate as described earlier. A single pulse from the 1064 nm laser beam with a fluence of 10 mJ/cm^2 is irradiated from the glass side at an incident angle of 0^o. The spheres are ejected from the glass surface and periodic surface structures are formed on the surface of the glass substrate. These structures are characterized by long, parallel lines extending over the entire laser exposed area as shown in Figure 4.4.

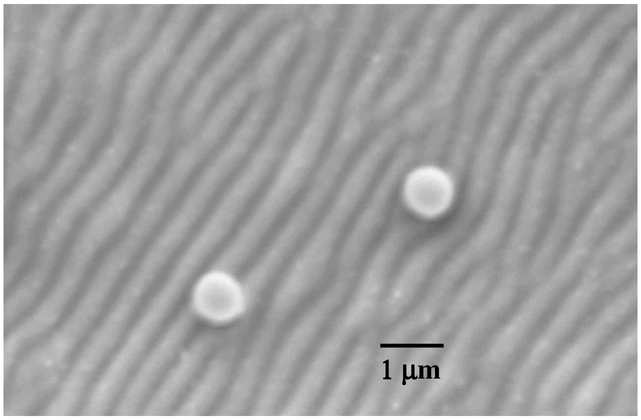

Figure 4.4: SEM micrograph of the ripples extending over the entire laser exposed area for 640 nm spheres at 0° incidence of an s-polarized laser beam.

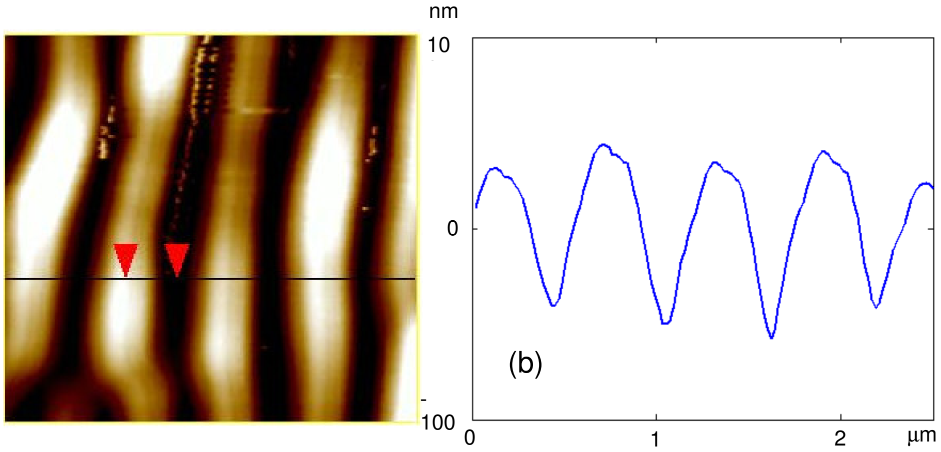

Figure 4.5: AFM traces showing the cross section profile of ripples created with 1.76 µm spheres for 0° incidence of an s-polarized laser: (a) surface topography, and (b) cross section profile.

The periodicity of the ripples (horizontal spacing between two crests or valleys) thus created is found to be 450 nm. AFM cross section of the surface shows that the ripples are indeed undulations of the surface and the profile varies sinusoidally with an amplitude variation of around 80 nm.

To better understand the ripple formation mechanism and to study the effect of sphere diameter, we repeated the experiments with 1.76 µm diameter spheres. It is found that the diameter of the spheres does not influence the ripple characteristics i.e. the spacing and amplitude remain 450 nm and 80 nm respectively. An AFM picture showing the surface topography and the cross section profile is presented in Figure 4.5.

4.4.2 Effect of Incident Angle

In order to study the effect of incident angle on the ripple characteristic, the laser beam is illuminated on the glass sample at 0^o and 45^o angle of incidence. At a laser fluence of 10 mJ/cm^2, the ripples obtained remained identical irrespective of the incident angle. The periodicity of the ripples was again found to be around 450 nm, and the amplitude of the ripples was approximately 80 nm. This shows that, the effect of incident angle on the ripples were negligible.

4.4.3 Effect of Polarization

The experiment is repeated with 1.76 µm spheres for both the horizontal and vertical polarizations. The laser energy is kept constant at 10 mJ/cm^2, and the angle of incidence is maintained at 0^o (normal incidence from the back side of glass). For an s-polarized beam (vertical polarization) the ripples are oriented perpendicular to the electric field (E). In case of a p-polarized beam (horizontal polarization), the arrangement of the ripples are parallel to the electric field. This means that, irrespective of the polarization direction, the ripples are always oriented in the same direction. Studying the ripples with a scanning electron microscope and an atomic force microscope show that, the ripple spacing is 450 nm for both polarizations and the amplitude is approximately 80 nm for both cases. An AFM image of the ripples obtained with 1.76 μm spheres for 0° incidence of a p-polarized laser beam is presented in Figure 4.6.

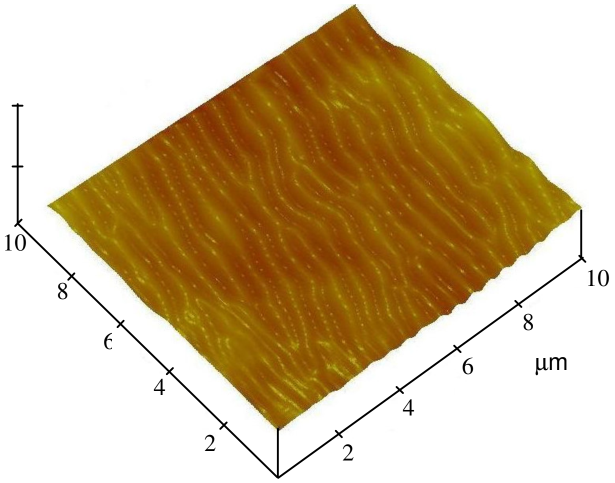

Figure 4.6: AFM image of the ripples created with 1.76 μm diameter spheres at 45° incidence of a p-polarized laser beam.

Thus the ripple formation mechanisms proposed earlier do not provide a satisfactory explanation for the ripples observed in our experiment. Also for dielectrics, no surface excitations like surface plasmons exist in the visible or near infrared, and for these materials a wave propagating parallel to the surface with a wavelength λ or indeed with any wavelength does not satisfy the Maxwell boundary conditions across the interface [27].

In laser ablation of wide bandgap transparent dielectrics using an ultrafast laser pulse, multiphoton surface ionization followed by Coulomb explosion of positive ions from an electrostatically unstable surface is believed to be the prominent mechanism for material removal [28, 29]. In patterning using nanospheres, it has been shown that the enhanced optical near-field could be several orders of magnitude higher than the original incident intensity. Since the linear absorption coefficient of glass is very low at the experimental wavelength, the pattern formation is due to nonlinear absorption of the enhanced optical field by the glass material. Although the physical mechanisms responsible for infrared photosensitivity are still under investigation, the process is believed to be initiated by a multiphoton absorption process and therefore exhibits a highly nonlinear dependence on the intensity of the illuminating beam [30, 31]. These intensity-dependent changes in the material's optical properties affect the propagation of the incident light. The refractive part of the nonlinearity gives rise to self-lensing, which can lead to optical damage. The absorptive part of the nonlinearity can decrease the transmittance at high intensity and provide a path for optical damage in the material at lower irradiances than conventional dielectric breakdown [32, 33]. Also the presence of a surface breaks the inversion symmetry of the medium normal to the boundary and makes nonlinear interaction possible [34].

In this work, the enhanced optical field around the spheres results in an electrostatically unstable surface due to multiphoton ionization, finally leading to an explosive emission of ions. However, the whole electrostatically driven ablation mechanism comes against the idea of ripple formation, which corresponds to a phase transition. Therefore as suggested by Reif et al [35-37], the generation of a strongly perturbed surface in an extremely short time leads to a self-organization process during the relaxation of the surface instability. Thus we believe self-organization mechanism to be the main cause for the formation of ripples. Though this model cannot explain the role of polarization, investigation to support this view is currently underway.

4.4.4 Effect of Laser Energy

In order to study the effect of laser intensity on the features obtained, the glass substrate with the 640 nm nanospheres is exposed to a single pulse of 3 J/cm^2, at an incident angle of 0^o. The ripples were observed only for very low laser fluences, and with

3 J/cm^2 a periodic array of holes 350 nm in diameter were formed on the surface. A scanning electron micrograph of this is shown in Figure 4.7. The created features are arranged hexagonally and the distance between the centers of the features is about 640 nm which is the same as the diameter of the spheres used. This confirms the formation of features underneath the location of spheres. As explained earlier, the pattern formation is due to nonlinear absorption of the enhanced optical field by the glass material.

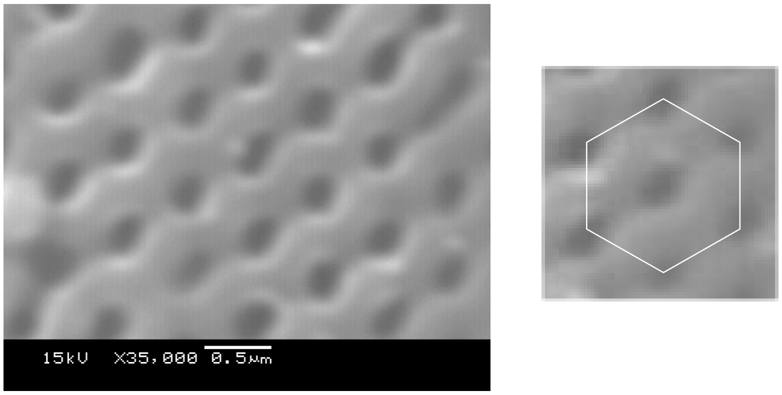

Figure 4.7: SEM image of hexagonally arranged dents on borosilicate glass produced using 640 nm silica nanospheres with a laser fluence of 3 J/cm^2.

The optical field enhancement could arise from several sources. Scattering and near-field effects are the obvious ones as demonstrated by previous work when the laser beam was incident on the top surface of the spheres [38-41]. Calculation of the field enhancement around the spheres illustrates that both focusing effects as well as near-field effects contribute to the size and shape of the features formed underneath the spheres. But when the sample is irradiated from the backside, the scattering effect is minimized. We calculated the intensity enhancement due to scattering by the dielectric spheres according to Mie theory for a laser wavelength of 1064 nm and 640 nm silica spheres with a refractive index of 1.39. The intensity enhancement as a function of the scattering angle is plotted in Figure 4.8. The calculations show that there is no significant intensity enhancement due to scattering for angles between 90° and 270°. This means that, at the interface between the sphere and the glass substrate, the field enhancement is not due to scattering.

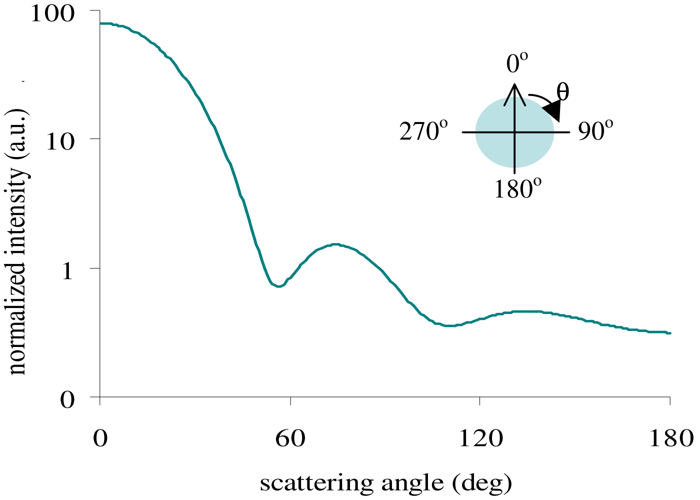

Figure 4.8: Calculated scattering intensity distribution around the nanosphere for 1064nm incident laser beam on a 640 nm silica nanosphere.

The optical field enhancement could also come from the rear surface interference effect. Due to the interference of the incoming and reflected waves, the electric field strength is higher at the rear side of a weakly absorbing slab with n>1, so that optical breakdown threshold is lower at the rear side [42]. Rear surface ablation has been previously reported for fused silica and borosilicate glasses at 193 nm, which is very well absorbed by these glasses. Despite this enhancement on the rear side, no damage was observed at the rear side in the experiments performed with 1064 nm laser in the absence of spheres at similar laser fluences. This confirms the role of nanospheres in the formation of nano-features.

4.5 CONCLUSIONS

Sub-micron features were created on glass by depositing a monolayer of silica nanospheres and irradiating with a laser beam from the back side. At very low laser fluences, periodic surface structures that are characterized by long parallel lines were observed. The spacing of the ripples obtained in the experiment does not satisfy the Rayleigh's diffraction criterion. The spacing was found to be 450 nm and the amplitude of the ripples was approximately 80 nm. This is different from the earlier predictions by the Rayleigh's diffraction criterion.

The effect of the sphere size on the ripples was studied by performing the experiments with spheres of diameter 640 nm and 1.76 μm spheres. The spheres did not have any influence on the ripple characteristics, and features with the same spacing and amplitude as before were obtained. In order to study the effect of angle of incidence on the ripple formation, the laser beam was illuminated both at 0^o and 45^o angle of incidence. Again, the angle of incidence was found to have negligible effect on the ripples and the features with the same spacing and amplitude were obtained.

In previous works, the ripple orientation was always perpendicular to the electric field direction. However in this work, the ripples were oriented perpendicular to the electric field while using an s-polarized beam and parallel to the electric field in case of a p-polarized beam. This means that the laser polarization did not influence the ripple formation and the ripples were always oriented in the same direction irrespective whether the polarization is horizontal or vertical.

The effect of laser fluence on the ripple formation was also studied. At very low laser fluences, around 10 mJ/cm^2, well defined ripples were observed. However, as the laser fluence is increased to 3 J/cm^2, hexagonally arranged periodic array of 350 nm bowl-like features were observed. In both cases, non-linear absorption of the enhanced optical field between the spheres and glass sample is believed to be the primary reason for the creation of nano-features on glass.

4.6 REFERENCES

1. Geiger, G., "Glass in Electronic Packaging Applications", *American Ceramic Society Bulletin,* **69**, 1131-&, (1990).
2. Illyefalvi-Vitez, Z., "Laser processing for microelectronics packaging applications", *Microelectronics Reliability,* **41**, 563-570, (2001).
3. Stuart, B. C., Feit, M. D., Rubenchik, A. M., Shore, B. W., and Perry, M. D., "Laser-Induced Damage in Dielectrics with Nanosecond to Subpicosecond Pulses", *Physical Review Letters,* **74**, 2248-2251, (1995).
4. Campbell, E. E. B., Ashkenasi, D., and Rosenfeld, A., "Ultra-short-pulse laser irradiation and ablation of dielectrics", *Lasers in Materials Science,* **301**, 123-144, (1999).
5. Mao, X. L., Mao, S. S., and Russo, R. E., "Imaging femtosecond laser-induced electronic excitation in glass", *Applied Physics Letters,* **82**, 697-699, (2003).
6. Davis, K. M., Miura, K., Sugimoto, N., and Hirao, K., "Writing waveguides in glass with a femtosecond laser", *Optics Letters,* **21**, 1729-1731, (1996).
7. Wang, J., Niino, H., and Yabe, A., "One-step microfabrication of fused silica by laser ablation of an organic solution", **68**, 111-113, (1999).
8. Zhou, G. S., Fauchet, P. M., and Siegman, A. E., "Growth of Spontaneous Periodic Surface-Structures on Solids During Laser Illumination", *Physical Review B,* **26**, 5366-5381, (1982).
9. Sipe, J. E., Young, J. F., Preston, J. S., and Vandriel, H. M., "Laser-Induced Periodic Surface-Structure .1. Theory", *Physical Review B,* **27**, 1141-1154, (1983).
10. Leamy, H. J., Rozgonyi, G. A., Sheng, T. T., and Celler, G. K., "Periodic Regrowth Phenomena Produced by Laser Annealing of Ion-Implanted Silicon", *Applied Physics Letters,* **32**, 535-537, (1978).
11. Tsukada, N., Sugata, S., Saitoh, H., and Mita, Y., "Surface Ripples in Laser-Photochemical Wet Etching of Gallium-Arsenide", *Applied Physics Letters,* **43**, 189-191, (1983).
12. Tsukada, N., Sugata, S., and Mita, Y., "New Experimental-Evidence of Surface Ripples on Gallium-Arsenide in Laser Annealing", *Applied Physics Letters,* **42**, 424-426, (1983).
13. Brueck, S. R. J., and Ehrlich, D. J., "Stimulated Surface-Plasma-Wave Scattering and Growth of a Periodic Structure in Laser-Photodeposited Metal-Films", *Physical Review Letters,* **48**, 1678-1681, (1982).

14. Osgood, R. M., and Ehrlich, D. J., "Optically Induced Microstructures in Laser-Photodeposited Metal-Films", *Optics Letters,* **7**, 385-387, (1982).

15. Jain, A. K., Kulkarni, V. N., Sood, D. K., and Uppal, J. S., "Periodic Surface Ripples in Laser-Treated Aluminum and Their Use to Determine Absorbed Power", *Journal of Applied Physics,* **52**, 4882-4884, (1981).

16. Maracas, G. N., Harris, G. L., Lee, C. A., and Mcfarlane, R. A., "Origin of Periodic Surface-Structure of Laser-Annealed Semiconductors", *Applied Physics Letters,* **33**, 453-455, (1978).

17. Young, J. F., Sipe, J. E., and Vandriel, H. M., "Regimes of Laser-Induced Periodic Surface-Structure on Germanium - Radiation Remnants and Surface-Plasmons", *Optics Letters,* **8**, 431-433, (1983).

18. Vanvechten, J. A., "Experimental Tests for Boson Condensation and Superconductivity in Semiconductors During Pulsed-Beam Annealing", *Solid State Communications,* **39**, 1285-1291, (1981).

19. Soileau, M. J., "Ripple Structures Associated with Ordered Surface-Defects in Dielectrics", *Ieee Journal of Quantum Electronics,* **20**, 464-467, (1984).

20. Temple, P. A., and Soileau, M. J., "Polarization Charge Model for Laser-Induced Ripple Patterns in Dielectric Materials", *Ieee Journal of Quantum Electronics,* **17**, 2067-2072, (1981).

21. Cline, H. E., and Anthony, T. R., "Non-Equilibrium Morphology of Liquid Inclusions Migrating in Solids", *Journal of Applied Physics,* **48**, 5096-5104, (1977).

22. Anthony, T. R., and Cline, H. E., "Surface Rippling Induced by Surface-Tension Gradients During Laser Surface Melting and Alloying", *Journal of Applied Physics,* **48**, 3888-3894, (1977).

23. Emelyanov, V. I., Konov, V. I., Tokarev, V. N., and Seminogov, V. N., "Formation of Periodic Surface Ripples under the Action of Pulsed Carbon-Dioxide Laser-Radiation on Fused-Silica", *Journal of the Optical Society of America B-Optical Physics,* **6**, 104-114, (1989).

24. Wilson, R. J., and Houle, F. A., "Composition, Structure, and Electric-Field Variations in Photodeposition", *Physical Review Letters,* **55**, 2184-2187, (1985).

25. Ehrlich, D. J., and Brueck, S. R. J., "Laser Photochemical Fabrication of Phase-Controlled 160-Nm Period Gratings by Stimulated 2nd-Order Surface Plasma-Wave Scattering", *Applied Physics Letters,* **47**, 216-218, (1985).

26. Mosbacher, M., Chaoui, N., Siegel, J., Dobler, V., Solis, J., Boneberg, J., Afonso, C. N., and Leiderer, P., "A comparison of ns and ps steam laser cleaning of Si surfaces", *Applied Physics a-Materials Science & Processing,* **69**, S331-S334, (1999).

27. Young, J. F., Sipe, J. E., Preston, J. S., and Vandriel, H. M., "Laser-Induced Periodic Surface Damage and Radiation Remnants", *Applied Physics Letters,* **41**, 261-264, (1982).

28. Dickinson, J. T., Shin, J. J., and Langford, S. C., "The role of defects in laser induced positive ion emission from ionic crystals", *Applied Surface Science,* **96-8**, 316-320, (1996).

29. Dickinson, J. T., Shin, J. J., and Langford, S. C., "Laser-induced emission of neutral atoms and molecules from electron-irradiated NaNO3", *Applied Surface Science,* **96-8**, 326-331, (1996).

30. Ashkenasi, D., Varel, H., Rosenfeld, A., Noack, F., and Campbell, E. E. B., "Pulse-width influence on the laser-induced structuring of CaF2 (111)", *Applied Physics a-Materials Science & Processing,* **63**, 103-107, (1996).

31. Varel, H., Ashkenasi, D., Rosenfeld, A., Herrmann, R., Noack, F., and Campbell, E. E. B., "Laser-induced damage in SiO_2 and CaF2 with picosecond and femtosecond laser pulses", *Applied Physics a-Materials Science & Processing,* **62**, 293-294, (1996).

32. Soileau, M. J., Vanstryland, E. W., and Williams, W. E., "Laser-Light Induced Bulk Damage to Optics", *Proceedings of the Society of Photo-Optical Instrumentation Engineers,* **541**, 110-122, (1985).

33. Soileau, M. J., Williams, W. E., Mansour, N., and Vanstryland, E. W., "Laser-Induced Damage and the Role of Self-Focusing", *Optical Engineering,* **28**, 1133-1144, (1989).

34. Bloembergen, N., "Light Waves Interact - a Citation-Classic Commentary on Interactions between Light Waves in a Nonlinear Dielectric by Armstrong,J.A., Bloembergen,N., Ducuing,J. And Pershan,P.S." *Current Contents/Engineering Technology & Applied Sciences,* 10-10, (1991).

35. Costache, F., Henyk, M., and Reif, J., "Modification of dielectric surfaces with ultra-short laser pulses", *Applied Surface Science,* **186**, 352-357, (2002).

36. Reif, J., Costache, F., Henyk, M., and Pandelov, S. V., "Ripples revisited: non-classical morphology at the bottom of femtosecond laser ablation craters in transparent dielectrics", *Applied Surface Science,* **197**, 891-895, (2002).

37. Costache, F., Henyk, M., and Reif, J., "Surface patterning on insulators upon femtosecond laser ablation", *Applied Surface Science,* **208**, 486-491, (2003).

38. Leiderer, P., Mosbacher, M., Boneberg, J., Bartels, C., Lang, F., Afonso, C., and Baeuerle, D., "Investigation of particle removal from silicon surfaces by means of dry and steam laser cleaning", *Ultra Clean Processing of Silicon Surfaces V,* **92**, 133-134, (2003).

39. Munzer, H. J., Mosbacher, M., Bertsch, M., Zimmermann, J., Leiderer, P., and Boneberg, J., "Local held enhancement effects for nanostructuring of surfaces", *Journal of Microscopy-Oxford,* **202**, 129-135, (2001).

40. Mosbacher, M., Munzer, H. J., Zimmermann, J., Solis, J., Boneberg, J., and Leiderer, P., "Optical field enhancement effects in laser-assisted particle removal", *Applied Physics a-Materials Science & Processing,* **72**, 41-44, (2001).

41. Fourrier, T., Schrems, G., Muhlberger, T., Heitz, J., Arnold, N., Bauerle, D., Mosbacher, M., Boneberg, J., and Leiderer, P., "Laser cleaning of polymer surfaces", *Applied Physics a-Materials Science & Processing,* **72**, 1-6, (2001).

42. Crisp, M. D., Boling, N. L., and Dube, G., "Importance of Fresnel reflections in laser surface damage of transparent dielectrics", *Applied Physics Letters,* **21**, 364-366, (1972).

Chapter 5: Nanoscale Processing of Silicon with Surface Plasmons

5.1 ABSTRACT

In this chapter, I report on the nano-scale surface modification of silicon using surface plasmons. The localized optical excitation is achieved by shining a 532 nm pulsed Nd:YAG laser beam on 40 nm gold spheres. Due to the excitation of coherent resonant electron plasma oscillations, there is a strong local enhancement of the electromagnetic field around the spheres. As a result of this enhancement, surface modification occurs by the melting and subsequent resolidification of silicon. Since this excitation is confined to a very small area, nanofeatures ranging from 30-40 nm in diameter are realized. These nanofeatures which are smaller than the laser wavelength ($\lambda/15$) are realized because the gold spheres interact strongly with visible light when resonantly excited at their surface plasmon frequency. The study is conducted on Silicon, polyimide and PMMA substrates. Nanofeatures were observed on silicon and polyimide, as the absorption of PMMA at this wavelength is very minimal.

5.2 INTRODUCTION

The miniaturization of conventional photonic devices is limited by diffraction effects due to the wave nature of light. In order to push the miniaturization of optical elements and devices new concepts are needed. In this context, research has recently intensified on noble metal nanoparticles [1]. Within such particles visible light can resonantly excite collective electron oscillations, also known as surface plasmons [2]. Surface plasmon resonances in metallic nanoparticles are of interest for a variety of applications due to the large electromagnetic field enhancement that occurs in the vicinity of the metal surface. Also the recent advances that allow metals to be structured and characterized on the nanometer scale have facilitated this .

Surface plasmons can be categorized into two types: localized plasmon resonances [3], in which incident light is absorbed or scattered by the oscillating electric dipoles within a metal nanoparticle; and surface plasmon polaritons [4], which propagate along metal surfaces in a waveguide-like fashion until released at some distance from their point of origin. The former are important for generating local field factors, which enhance linear and nonlinear optical effects near the metal surface. However, metal nanostructures often support both types of plasmons simultaneously; in fact, it can be difficult to decouple one from the other, resulting in a confusion of terms. It is the particle plasmon effect that is utilized in this study for the nanoscale modification of solids. Nevertheless, the plasmonic coupling of metal nanoparticles with light enhances a broad range of useful optical phenomena, such as resonant light scattering, surface plasmon resonance [5], and surface-enhanced Raman scattering [6], all of which have tremendous potential for ultra-sensitive chemical and biomolecular detection and analysis.

Many properties of particle plasmons can be qualitatively understood in the following semi-classical model [7] schematically shown in Figure 5.1. Since the diameter of the gold nanoparticles used is on the order of the penetration depth of electromagnetic waves in metals (at optical frequencies the penetration depth ~ 30 nm), the excitation light is able to penetrate the particle. The field inside the particle shifts the conduction electrons collectively with respect to the fixed positive charge of the lattice ions. The electrons build up a charge on the surface at one side of the particle. The attraction of this negative charge and the positive charge of the remaining lattice ions on the opposite side results in a restoring force. If the frequency of the excitation light field is in resonance with the eigen frequency of this collective oscillation, even a small exciting field leads to a strong oscillation. The magnitude of the oscillation depends only on the damping involved, which can be both radiative and nonradiative [8]. The resonance frequency is mainly determined by the strength of the restoring force. This force depends on the separation of the surface charges, i.e. the particle size, and the polarizability of the medium between and around the charges. The alternating surface charges effectively form an oscillating dipole, resulting in a resonantly enhanced non-propagating electromagnetic near-field close to the particle surface.

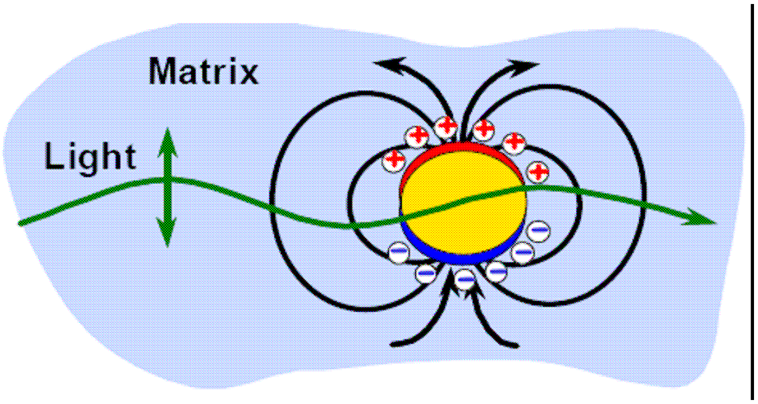

Figure 5.1: Schematic view of the excitation of a particle plasmon oscillation in a metal nanoparticle by an external light field

Figure 5.2 shows the flow of electromagnetic energy around a single spherical metal nanoparticle at two different excitation frequencies. The sketches show Poynting vector calculations for the absorption of electromagnetic energy. When the frequency of the light is far from the intrinsic plasmon resonance frequency of the metal nanoparticle the energy flow is only slightly perturbed. At the plasmon resonance frequency, the strong polarization of the particle effectively draws energy into the particle. The resonance in the polarizability leads to an enhanced electromagnetic near field which is confined over distances $d < \lambda$ to the surface of the nanoparticle. For Au and Ag nanoparticles, the near-field enhancement is typically on the order of 10 and can only be detected in the near field of the particle or through the enhancement of secondary processes such as an increased nanoparticle luminescence [9-11].

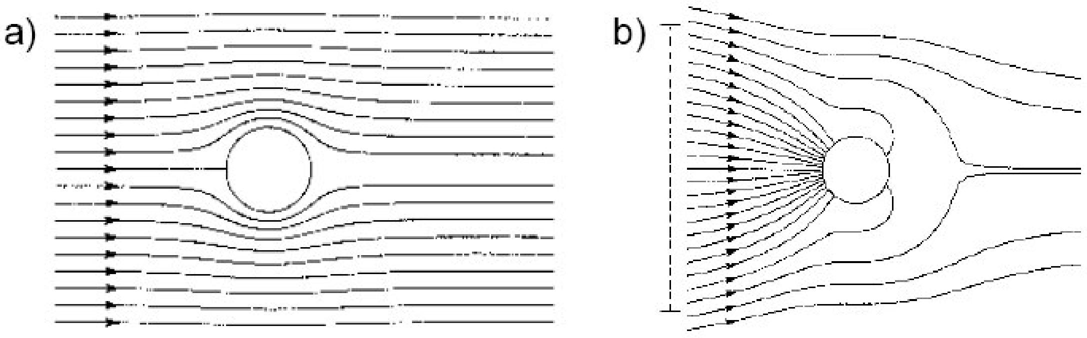

Figure 5.2: Energy flux (Poynting vector) around a metal nanoparticle under plane wave excitation at a) far from the plasmon resonance frequency, and b) at the plasmon resonance frequency

The field enhancement due to the plasmon oscillation has been used in a variety of applications, most notably for ultra-sensitive chemical and biomolecular detection and analysis. SPR has been used as an optical detection technology since its potential as biosensors was first demonstrated in 1983 [12, 13]. Compared with other sensors, plasmon based biosensors allow real-time measurement of biomolecular interactions without labeling and with simple optical system device. There are several examples in which SPR biosensors have been used to characterize the details of biomolecular interactions, and thus the SPR biosensors have emerged as one of the most powerful tools in biochemical and proteomics researches [14, 15]. This technique has been commercialized and is used extensively in biological research to study DNA hybridization [16], conformational changes of proteins [17], and reaction kinetics [18].

The strong electromagnetic field around the particles, which can be much higher than the exciting light field at the particle plasmon frequency, was used to enhance nonlinear optical effects such as surface enhanced Raman scattering [19-21]. The exact mechanism of this SERS enhancement remains unclear, but field enhancement seems to be one of the factors [22]. Other nonlinear applications such as generation of higher harmonics or white light are currently discussed. SPR concept have also been used as a waveguide to guide light in photonic devices [23]. Nanoscale gold dots that are patterned on a silicon-on-insulator wafer was successfully used to define the plasmon propagation path [24]. In order to improve the transmission V-shaped grooved have been used and the propagation distance performance has been extended to around 250 μm [25]. Several other schemes have also been developed for waveguiding: as laterally confined metal thin films [26], nanowires [27], Bragg mirrors [28], or photonic band gap structures [29].

More recently, a new field named ‘Plasmon nanolithography’ has emerged. Here the electric field enhancement by the plasmon has been utilized for nanostructuring. Sub-100 nm lines were patterned photolithographically using surface plasmon polaritonic interference in the optical near field excited by a wavelength of 436 nm [30]. Using 2-D hole arrays on an aluminum substrate, features as small as 90 nm have been realized [31]. Instead of using metallic masks to generate the plasmon resonance, silver nanospheres have been used and features as small as 50 nm were obtained [32]. However, since all the above mentioned works were developed as a parallel route to optical lithography, they focused only on patterning photoresists.

In this study, I use plasmons for directly patterning various substrates. This is achieved by illuminating gold nanospheres at their resonant frequency by using a 532 nm laser beam. The field enhancement as a result of this excitation is directly absorbed by the substrate and nanofeatures are realized. The features thus obtained are characterized using a scanning electron microscope. The effect of the substrate, sphere size, laser energy, polarization, and incidence angle has been studied experimentally and are presented in the following sections.

5.3 EXPERIMENTAL SETUP

The schematic of our experimental setup is shown in Figure 5.3a. A pulsed Nd:YAG laser of wavelength 532 nm and 355 nm, and pulse width 10 ns is used for the experiment. The output from the laser is passed through a half wave plate, which by rotating changes the polarization of the laser beam from horizontal to vertical and vice versa. The laser beam is then split into two by using a beam splitter - one part to be used for patterning and the other for measuring the laser energy. The sample is mounted on a 3-D stage and the laser beam is focused onto the sample by using a plano-convex lens.

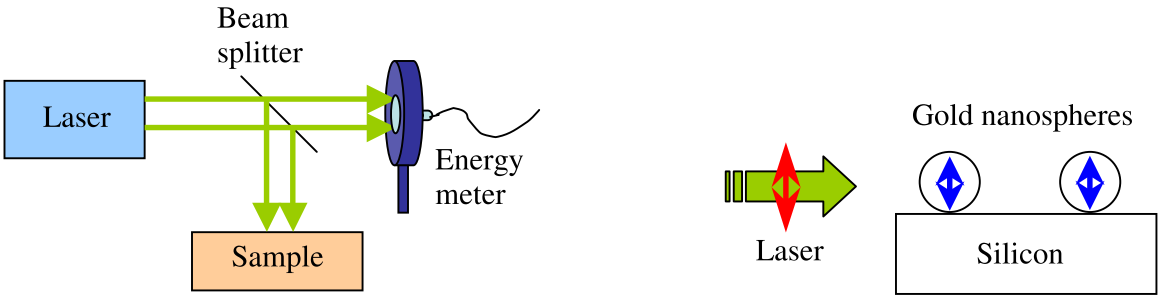

(a) **(b)**

Figure 5.3: Schematic of a) the experimental setup, and b) illumination of the gold spheres with the laser beam

As shown in Figure 5.3b, gold spheres are irradiated with a p-polarized laser beam ay a glancing angle i.e. parallel to the substrate. Since the diameter of the gold sphere is much smaller than the illuminating laser wavelength, this results in an oscillating dipole around the particle resulting in a strongly enhanced electrical field near the sphere. This resonantly excited field is absorbed by the substrate leading to formation of nanofeatures. The features thus obtained were characterized using a scanning electron microscope and are presented in the results and discussion section of the paper.

5.3.1 Sample preparation

The first sample used for patterning is a 500 μm thick *n*-type (100) polished silicon wafer with a surface roughness of a few nanometers (< 2 nm) and a 2-3 nm thick native oxide layer. Before processing the sample, care was taken to ensure that the sample is clean and free of any contaminants. For this reason, it is first cleaned in ethanol solution followed by rinsing in deionized water. After the sample is dried with nitrogen gas, a colloidal suspension of mono-dispersed gold spheres is applied on the silicon sample and let to dry. The gold solution is diluted in order to scatter the gold spheres deposited on the surface. A scanning electron microscope image of the scattered 40 nm gold spheres on silicon is presented in Figure 5.4.

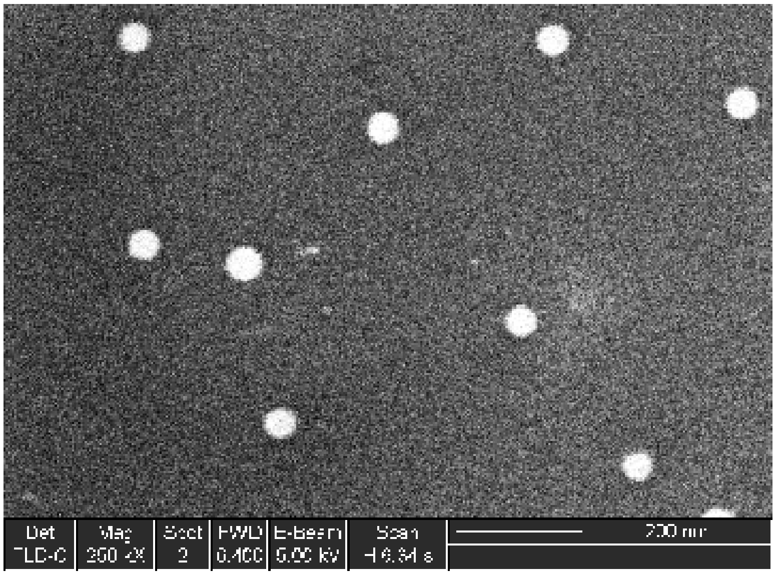

Figure 5.4: Scanning electron micrograph of the 40 nm gold spheres deposited on silicon.

Polyimide is the second material used in this study. This material is chosen because of its high absorption at both 355 and 532 nm. Also the relatively high glass transition temperature of polyimide (280^{o}C – depending on the measurement technique) is another desirable feature. Polyimide films of 125 µm thickness (Good fellow Inc.) are cleaned and scattered gold spheres were deposited as before.

In order to make sure the formation of nanofeatures is purely due to the optical excitation of plasmons and not the heating of gold spheres, Polymethyl-methacrylate (PMMA) is used as the third substrate. PMMA is chosen because of its poor absorption characteristic at this wavelength. First silicon sample is cleaned in ethanol and using a spin coater at 1200 rpm for 90 seconds PMMA is spin coated on the silicon substrate. This is followed by baking the sample in an oven at 120 F for 1 hour to improve the adhesion. As before, gold spheres are deposited by applying a drop of the gold solution and letting it to dry.

5.4 RESULTS AND DISCUSSION

As explained above, gold spheres are deposited on the substrate and irradiated with a laser beam. The experiment is performed on three different materials (silicon, polyimide, and PMMA) using gold spheres of different diameters (250 nm and 40 nm). The effect of laser polarization (s and p-polarization) at various incident angles (0^o and 90^o) is studied in detail in order to understand the role of each of these parameters. Then an optical microscope and a scanning electron microscope were used to characterize the features obtained and the resulting images are presented and explained below.

5.4.1 Effect of Substrate

40 nm gold spheres are deposited on silicon substrate and a p – polarized 532 nm laser beam is incident at a glancing angle on the substrate. Features comparable to the sphere diameter i.e. approximately 40 nm are created on the surface. A scanning electron microscope image of the features created with a laser fluence of 50 mJ/cm^2 is shown in Figure 5.5.

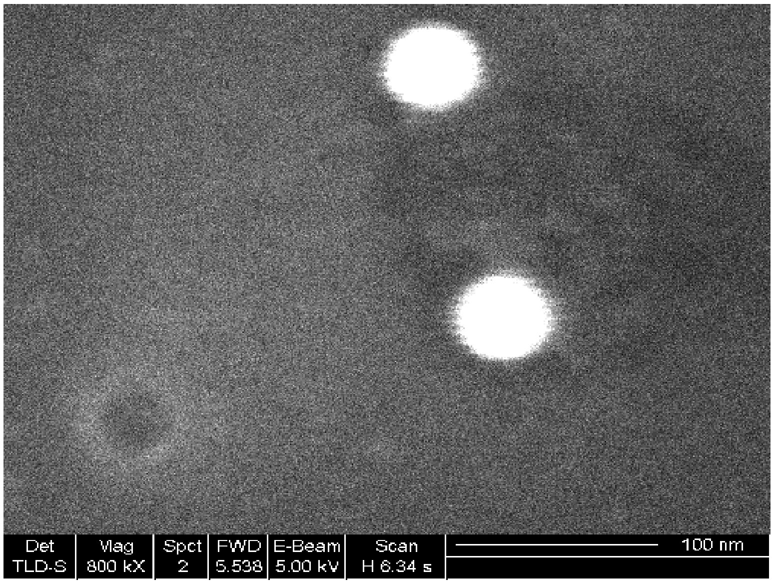

Figure 5.5: SEM micrograph of the features on silicon obtained by irradiating 40 nm gold spheres with a 532 nm laser at 50 mJ/cm^2 fluence.

The diameter of the gold spheres is much smaller than the applied wavelength, and hence when irradiated at their resonance frequency all conduction electrons are excited in phase in a collective dipole-like oscillation. The enhanced electromagnetic field resulting from this resonant illumination is confined over distances $d < \lambda$ to the surface of the nanoparticle. Hence the features formed are approximately the same size or smaller than the spheres used in the study. This is confirmed by Heltzel et al. using a finite-difference time-domain method (FDTD) equipped with the Drude model for gold (Appendix – 2).

When 40 nm gold spheres deposited on Polyimide is irradiated with a 532 nm laser beam, similar features are obtained. Figure 5.6 is a scanning electron microscope image of the features obtained with a laser fluence of 50 mJ/cm2. This fluence is much lower than the ablation threshold of polyimide at 532 nm, which is 200 mJ/cm2. This clearly shows that the features are created because of the field enhancement due to collective plasmon oscillations. Also, the features obtained are slightly larger due to the relatively low glass transition temperature of polyimide and the photo thermal nature of the ablation process.

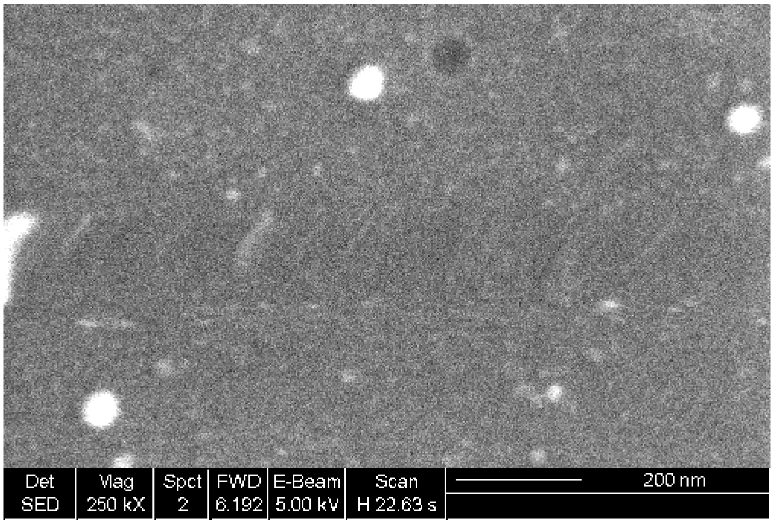

Figure 5.6: SEM micrograph of the features on polyimide obtained by irradiating 40 nm gold spheres with a 532 nm laser at 50 mJ/cm^2 fluence.

The feature formation could also be due to the heating of the gold spheres by the incident 532 nm laser radiation and the subsequent heat conduction to the substrate. In order to verify this hypothesis, the same experiment is performed on PMMA. This material is chosen because of its low glass transition (90^{o}C) and melting temperatures (200^{o}C). When gold spheres are deposited on PMMA and irradiated with a 532 nm laser beam, no such features were observed. This confirms that the features formed on silicon and polyimide is not because of the heating of gold, but rather due to the electric field enhancement around the nanospheres.

5.4.2 Effect of Sphere Size

In order to study the effect of sphere diameter on the features formed, two sphere diameters – 40 nm and 250 nm were deposited on silicon and irradiated with a p – polarized 532 nm laser beam at a glancing angle. When 40 nm spheres are used, features approximately 40 nm in diameter are formed – Figure 5.5. In case of 250 nm gold spheres, approximately 100 nm features are created. A scanning electron microscope image of the features formed at a laser fluence of 50 mJ/cm^2 is shown in Figure 5.7.

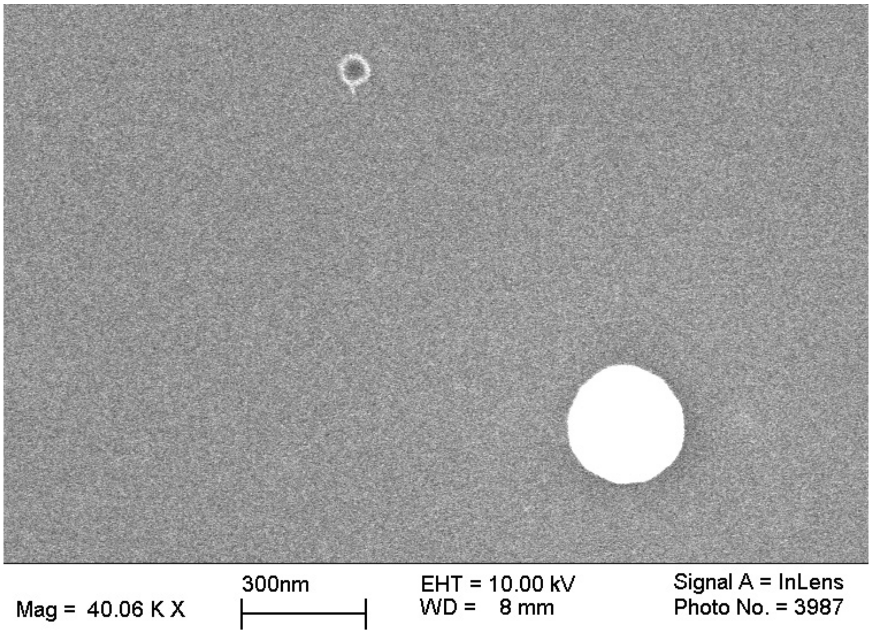

Figure 5.7: SEM micrograph of the features on silicon obtained by irradiating 250 nm gold spheres with a 532 nm laser at 50 mJ/cm^2 fluence.

5.4.3 Effect of Polarization

The study was conducted for both s and p – polarized laser beams. As before 40 nm gold spheres were deposited on silicon and a 532 nm laser beam is incident on the substrate at a glancing angle. A half wave plate was used to change the polarization from horizontal to vertical and vice versa. Nanofeatures were observed only for the p – polarized beam because for the s – polarized beam, the plasmon oscillation is not directed at the substrate, instead it is parallel to the substrate.

5.4.4 Effect of Laser Energy

The experiment is performed using 40 nm gold spheres irradiated by a single 532 nm laser pulse incident at a glancing angle at four fluences: 50, 100, 200 and 250 mJ/cm^2. The features thus created are characterized using an SEM, and the results are presented in Figure 5.8, and Figure 5.9. Increasing the laser energy from 50 mJ/cm^2 to 200 mJ/cm^2 doesn't seem to have any effect on the diameter of the features. The features obtained for all these cases are approximately 40 nm in diameter, indicating a strong dependence on the sphere size rather than the laser fluence. However from the scanning electron microscope images, it appears that the depth of the features increase with energy. An attempt was made to get the depth profile by using an atomic force microscope, but due to the extreme small geometry of the features, the feature depth couldn't be resolved. Increasing the laser fluence to 250 mJ/cm^2 resulted in the disintegration of the gold spheres, and no features were observed.

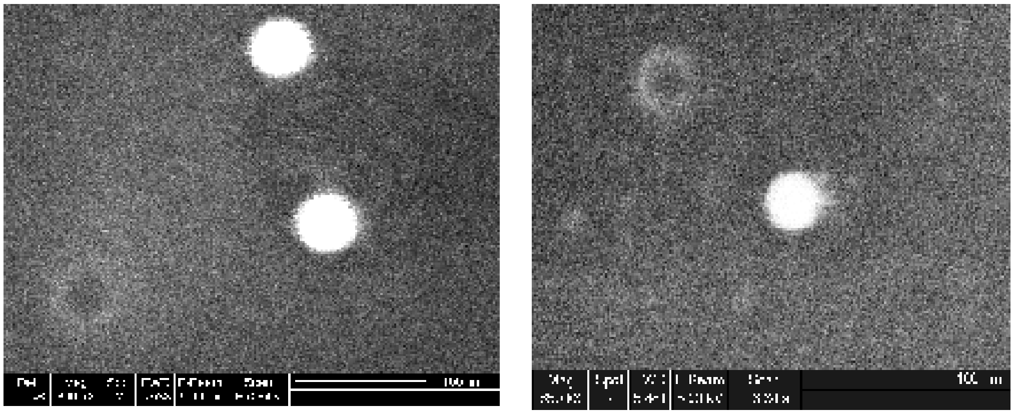

Figure 5.8: SEM micrograph of 40 nm gold spheres irradiated by 532 nm laser at a fluence of (a) 50 mJ/cm^2, and (b) 100 mJ/cm^2.

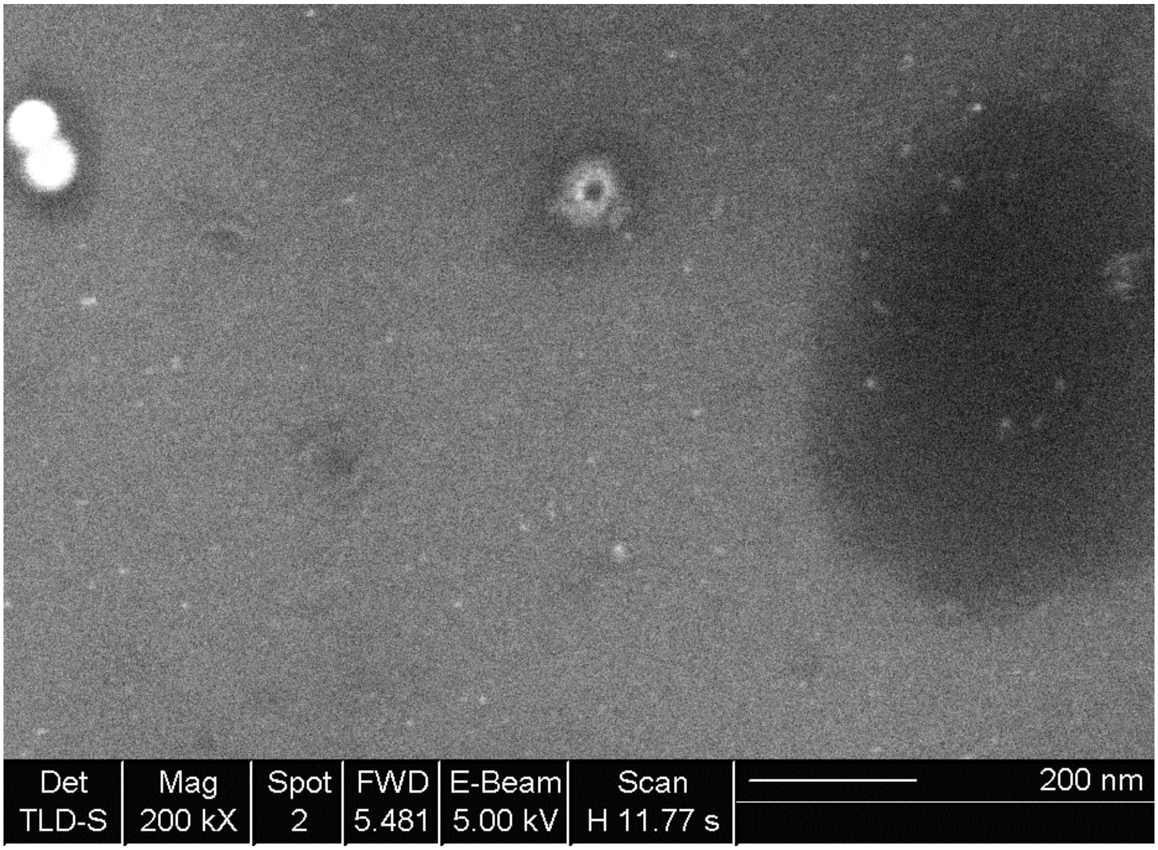

Figure 5.9: SEM micrograph of 40 nm gold spheres irradiated by 532 nm laser at a fluence of 200 mJ/cm^2.

5.4.5 Effect of Incident Angle

The effect of two angles of incidence – normal incidence (90^o) and glancing incidence (0^o), were studied. Nanofeatures were observed only for the p – polarized glancing incidence and not for the normal incidence (irrespective of the polarization). This is because only under glancing incidence and p - polarization, the plasmon oscillation is directed at the substrate. This is confirmed by a finite difference time domain model equipped with Drude model for gold.

5.5 CONCLUSIONS

Features as small as 40 nm (λ/15) have been realized on various substrates by overcoming the diffraction limit of light. This is achieved by irradiating gold nanospheres using a 532 nm Nd:YAG laser and inducing collective plasma oscillations inside the nanoparticle. The electrical field enhancement resulting form this oscillation is absorbed by the substrate and nanofeatures are created. The effect of substrate material, sphere diameter, laser energy, and laser polarization on the feature formation is studied in detail. The features are characterized by a scanning electron microscope.

Nanofeatures were successfully created on silicon and polyimide, but not on PMMA. This is because PMMA is highly transparent in this wavelength range and does not absorb the enhanced radiation. From the study it was concluded that the features are formed only because of the collective plasmon excitation and not due to the heating of gold nanospheres.

The diameter of the features formed does not depend on the incident laser intensity and remained the same for increasing energy density. However the depth of the features seems to increase with fluence, but could not be verified with an atomic force microscope due to the extremely small geometry of the features.

The sphere diameter has a huge influence on the feature size. For 40 nm spheres, approximately 40 nm features were created. Using 250 nm spheres resulted in features approximately 100 nm in diameter. This is because the enhanced field is confined to a very small area just underneath the spheres.

Nanofeatures were obtained only for a p – polarized laser beam incident on the spheres at a glancing angle. Only under these conditions, the collective plasma oscillation is normal to the substrate as confirmed by the FDTD model equipped with Drude model for gold (1). For an s – polarized beam, the field enhancement is directed parallel to the substrate, and as a result it is not absorbed by the substrate. For normal incidence of the laser beam nanofeatures were not observed for the above explained reason.

5.6 REFERENCES

1. Klar, T.A., Perner, M., Grosse, S., Plessen, G., Spirkl, W., and Feldmann, J., "Surface-plasmon resonances in single metallic particles", *Physical Review Letters* **80,** 4249-4252 (1998).
2. Raether, H., *Surface plasmons*, Springer, Berlin, 1988.
3. Hutter, E., and Fendler, H., "Exploitation of localized surface plasmon resonance", *Advanced Materials*, **16,** 1685-1706, (2004).
4. Sambles, J.R., Bradbery, G.W., and Yang, F., "Optical excitation of surface plasmons: an introduction", *Contemporary physics*, **32,** 173-183, (1991).
5. Murray, W.A., Astilean, S., Barnes, W.L., "Transition from localized surface plasmon resonance to extended surface plasmon-polariton as metallic nanoparticles merge to form a periodic hole array ", *Physical Review B*, **69,** 165407/1-7, (2004).
6. Grand, J., de la Chapelle, M.L., Bijeon, J.-L., Adam, P.-M., Vial, A., Royer, P., "Role of localized surface plasmons in surface-enhanced Raman scattering of shape-controlled metallic particles in regular arrays ", *Physical Review B*, **72,** 33407/1-4, (2005).
7. Sonnichsen, C., *Plasmons in metal nanostructures*, in *Department of Physics*. 2001, Ludwig-Maximilians-University of Munich: Munich.
8. Sönnichsen, C., Franzl, T.,Wilk, T., von Plessen, D., and Feldmann J., "Drastic reduction of plasmon damping in gold nanorods", *Physical Review Letters*, **88,** 077404/1-4, (2002).
9. Boyd, G.T., Yu, Z.H., and Shen, Y.R., "Photoinduced luminescence from the noble metals and its enhancement on roughened surfaces", *Physical Review B*, **33,** 7923-7935, (1986).
10. Mohamed, M.B., Volkov, V., Link, S., and El-Sayad, M.A., "The 'lightning' gold nanorods: fluorescence enhancement of over a million compared to the gold metal", *Chemical Physics Letters*, **317,** 517-523, (2000).
11. Wilcoxon, J.P., Martin, J.E., Parsapour, F., Wiedenman, B., and Kelley, D.F., "Photoluminescence from nanosize gold clusters", *Journal of Chemical Physics*, **108,** 9137-9143.
12. Liedberg, B., Nylander, C., Lundstrom, I., "Surface plasmon resonance for gas detection and biosensing", *Sensors and Actuators* **4,** 299-304, (1983).

13. Yuk, J.S., Jung, J.W., Jung, S.H., Hong, D., Han, J.A., Kim, Y.M., Ha, K.S., "Analysis of protein interactions on protein arrays by a wavelength interrogation-based surface plasmon resonance biosensor", *Proteomics*, **4,** 3468-3476, (2004).

14. Zhavnerko, G., Ha, K.S. Biosensor applications: surface engineering. In:. in *Encyclopedia of Nanoscience and Nanotechnology*. 2004: Marcel Dekker

15. Myszka, D.G., Rich, R.L., "Implementing surface plasmon resonance biosensors in drug discovery", *Pharmaceutical Science and Technology Today* **310-317**, (2000).

16. He, L., Musick, M.D., Nicewarner, S.R., Salinas, F.G., Benkovic, S.J., Natan, M.J., and Keating, C.D., "Colloidal Au-enhanced surface plasmon resonance for ultrasensitive detection of DNA hybridization", *Journal of the American Chemical Society*, **122,** 9071–9077, (2000).

17. Yu, C.Y., Chen, L.L., Luo, H.B., Chen, J., Cheng, F., Gui, C.S., Zhang, R.H., Shen, J.H., Chen, K.X., Jiang, H.L., and Shen, X., "Binding analyses between human PPAR {gamma}-LBD and ligands - surface plasmon resonance biosensor assay correlating with circular dichroic spectroscopy determination and molecular docking", *European Journal of Biochemistry*, **271,** 386–397, (2004).

18. Shannessy, D.J., Brighamburke, M., Soneson, K.K., Hensley, P., and Brooks, I. , "Determination of rate and equilibrium binding constants for macromolecular interactions using surface plasmon resonance - use of nonlinear least squares analysis methods", *Analytical Biochemistry*, **212,** 457–468, (1993).

19. Moskovits, M., "Surface-enhanced spectroscopy", *Review of Modern Physics*, **57,** 783, (1985).

20. Kneipp, K., Wang, Y., Kneipp, H., Itzkan, I., Dasari, R.R., and Feld, M. S., "Population pumping of excited vibrational states by spontaneous surface-enhanced Raman scattering", *Physical Review Letters*, **76,** 2444, (1996).

21. Nie, S.a.E., S.R., "Probing single molecules and single nanoparticles by surface enhanced Raman scattering", *Science*, **275,** 1102, (1997).

22. Shalaev, V., *Nonlinear Optics of Random Media: Fractal Composites and Metal-Dielectric Films*, Springer, Berlin, 2000.

23. Krenn, J., Wolf, R., Leitner, A., and Aussenegg, F., "Near-field optical imaging the surface plasmon fields of lithographically designed nanostructures", *Optics Communications*, **137,** 46, (1997).

24. Maier, S.A., Barclay,P.E., Johnson, T.J., Friedman, M.D., and Painter, O.A.P.L., 071103 (2005). "Experimental demonstration of fiber-accessible metal nanoparticle plasmon waveguides for planar energy guiding and sensing", *Applied Physics Letters*, **86**, (2005).

25. Bozhevolnyi, S.I., Volkov, V.S., Devaux, E., Ebbesen, T.W., "Channel plasmon-polariton guiding by subwavelength metal grooves", *Physical Review Letters*, **95,** 046802/1-4, (2005).

26. Weeber, J.C., Krenn, J.R., Dereux, A., Lamprecht, B., Lacroute, Y., Goudonnet, J.P., "Near-field observation of surface plasmon polariton propagation on thin metal stripes", *Physical Review B*, **64,** 045411/1-9, (2001).

27. Krenn, J.R., Lamprecht, B., Ditlbacher, H., Schider, G., Salerno, M., Leitner, A., Aussenegg, F.R., "Non-diffraction-limited light transport by gold nanowires", *Europhysics Letters*, **60,** 663-669, (2002).

28. Ditlbacher, H., Krenn, J.R., Schider, G., Leitner, A., Aussenegg, F.R., "Two-dimensional optics with surface plasmon polaritons", *Applied Physics Letters*, **81,** 1762-1764, (2002).

29. Bozhevolnyi, S.I., Volkov, V.S., Leosson, K., Boltasseva, A., "Bend loss in surface plasmon polariton band-gap structures", *Applied Physics Letters*, **79,** 1076-1078, (2001).

30. Luoa, X., and Ishihara, T., "Surface plasmon resonant interference nanolithography technique", *Applied Physics Letters*, **84,** 4780-4782, (2004).

31. Srituravanich, W., Fang, N., Sun, C., Luo, Q., and Zhang, X., "Plasmonic Nanolithography", *Nano Letters*, **4,** 1085-1088, (2004).

32. Kik, P.G., Maier, S.A., Atwater, H.A. Plasmon printing - a new approach to near-field lithography. in *Nanopatterning - From Ultralarge-Scale Integration to Biotechnology. Symposium (Materials Research Society Symposium Proceedings)*. 2002.

Chapter 6: Summary

This dissertation is aimed at exploring the use of lasers for micro and nano scale processing of advanced materials like silicon and glass. The objective of the dissertation is two fold: a) use lasers for locally micro bonding glass and silicon wafers, and b) use lasers for nanopatterning glass and silicon. In the first part, glass and silicon wafers are bonded locally in microscale by laser transmission joining technique, and in the second part nanoscale processing is accomplished by circumventing the diffraction limit of light by the use of nanospheres.

In the first part of the dissertation (Chapter 2), silicon and glass wafers were bonded directly using a localized laser heating technique. A 1064 nm pulsed Nd:YAG laser of 12 ns pulse width was used for the bonding process. As glass is transparent to this wavelength, the laser beam passes through the glass wafer and is absorbed by silicon. As a result, silicon is melted, and upon resolidification, bonding is realized between the two wafers. The transient melting and resolidification of silicon were studied by probing with a 633 nm continuous wave He-Ne laser. The bonded areas were characterized using a scanning electron microscope and a chemical analysis was done to understand the bonding mechanism. Numerical simulation was also carried out using finite element method to predict the local temperature change of both materials during bonding, and there is good agreement between the experimental and numerical results.

In the second part of the dissertation (Chapters 3-5), nanopatterns were created on glass and silicon substrates by circumventing the diffraction limit of light. The nanofeatures were created by irradiating silica and gold nanospheres deposited on a substrate. In case of silica spheres, features approximately half the diameter of the sphere were obtained by utilizing the optical field enhancement around the spheres. In case of gold spheres, features as small as 40 nm were realized by the excitation of coherent resonant electron plasma oscillations. The effect of sphere size, laser wavelength, polarization, incident angle, and energy were studied experimentally and compared with the numerical results where applicable.

In Chapter 3, an experimental investigation on the sub micron features created on silicon by the irradiation of 1.76 μm silica microspheres with a 532 nm pulsed laser is presented. These features thus obtained were approximately half the diameter of the spheres used. The diameter of the features did not change upon switching from 532 to 355 nm, but the feature depth increased due to higher field enhancement and higher absorption at 355 nm. The experimental results are compared with the numerical results from a multidimensional, heat transfer model built by Heltzel et al. to simulate the heat transfer through silicon. The experimental results correlate well with the predicted results. Also the threshold energy required to damage the substrate with the presence of nanospheres matches the level of enhancement predicted by the Mie theory calculations.

In Chapter 4, nano-scale surface modification of borosilicate glass, when irradiated by a 1064 nm pulsed Nd:YAG laser in the presence of silica nanospheres is reported. At very low energy densities, sub-micron ripples are created on the glass surface. The ripples thus obtained do not satisfy Rayleigh's diffraction condition in that a) the ripple spacing is different from the value predicted by the classical model, b) the spacing is independent of the incident angle, and c) the orientation is not always perpendicular to the laser polarization. Also, the ripple characteristics are not dependent on the diameter of the spheres used and the ripples have almost the same periodicity irrespective of the experimental parameters. However, at higher energy densities hexagonally arranged nanofeatures 350 nm in diameter are formed on the substrate instead of the ripples. Nonlinear absorption of the enhanced optical field between the spheres and glass sample is believed to be the primary reason for the creation of nano-features on the glass substrate.

In Chapter 5, surface plasmons are employed to circumvent the diffraction limit of light for nano-scale surface modification. The localized optical excitation is achieved by shining a p-polarized, 532 nm laser beam on 40 nm gold spheres at a glancing angle. Since this excitation is confined to a very small area, nanofeatures ranging from 30-40 nm in diameter ($\lambda/15$) were realized. The study was conducted on silicon, polyimide and PMMA substrates. Nanofeatures were observed only on silicon and polyimide, and not on PMMA because of its high transparency and poor absorption at this wavelength. Also it was concluded that the feature formation is only because of the collective plasmon excitation and not due to the heating of gold nanospheres and the subsequent heat conduction to the substrate.

Appendix – 1

The enhancement of incident intensity can be described from the starting point of Mie's theory of scattering. Born and Wolf presents the rigorous solution to Maxwell's equations describing the scattered electromagnetic field components [1].

The electric field vectors are:

$$
\begin{aligned}
E_r^{(s)} &= \frac{1}{k^2}\frac{\cos\phi}{r^2}\sum_{l=1}^{\infty} l(l+1)eB_l\zeta_l^{(1)}(kr)P_l^{(1)}(\cos\theta), \\
E_\theta^{(s)} &= -\frac{1}{k}\frac{\cos\phi}{r}\sum_{l=1}^{\infty}[eB_l\zeta_l^{(1)}{}'(kr)P_l^{(1)}{}'(\cos\theta)\sin\theta \\
&- i\cdot mB_l\zeta_l^{(1)}(kr)\frac{P_l^{(1)}(\cos\theta)}{\sin\theta}] \\
E_\phi^{(s)} &= -\frac{1}{k}\frac{\sin\phi}{r}\sum_{l=1}^{\infty}[eB_l\zeta_l^{(1)}{}'(kr)\frac{P_l^{(1)}(\cos\theta)}{\sin\theta} \\
&- i\cdot mB_l\zeta_l^{(1)}(kr)P_l^{(1)}{}'(\cos\theta)\sin\theta]
\end{aligned}
\tag{1}
$$

The magnetic field vectors are:

$$
\begin{aligned}
H_r^{(s)} &= \frac{1}{k^2}\frac{\sin\phi}{r^2}\sum_{l=1}^{\infty} l(l+1)mB_l\zeta_l^{(1)}(kr)P_l^{(1)}(\cos\theta) \\
H_\theta^{(s)} &= \frac{i}{k}\frac{\sin\phi}{r}\sum_{l=1}^{\infty}[eB_l\zeta_l^{(1)}{}'(kr)P_l^{(1)}{}'(\cos\theta)\sin\theta \\
&- i\cdot mB_l\zeta_l^{(1)}(kr)\frac{P_l^{(1)}(\cos\theta)}{\sin\theta}] \\
H_\phi^{(s)} &= -\frac{i}{k}\frac{\cos\phi}{r}\sum_{l=1}^{\infty}[eB_l\zeta_l^{(1)}{}'(kr)P_l^{(1)}{}'(\cos\theta)\sin\theta \\
&- i\cdot mB_l\zeta_l^{(1)}(kr)\frac{P_l^{(1)}(\cos\theta)}{\sin\theta}]
\end{aligned}
\tag{2}
$$

The coefficients eB_l and mB_l characterize the wave scattered by the sphere and are given by

$$eB_l = i^{l+1}\frac{2l+1}{l(l+1)}\frac{n\psi_l'(q)\psi_l(nq)-\psi_l(q)\psi_l'(nq)}{n\zeta_l^{(1)}{}'(q)\psi_l(nq)-\zeta_l^{(1)}(q)\psi_l'(nq)} \tag{3}$$

$$mB_l = i^{l+1}\frac{2l+1}{l(l+1)}\frac{n\psi_l(q)\psi_l'(nq)-\psi_l'(q)\psi_l(nq)}{n\zeta_l^{(1)}(q)\psi_l'(nq)-\zeta_l^{(1)}{}'(q)\psi_l(nq)} \tag{4}$$

The terms containing $P_l^{(1)}(\cos\theta)$ and its derivatives are forms of the associated Legendre functions [2, 3] defined as

$$P_l^{(m)}(\cos\theta) = (\sin\theta)^m \frac{d^m P_l(\cos\theta)}{d(\cos\theta)^m} \tag{5}$$

with the (non-associated) Legendre polynomial given by

$$P_l(\cos\theta) = \sum_{m=0}^{l/2}(-1)^m \frac{(2l-2m)!}{2^l m!(l-m)!(l-2m)!}(\cos\theta)^{l-2m} \tag{6}$$

$\zeta_l^{(1)}$ is proportional to the spherical Hankel function, which is a complex combination of first and second-order Bessel functions.

$$\zeta_l^{(1)}(\rho) = \psi_l(\rho) - i\cdot\chi(\rho) = \sqrt{\frac{\pi\rho}{2}}\cdot H_{l+\frac{1}{2}}^{(1)}(\rho) \tag{7}$$

The scattered electromagnetic field components are added to the incident field components (plane wave of the laser) to give the solution to Maxwell's equations both inside and outside the sphere. The parameter, n, is the complex refractive index of the sphere. The parameter, k, in equations (1) and (2) is equal to 2π divided by the wavelength of the incident laser. The parameter, q, is equal to k times the radius of the sphere.

There is some difficulty associated with the exact calculation of the field components, specifically the Bessel functions, Legendre functions, and their derivatives. Much of this difficulty can be circumvented by substituting asymptotic approximations for these terms that acceptably describe the field at a large distance from the particle. The critical coefficients eB_l and mB_l can be approximated for relatively large or highly conductive particles. In addition to individual term approximations, the overall intensity of the field is often approximated by squaring the amplitude of the electric vector. Under the conditions of the experiments presented, none of these simplifications can be acceptably included. Most importantly, the far field approximation cannot be utilized, as it is specifically the near field enhancement that is assumed responsible for the substrate damage.

Because of the limitations, all terms in Mie's theory, eqs. (1) and (2) were calculated exactly up to the critical value of $l_{cut\text{-}off}$, after which the terms in the infinite sum were equal to zero. This was done through the use of recurrence relations for the Bessel functions and Legendre functions provided by [2, 3]. The derivatives of these functions were determined numerically, with 45,000 values calculated in the range of θ = 0 to 45°, with the origin taken at the center of the sphere. The summation cut-off value of l, was chosen to be

$$l_{cut-off} = \frac{2\pi \cdot a \cdot n}{\lambda} + 4 \qquad \textbf{(8)}$$

where a is the sphere radius, n is the real refractive index of the sphere, and λ is the incident wavelength of the laser. An investigation was carried out to determine the effectiveness of the $l_{cut\text{-}off}$ value. The magnitude of the real and imaginary coefficients, eB_l and mB_l fell to zero through four decimal places by the final term included in the summation for all theoretical cases. Therefore $l_{cut\text{-}off}$ was chosen large enough to contain every term of value in the infinite series.

The intensity of the radiation incident on the plane of the substrate is quantified using the Poynting vector of the EM field. The spherical components of the time-averaged Poynting vector are:

$$\begin{aligned} S_r &= I_0 \cdot \mathrm{Re}\left[E_\theta H_\phi^* - E_\phi H_\theta^*\right] \\ S_\theta &= I_0 \cdot \mathrm{Re}\left[E_\phi H_r^* - E_r H_\phi^*\right] \\ S_\phi &= I_0 \cdot \mathrm{Re}\left[E_r H_\theta^* - E_\theta H_r^*\right] \end{aligned} \qquad \textbf{(9)}$$

I_0 is the intensity of the incident laser, and the asterisk superscript indicates the complex conjugate of the magnetic field components. The z-direction is taken longitudinal to the incident laser and normal to the substrate lying beneath the particle. The z-component of the Poynting vector is therefore a description of the energy incident upon the substrate surface due to the laser and the presence of the nanosphere. The coordinate convention used dictates the z-component equal to

$$S_z = \cos\theta \cdot S_r - \sin\theta \cdot S_\theta \qquad \textbf{(10)}$$

S_z has been calculated for certain cases available for experimentation.

Numerical modeling

Calculation of the laser intensity enhancement provides a boundary condition to employ in a model of the heat transfer within the substrate. The goal of the simulation is to obtain a maximum temperature distribution in the silicon, which indicates the size and shape of the melt zone. This data is then compared with experimental observations characterized using an SEM.

The ~ 6 nanosecond duration of the laser pulse allows the use of Fourier conduction within the substrate. The enthalpy method was used explicitly to account for the moving phase boundary within the material (Stefan problem) [4-6] The heat equation as a function of the enthalpy in the silicon is

$$\rho \frac{\partial H}{\partial t} = \frac{\partial}{\partial x}\left(k \frac{\partial T}{\partial x} \right) + \frac{\partial}{\partial y}\left(k \frac{\partial T}{\partial y} \right) + \dot{q} \tag{11}$$

with the generation term $\dot{q}$ (W/m^3) equal to

$$\dot{q} = (1 - r) \cdot q_{inc}(x_{\text{int}}, t) \cdot a \cdot e^{(-a \cdot z)} \tag{12}$$

where r is the reflectivity of silicon dependent on the wavelength of the incident light and phase of the silicon, and a is the absorption coefficient, given by:

$$r = \frac{(n-1)^2 + k_x^2}{(n+1)^2 + k_x^2} \tag{13}$$

$$a = \frac{4 \cdot \pi \cdot k_x}{\lambda} \tag{14}$$

q_{inc} is the enhanced value of laser energy taken at x_{int}, the surface intercept node between the node in the solid and the center of the sphere. It follows a Gaussian shape through time given by

$$q_{inc}(x_{\text{int}}, t) = A \cdot \exp\left[-(B - t)^2 / C \right] \cdot I(x_{\text{int}}) \tag{15}$$

The constants B and C are fit to the laser waveform, while A ensures the total energy incident corresponds to the proper fluence, and $I(x_{\text{int}})$ refers to the intensity distribution.

New values of H are calculated explicitly every time step, relying only on the surrounding temperatures from the previous iteration. This precludes the need to invert matrices or employ other convergence algorithms, but requires the following expression obeyed to prevent divergence of the solution.

$$\frac{\Delta t}{\Delta x^2} \leq \frac{\rho \cdot c}{2 \cdot k} \tag{16}$$

This expression limits the numerical time and space steps in terms of the specific heat, density, and thermal conductivity of the material. Using the extreme values of all three variables in the anticipated temperature range, the left-hand side of [7]must be less than approximately 6000. Time steps of 75 fs and space steps of 19.5 nm were used to obtain the following results, and were proven adequate by grid-independence investigations.

At the surface of the substrate, an energy conserving boundary condition is used to account for energy loss due to radiation, which was found to be significant at the high temperatures of the liquid state.

$$(1-r)\cdot q_{inc} - \varepsilon \cdot \sigma \cdot T^4 = k\frac{\Delta t}{\Delta y} + \rho \cdot c \cdot \Delta y \frac{\Delta T}{\Delta t} \tag{17}$$

The emissivity, ε, of the liquid silicon is determined from the following relation:

$$\varepsilon(\lambda, T) = \frac{4n}{n^2 + k^2 + 2n + 1} \tag{18}$$

where the refractive indices n and k are obtained from [7, 8]

The new value of enthalpy calculated determines the temperature at the node based on the following relations:

$$\begin{aligned}
&T_{x,y}^{t+1} = H_{x,y}^{t+1} / c_l && H^{t+1} < (c \cdot T_m) \\
&T_{x,y}^{t+1} = T_m && (c \cdot T_m) < H^{t+1} < (c \cdot T_m + L) \\
&T_{x,y}^{t+1} = \left(H_{x,y}^{t+1} - (c - c_l) \cdot T_m - L_m\right) / c_l && H^{t+1} \geq (c \cdot T_m + L)
\end{aligned} \tag{19}$$

The silicon is therefore separated into three regimes: solid, liquid, and a transition zone. The boundaries of these regions are tracked through time using the preceding method.

References

1. Born, M., and Wolf, E., *Principles of Optics*, 7th edition, Cambridge University, Cambridge, England, 1999.
2. Abramowitz, M., and Stegun, I., *Handbook of Mathematical Functions*, Dover, New York, 1965.
3. Lowan, A., *Tables of Associated Legendre Functions*, Columbia University Press, New York, 1945.
4. Xu, X., Grigoropoulos, C.P., Russo, R.E., "Heat Transfer in Excimer Laser Melting of Thin Polysilicon Layers", *ASME Journal of Heat Transfer*, **117,** 708-715, (1995).
5. Shamsundar, N., Sparrow, E.M., "Analysis of Multidimensional Conduction Phase Change Via the Enthalpy Method", *ASME Journal of Heat Transfer*, **97,** 333-340, (1975).
6. Minkowycz, W.J., Sparrow, E.M., *Advances in Numerical Heat Transfer*, Taylor and Francis Group, Washington, DC, 1996.
7. Jellison, G.E., "Measurements of the optical properties of liquid silicon and germanium using nanosecond time-resolved ellipsometry", *Applied Physics Letters*, **51,** 352-354, (1987).
8. Hull, R., *Properties of Crystalline Silicon*, The Instititution of Elec. Eng, London, 1999.

Appendix – 2

The Finite-Difference Time-Domain (FDTD) Method

Numerically solving Maxwell's equations eliminates the constraints of Mie theory described above. In their stead, other considerations arise including numerical inaccuracy, computational expense, and stability which will all be discussed. The finite-difference time-domain (FDTD) method was chosen as the investigative technique because it has the ability to incorporate arbitrary geometries as well as both dielectric and metallic materials used in the experiments.

The FDTD method explicitly marches through time by solving Maxwell's curl equations at the nodes of a discretized spatial grid. The relations are given by Eqs. (1) for a linear, isotropic material.

$$\nabla \mathrm{x} \mathrm{E} = -\mu \frac{\partial \mathrm{H}}{\partial t} \tag{1a}$$

$$\nabla \mathrm{x} \mathrm{H} = \sigma \mathrm{E} + \varepsilon \frac{\partial \mathrm{E}}{\partial t} \tag{1b}$$

The vectors E and H are the electric and magnetic field components, respectively, while ε is the electrical permittivity, σ is the electric conductivity, and μ is the magnetic permeability.

Kane Yee (1966) developed the algorithm to solve for both electric and magnetic field components in time and space. Solution of all field components allows treatment of both electric and magnetic materials, an advantage over previous methods of solving either the electric or the magnetic fields with a wave equation. The Yee algorithm is based upon the staggered lattice he introduced called the Yee cell, shown in Figure 1.

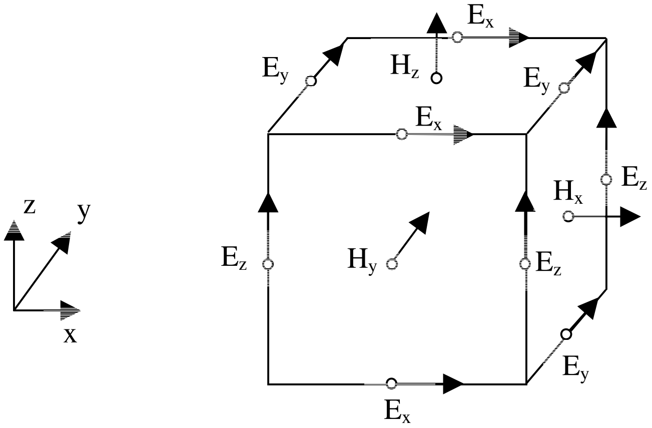

Figure 1: Electric and magnetic field components in a unit Yee cell

The solution method involves a leapfrog procedure in which the electric fields are solved using finite-differences at integer time-steps, while the magnetic components then access the electric vectors at integer-plus-1/2 time steps. This procedure as well as many advanced techniques are detailed in Taflove and Hagness (2005).

In anticipation of simulating metallic materials in the plasmonics investigation, the current density form of Maxwell's equations are used, which can treat negative real parts of the dielectric function defining reflection from metals as well as positive values defining dielectrics.

$$\frac{\partial \mathrm{E}}{\partial t}=\frac{1}{\varepsilon}[\nabla \mathrm{x} \mathrm{H}-\mathrm{J}] \tag{2a}$$

$$\frac{\partial \mathrm{H}}{\partial t}=-\frac{1}{\mu}[\nabla \mathrm{x} \mathrm{E}] \tag{2b}$$

$$\frac{\partial \mathrm{J}}{\partial t}=k_d \mathrm{J}+\beta \mathrm{E} \tag{2c}$$

where J is the electric current density vector, and k_d and β are material-based coefficients to be defined later.

Nano-optical simulations that realistically describe NOBEL lab experiments require additional FDTD implementations to the basic algorithm. One of the most important aspects of any FDTD environment is the boundary condition. In order to prevent spurious reflection of electromagnetic waves at the grid edges, an absorbing boundary condition (ABC) is needed. Mur (1981) and Liao et al. (1984) presented ABC's based on gradients in time and space. Though successful, both methods become unstable at many thousands of time steps and lose accuracy based on the incident angle of the wave at the boundary. Berenger (1994) introduced the perfectly-matched layer (PML) which eliminated angle dependence, increased absorption levels by two orders of magnitude and remained stable at the cost of splitting the field components and a difficult implementation. Gedney (1996) then presented the anisotropic PML or uniaxial PML (UPML) which retained the un-split field components and was proven mathematically identical to Berenger's PML. Currently the UPML is used by many high-end commercial and research codes with success. Roden and Gedney (2000) further increased the absorption precision and computational efficiency by an order of magnitude with their convolution PML (CPML). Gedney et al. (2001) have characterized the relative error due to the reflected wave that re-enters the FDTD environment with a ten cell CPML at ~10^{-5} to 10^$^{-6}$. The CPML is the most advanced and flexible ABC available, and is implemented in this work due to its accuracy and abilities to absorb evanescent waves and treat dispersive materials such as the noble metals in the plasmonic investigation.

The discretized versions of field components E_x, J_x, and H_x *with CPML incorporation* used for the explicit updates are given by

$$E_x\big|^{n+1/2}_{i+1/2,j,k} = C_a\big|_{i+1/2,j,k}\, E_x\big|^{n-1/2}_{i+1/2,j,k} + C_b\big|_{i+1/2,j,k} \left(\begin{array}{l} \dfrac{H_z\big|^{n}_{i+1/2,j+1/2,k} - H_z\big|^{n}_{i+1/2,j-1/2,k}}{\kappa_{y_j}\Delta y} - \dfrac{H_y\big|^{n}_{i+1/2,j,k+1/2} - H_y\big|^{n}_{i+1/2,j,k-1/2}}{\kappa_{z_k}\Delta z} \\ + \psi_{E_{x,y}}\big|^{n}_{i+1/2,j,k} - \psi_{E_{x,z}}\big|^{n}_{i+1/2,j,k} - \dfrac{1}{2}\left(1+k_d\right) J_x\big|^{n-1/2}_{i+1/2,j,k} \end{array}\right) \tag{3}$$

$$J_x\big|^{n+1/2}_{i+1/2,j,k} = k_d J_x\big|^{n-1/2}_{i+1/2,j,k} + \beta\left(\frac{E_x\big|^{n+1/2}_{i+1/2,j,k} - E_x\big|^{n-1/2}_{i+1/2,j,k}}{\Delta t}\right) \tag{4}$$

$$H_x\big|^{n+1}_{i,j+1/2,k+1/2} = D_a\big|_{i,j+1/2,k+1/2}\, H_x\big|^{n}_{i,j+1/2,k+1/2} - D_b\big|_{i,j+1/2,k+1/2} \left(\begin{array}{l} \dfrac{E_z\big|^{n+1/2}_{i,j+1,k+1/2} - E_z\big|^{n+1/2}_{i,j,k+1/2}}{\kappa_{y_{j+1/2}}\Delta y} - \dfrac{E_y\big|^{n+1/2}_{i,j+1/2,k+1} - E_y\big|^{n+1/2}_{i,j+1/2,k}}{\kappa_{z_{k+1/2}}\Delta z} \\ + \psi_{H_{x,y}}\big|^{n+1/2}_{i,j+1/2,k+1/2} - \psi_{H_{x,z}}\big|^{n+1/2}_{i,j+1/2,k+1/2} \end{array}\right) \tag{5}$$

where i, j, and k are the Cartesian indices. The terms $\psi_{E_{i,j}}$ and $\psi_{H_{i,j}}$ are stored only in the CPML regions with i-normal and j-normal interface boundaries and act as radiation sources to destructively interfere with the waves hitting the boundary. The CPML regions are ten-cell thick slabs on each of the six faces of the Cartesian FDTD environment. The CPML terms are defined by

$$\psi_{E_{x,y}}\big|^{n}_{i+1/2,j,k} = b_y \psi_{E_{x,y}}\big|^{n-1}_{i+1/2,j,k} + c_y\left(\frac{H_z\big|^{n}_{i+1/2,j+1/2,k} - H_z\big|^{n}_{i+1/2,j-1/2,k}}{\Delta y}\right) \tag{6a}$$

$$\psi_{E_{x,z}}\big|^{n}_{i+1/2,j,k} = b_z \psi_{E_{x,z}}\big|^{n-1}_{i+1/2,j,k} + c_z\left(\frac{H_y\big|^{n}_{i+1/2,j,k+1/2} - H_y\big|^{n}_{i+1/2,j,k-1/2}}{\Delta z}\right) \tag{6b}$$

$$\psi_{H_{x,y}}\Big|_{i,j+1/2,k+1/2}^{n+1/2} = b_y \psi_{H_{x,y}}\Big|_{i,j+1/2,k+1/2}^{n-1/2} + c_y \left(\frac{E_z\big|_{i,j+1,k+1/2}^{n+1/2} - E_z\big|_{i,j,k+1/2}^{n+1/2}}{\Delta y} \right) \quad \text{(6c)}$$

$$\psi_{H_{x,z}}\Big|_{i,j+1/2,k+1/2}^{n+1/2} = b_z \psi_{H_{x,z}}\Big|_{i,j+1/2,k+1/2}^{n-1/2} + c_z \left(\frac{E_y\big|_{i,j+1/2,k+1}^{n+1/2} - E_y\big|_{i,j+1/2,k}^{n+1/2}}{\Delta z} \right) \quad \text{(6d)}$$

with coefficients b_w and c_w given by

$$b_w = e^{-\left(\frac{\sigma_w}{\varepsilon_0 \kappa_w} + \frac{a_w}{\varepsilon_0}\right)\Delta t} \quad \text{(7)}$$

$$c_w = \frac{\sigma_w}{\sigma_w \kappa_w + \kappa_w^2 a_w} \left[e^{-\left(\frac{\sigma_w}{\varepsilon_0 \kappa_w} + \frac{a_w}{\varepsilon_0}\right)\Delta t} - 1 \right] \quad \text{(8)}$$

The scaled tensors κ_w, σ_w, and a_w are important parameters that act within the CPML terms to damp the electromagnetic waves as they travel through the ten-cell region, reflect off the perfect-electric conductor final outer boundary, and travel back through the CPML region a second time. The exact scaling of these parameters is simulation-specific. For the results presented in this work, the parameters are defined by the polynomial grading:

$$\sigma_x(x) = \sigma_{x,\max} \left(\frac{x}{d} \right)^m \quad \text{(9)}$$

$$\kappa_x(x) = 1 + (\kappa_{x,\max} - 1)\left(\frac{x}{d} \right)^m \quad \text{(10)}$$

$$a_x(x) = a_{x,\max} \left(\frac{d - x}{d} \right) \quad \text{(11)}$$

using $a_{x,\max}$ =0.2, $\kappa_{x,\max}$ =1 (vacuum boundary), and

$$\sigma_{x,\max} = \frac{0.8(m+1)}{\eta_0 \Delta \sqrt{\varepsilon_0 \mu_0}} \quad \text{(12)}$$

where η_0 is the free-space wave impedance, Δ is the cubic lattice cell dimension, ε_0 and μ_0 are the permittivity and permeability of free space, and m is the polynomial grade=3. The constant d defines the thickness of the CPML (here d=10).

Returning to Eqs. (3-5), the material coefficients C_a, C_b, D_a, D_b, k_d, and β are defined at individual node calculations, and characterize the mesh with a physical nanostructure or free space. For non-dispersive materials, such as the dielectric simulations to be presented, the coefficients take the form

$$C_a = \left(1 - \frac{\sigma \Delta t}{2\varepsilon}\right) / \left(1 + \frac{\sigma \Delta t}{2\varepsilon}\right) \tag{13}$$

$$C_b = \left(\frac{\Delta t}{\varepsilon}\right) / \left(1 + \frac{\sigma \Delta t}{2\varepsilon}\right) \tag{14}$$

$$D_a = \left(1 - \frac{\sigma^* \Delta t}{2\mu}\right) / \left(1 + \frac{\sigma^* \Delta t}{2\mu}\right) \tag{13}$$

$$D_b = \left(\frac{\Delta t}{\mu}\right) / \left(1 + \frac{\sigma^* \Delta t}{2\mu}\right) \tag{14}$$

where Δt is the timestep, and σ^* is the magnetic loss (generally=0 ohms/m), while k_d=1 and β=0. Material parameters for dispersive materials such as gold and silver are more complicated and will be covered in Chapter 4 of this work. Field components E_y, J_y, H_y, and E_z, J_z, H_z can be determined analogously by permuting the i, j, and k indices appropriately.

With the FDTD interior, boundary, and material definition procedures in place, the excitation field is required for a transient scattering analysis. The experimental condition of a monochromatic plane wave has been implemented in FDTD using the total field/scattered field (TFSF) formulation with matched dispersion compensation. The assumption of no spatial variation of intensity (pre-interaction) is made, reasonable because the Gaussian profile of the beams used are resolved on the order of millimeters, compared to the micrometer simulation environment.

The TFSF construct (Yee, 1966) takes advantage of the linearity of Maxwell's equation, meaning the total electric (and likewise magnetic) field is equal to the sum of the incident and scattered electric fields. The incident field is arbitrary and user-defined. The procedure involves choosing a total field zone that contains the object of interest (micro sphere and substrate) and designating six planar faces that mark the boundary of this cube-within-a-cube. Straddling the boundary will be electric and magnetic field pairs whose connection would intersect perpendicularly with the TFSF plane. At every node on these planes, the incident field is either added or subtracted, depending on the component, directly resulting in the generation of the plane wave within the TFSF zone. Because only the incident field is subtracted, the TFSF boundaries are transparent to scattered radiation. E_x and H_x field components straddling the y-minimum TFSF plane would be modified as follows.

$$E_x\Big|_{i,j0,k}^{n+1} = \left\{E_x\Big|_{i,j0,k}^{n+1}\right\}_{2.16} - \frac{\Delta t}{\varepsilon_0 \Delta} H_{z,inc}\Big|_{i,j-1/2,k}^{n+1/2} \tag{15}$$

$$H_x\Big|_{i,j0-1/2,k}^{n+1/2} = \left\{H_x\Big|_{i,j0-1/2,k}^{n+1/2}\right\}_{2.18} + \frac{\Delta t}{\mu_0 \Delta} E_{z,inc}\Big|_{i,j0,k}^{n} \tag{16}$$

The bracketed terms in Eqs. (15) and (16) indicate the original update values performed using Eqs. (3) and (5). The incident field components are obtained through a number of steps. First, a one-dimensional auxiliary FDTD grid is used as a lookup table. The sinusoidal waveform in this grid would continuously propagate defined by the excitation

$$E_{inc,0} = I_0 \sin(\omega \cdot t \cdot \Delta t) \tag{17}$$

where ω is the desired laser frequency. Then, a user-specified orientation is accessed. The plane wave can propagate through the Cartesian space at any incident angle θ and Φ. These values define the origin corner of the TFSF zone. A linear distance from this origin to each node is calculated, giving a correlation between a point on the TFSF planes and the 1-D auxiliary grid. Next, the Yee algorithm is modified for auxiliary grid calculation to account for numerical dispersion. In any discretized grid, a numerical phase-velocity anisotropy will occur that will lead to field leakage from the TFSF zone if unaddressed. Taflove and Hagness (2005) detail the dispersion compensation techniques needed for inclusion in the 1-D FDTD algorithm. Finally, an appropriate trigonometric function based on the propagation angles is applied to each field component to obtain the Cartesian vector magnitudes.

In order to maintain numerical stability, the Courant condition must be satisfied regarding the time step employed:

$$\Delta t < \frac{1}{c\sqrt{\frac{1}{(\Delta x)^2} + \frac{1}{(\Delta y)^2} + \frac{1}{(\Delta z)^2}}} \tag{18}$$

An additional requirement to yield accurate results is keeping the largest grid spacing, Δx, Δy, or Δz much less than the smallest wavelength (< λ/10) that will be propagating through the system. In order to resolve structures at the nanoscale with clarity, this requirement generally takes care of itself. Grid spacing used in this work maintained λ/25 to λ/1000 fidelity. The FDTD modeling environment and numerical algorithm for the developed code (MaxTex) are given in Figures 2 and 3.

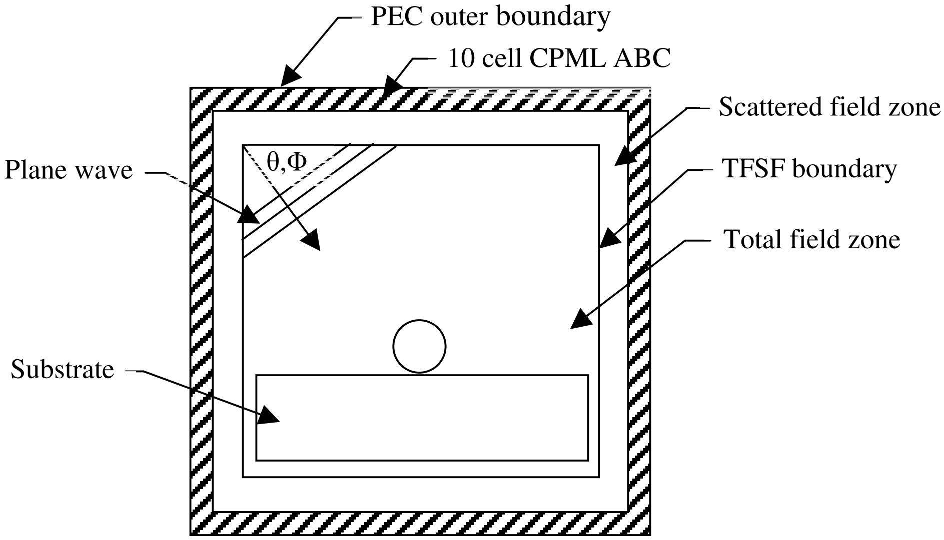

Figure 2: 2-D cross-section of 3-D FDTD modeling environment

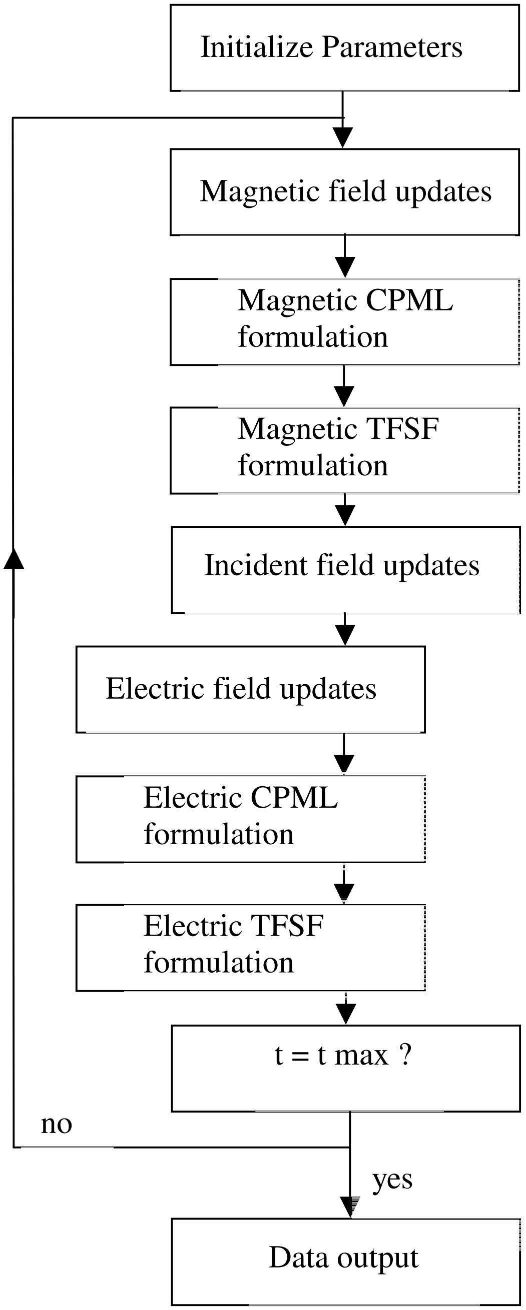

Figure 3: FDTD algorithm employed in MaxTex code

Bibliography

Chapter 1

1. Maiman, T.H., "Stimulated optical radiation in ruby", *Nature*, **187,** 493, (1960).
2. Svelto, O., *Principles of lasers*, Plenum Press, New York, 1989.
3. Duley, W.W., *Laser processing and analysis of materials*, Plenum Press, New York, 1983.
4. Born, W., and Wolf, E., *Principles of optics*, 6th edition, Pergamon, Oxford, 1980.
5. Zhang, X., Grigoropoulos, C. P., Kranjnovich, D. J., and Tam, A. C., "Excimer laser projection micromachining of polyimide thin films annealed at different temperatures", *IEEE Transactions on Components, Packaging and Manufacturing Technology: Part C (Manufacturing)*, **119,** 201-213, (1996).
6. Wood, R.F., White, C.W., and Young, R.T., *Semiconductors and semimetals*, Academic Press, Orlando, 1984.
7. Zergioti, I., Mailis, S., Fotakis, C., Chen, S.C., and Grigoropoulos, C.P., "Microdeposition of metals by femtosecond excimer laser", *Applied Surface Science*, **127-129,** 601-605, (1998).
8. Park, H.K., Xu, X., Grigoropoulos, C. P., Do, N., Klees, L., Leung, P. T., and Tam, A. C., "Transient optical transmission measurement in excimer laser irradiation of amorphous silicon films", *Transactions of ASME Journal of Heat Transfer*, **115,** 178-183, (1993).
9. Williams, E.W., *The cd-rom and optical disc recording systems*, Oxford University Press, Oxford, 1994.
10. Tam, A.C., Leung, W.P., Zapka, W., and Ziemlich, W., "Laser cleaning techniques for removal of surface particulates", *Journal of Applied Physics*, **71,** 3515-3523, (1992).
11. Nakata, Y., Kumuduni, W.K.A., Okada,T., and Maeda, M., "Plume-substrate interaction in pulsed-laser deposition of high-temperature superconducting thiin films", *Applied Physics Letters*, **64,** 2599-2601, (1994).
12. Fogarassy, E., Pattyn, H., Elliq, M., Slaoui, A., Prevot, B., Stuck, R., Unamuno, S., and Mathe, E. L., "Pulsed laser cystallization and doping for the fabrication of high quality poly-si tfts", *Applied Surface Science*, **69,** 231-241, (1993).
13. Endert, H., Galvanauskas, A.,Sucha, G., Patel, R., and Stock, M., "Novel ultrashort pulse fiber lasers for micromachining applications", *RIKEN Review*, **43,** 23-27, (2002).

14. Matz, R., Weber, H., and Weimann, G., "Laser-induced dry etching of integrated inp microlenses", *Applied Physics A: Materials Science & Processing*, **65,** 349-353, (1997).

15. Lu, Y.F., Takai, M., Komuro, S., Shiokawa, T., and Aoyagi, Y., "Surface cleaning of metals by pulsed-laser irradiation in air", *Applied Physics A: Materials Science & Processing*, **59,** 281-288, (1994).

16. Sato, S., Inaba, H., "Optical trapping and manipulation of microscopic particles and biological cells by laser beams", *Optical and Quantum Electronics* **28,** 1-16, (1996).

17. Malek, C.K., Saile, V., "Applications of liga technology to precision manufacturing of high-aspect-ratio micro-components and systems: A review", *Microelectronics Journal*, **35,** 131-143, (2004).

18. Kitai, M.S., Popkopv, V.L., Semchishen, V.A., and Kharizov, A.A., "The physics of uv laser cornea ablation", *IEEE Journal of Quantum Electronics*, **27,** 303-307, (1991).

19. Vogel, A., Schweiger, P., friieser, A., Asiyo, M.N., and Birngber, R., "Intraocular nd:Yag laser surgery: Light-tissue interaction, damage, and reduction of collateral effects", *IEEE Journal of Quantum Electronics*, **26,** 2240-2260, (1990).

20. Boyd, I.W., *Laser processing of thin films and microstructures.*, Springer-Verlag, Berlin, 1987.

21. Fann, W.S., Storz, R., Tom, H.W.K., and Bokor, J., "Direct measurement of non-equilibrium laser-heated gold films", *Physical Review Letters*, **68,** 2834-2837, (1992).

22. Fujimoto, J.G., Liu, J.M., and Ippen, E.P., "Femtosecond laser interaction with metallic tungsten and non-equilibrium electron and lattice temperatures", *Physical Review Letters*, **53,** 1837-1840, (1984).

23. Rogers, T. and Kowal, J., "Selection of glass, anodic bonding conditions and material compatibility for silicon-glass capacitive sensors", *Sensors and Actuators a-Physical*, **46,** 113-120, (1995).

24. Carabe, J., Gandia, J.J., "Thin-film-silicon solar cells", *Opto-Electronics Review*, **12,** 1-6, (2004).

25. Wilson, A.R., Olsson-Jacques, C., Muscat, R.F. *Adhesive bond degradation sensor*. in *Proceedings of the SPIE - The International Society for Optical Engineering*. 2002.

26. Zhang S., Z., W., Zhang, S.C., Yao, S., "The research status of soi high-temperature pressure sensor", *Journal of Hebei University of Technology*, **34,** 14-19, (2005).

27. Smith, C.S., "Piezoresistance effect in germanium and silicon", *Physical Review*, **94,** 42-49, (1954).

28. Kim. C., a.K.Y., "Micro xy-stage using silicon on a glass substrate", *Journal of Micromechanics and Microsystems*, **12,** 103-107, (2002).

29. Madou, M.J., *Fundamentals of microfabrication*, 2nd edition, CRC Press, Boca raton, FL, 2002.

30. Roylance, L., Angell. J. *A miniature integrated circuit accelerometer*. in *Solid State Circuits Conference*. 1978.

31. Rusu, C., "Direct integration of micromachined pipettes in a flow channel for single DNA molecule study by optical tweezers," *Journal of Micromechanical Systems*, **10,** 238-246, (2001).

32. Luginbuhl, P. *Micromachined injector for DNA mass spectrometry*. in *Proceedings of Transducers '99*. 1999.

33. Zheng, W.a.C., S.C. *Continuous flow, submicroliter scale pcr chip for DNA amplification*. in *Proceedings of SPIE - the International Society for Optical Engineering*. 2001.

34. Simpson, P.C., Woolley, A.T., and Mathies, R.A., "Microfabrication technology for the production of capillary array electrophoresis chips", *Biomedical Microdevice*, **1/1,** 7-25, (1998).

35. Iliescu, C., "Fabrication of a dielectrophoretic chip with 3d silicon electrodes", *Journal of Micromechanics and Microsystems*, **15/3,** 494-500, (2005).

36. Rothschild, M., Bloomstein, T.M., Curtin, J.E., Downs, D.K., Fedynyshyn, T.H., Hardy, D.E., Kunz, R.R., Liberman, V., Sedlacek, J.H.C., Uttaro, R.S., Bates, A.K., and Van Peski, C., "157 nm: Deepest deepultraviolet yet", *Journal of vacuum Science and Technology B*, **17,** 3262-3266, (1999).

37. Gwyn, C.W., Stulen, R., Sweeney, D., and Attwood, D., "Extreme ultraviolet lithography", *Journal of Vacuum Science and Technology B*, **16,** 3142-3149, (1998).

38. Silverman, J.P., "Challenges and progress in x-ray lithography", *Journal of Vacuum Science and Technology B*, **16,** 3137-3141, (1998).

39. Gwyn, C. *Euv llc program status and plans*. in *1st EUVL Workshop*. 2001. Tokyo.

40. Hector, S.D. *Euvl masks: Requirements and potential solutions*. in *Emerging Lithographic technologies VI, SPIE Proceedings*. 2002.

41. Gibson, S.F., and Lanni, F., "Experimental test of an analytical model of aberration in an oil-immersion objective lens used in three-dimensional microscopy", *journal of Optical Society of America*, **8,** 1601-1613, (1991).

42. Hirota, K., Milster, T.D., Shimura, K., Zhang, Y., and Jo, J.S., "Near-field phase change optical recording using a gap hemispherical lens", *Japanese Journal of Applied Physics Part I - Regular Papers, Short Notes & review Papers*, **39,** 968-972, (2000).

43. Okazaki, S., "Resolution limits of optical lithography", *Journal of Vacuum Science and Technology*, **B9,** 2829-2833, (2001).

44. Ohtsu, M., and Hori, H., *Near-field nano-optics*, Kluwer Academic, New York, 1999.

45. Betzig, E. and Trautman, J.K., "Near-field optics - microscopy, spectroscopy, and surface modification beyond the diffraction limit", *Science*, **257,** 189-195, (1992).

46. Munzer, H.J., Mosbacher, M., Bertsch, M., Zimmermann, J., Leiderer, P., and Boneberg, J., "Local held enhancement effects for nanostructuring of surfaces", *Journal of Microscopy-Oxford*, **202,** 129-135, (2001).

47. Heltzel, A.J., Theppakuttai, S., Howell, J.R., and Chen,S.C., "Analytical and experimental investigation of laser-nanosphere interaction for nanoscale surface modification", *Journal of Heat Transfer*, **127,** 1231-1235, (2005).

Chapter 2

1. Gosele, U., and Tong, Q. Y., "Semiconductor wafer bonding", *Annual Review of Materials Science,* **28**, 215-241, (1998).

2. Gosele, U. et al., "Fundamental issues in wafer bonding", *Journal of Vacuum Science & Technology A,* **17**, 1145-1152, (1999).

3. Gosele, U., Tong, Q. Y., Schumacher, A., Krauter, G., Reiche, M., Plossl, A., Kopperschmidt, P., Lee, T. H., and Kim, W. J., "Wafer bonding for microsystems technologies", *Sensors and Actuators a-Physical,* **74**, 161-168, (1999).

4. Haisma, J., Spierings, B. A. C. M., Biermann, U. K. P., and Vangorkum, A. A., "Diversity and Feasibility of Direct Bonding - a Survey of a Dedicated Optical-Technology", *Applied Optics,* **33**, 1154-1169, (1994).

5. Galileo Galilei, *Discorsi E DimostrazioniMatematiche* (1638).

6. Haisma, J., and Spierings, G. A. C. M., "Contact bonding, including direct-bonding in a historical and recent context of materials science and technology, physics and chemistry - Historical review in a broader scope and comparative outlook", *Materials Science & Engineering R-Reports,* **37**, 1-60, (2002).

7. Rayleigh., L., *Proceedings of Physical Society A,* **156**, 326-349, (1936).

8. Israelachvili, J., *Intermolecular and Surface Forces* (Academic, London, 1991).

9. Pomerantz, G. W. a. D. I., "Field Assisted Glass-Metal Sealing", *Journal of Applied Physics,* **40**, 3946-3949, (1969).

10. Rogers, T., and Kowal, J., "Selection of Glass, Anodic Bonding Conditions and Material Compatibility for Silicon-Glass Capacitive Sensors", *Sensors and Actuators a-Physical,* **46**, 113-120, (1995).

11. Savage, G., *A Concise History of Bronzes* (Thomes & Hudson, London, 1968).

12. Wolf, D., "Should All Surfaces Be Reconstructed", *Physical Review Letters,* **70**, 627-630, (1993).

13. Hanfmann, G. M. A. (New York Graphic Society, Greenwitch, CT, USA).

14. Chen, M. X., Yi, X. J., Gan, Z. Y., and Liu, S., "Reliability of anodically bonded silicon-glass packages", *Sensors and Actuators a-Physical,* **120**, 291-295, (2005).

15. Aljancic, U., Resnik, D., Vrtacnik, D., Mozek, M., and Amon, S., "Silicon-glass anodic bonding", *Informacije Midem-Journal of Microelectronics Electronic Components and Materials,* **34**, 168-173, (2004).

16. Xing, Q. F., Yoshida, M., and Sasaki, G., "TEM study of the interface of anodic-bonded Si/glass", *Scripta Materialia,* **47**, 577-582, (2002).

17. Gerlach, A., Maas, D., Seidel, D., Bartuch, H., Schundau, S., and Kaschlik, K., "Low-temperature anodic bonding of silicon to silicon wafers by means of intermediate glass layers", *Microsystem Technologies-Micro-and Nanosystems-Information Storage and Processing Systems,* **5**, 144-149, (1999).

18. Yousefpour, A., Hojjati, M., and Immarigeon, J. P., "Fusion bonding/welding of thermoplastic composites", *Journal of Thermoplastic Composite Materials,* **17**, 303-341, (2004).

19. Xiao, Z. X., Wu, G. Y., Li, Z. H., Zhang, C. B., Hao, Y. L., and Wang, Y. Y., "Silicon-glass wafer bonding with silicon hydrophilic fusion bonding technology", *Sensors and Actuators a-Physical,* **72**, 46-48, (1999).

20. Henmi, H., Shoji, S., Shoji, Y., Yoshimi, K., and Esashi, M., "Vacuum Packaging for Microsensors by Glass Silicon Anodic Bonding", *Sensors and Actuators a-Physical,* **43**, 243-248, (1994).

21. Kutchoukov, V. G., Laugere, F., van der Vlist, W., Pakula, L., Garini, Y., and Bossche, A., "Fabrication of nanofluidic devices using glass-to-glass anodic bonding", *Sensors and Actuators a-Physical,* **114**, 521-527, (2004).

22. Goustouridis, D., Minoglou, K., Kolliopoulou, S., Chatzandroulis, S., Morfouli, P., Normand, P., and Tsoukalas, D., "Low temperature wafer bonding for thin silicon film transfer", *Sensors and Actuators a-Physical,* **110**, 401-406, (2004).

23. Chiao, M., and Lin, L. W., "Hermetic wafer bonding based on rapid thermal processing", *Sensors and Actuators a-Physical,* **91**, 398-402, (2001).

24. Chiao, M., and Lin, L. W., "Accelerated hermeticity testing of a glass-silicon package formed by rapid thermal processing aluminum-to-silicon nitride bonding", *Sensors and Actuators a-Physical,* **97-8**, 405-409, (2002).

25. Wei, J., Nai, S. M. L., Wong, C. K. S., Sun, Z., and Lee, L. C., "Low temperature glass-to-glass wafer bonding", *Ieee Transactions on Advanced Packaging,* **26**, 289-294, (2003).

26. Bower, R. W., and Chin, F. Y. J., "Low temperature direct silicon wafer bonding using argon activation", *Japanese Journal of Applied Physics Part 2-Letters,* **36**, L527-L528, (1997).

27. Bower, R. W., Ismail, M. S., and Roberds, B. E., "Low-Temperature Si3n4 Direct Bonding", *Applied Physics Letters,* **62**, 3485-3487, (1993).

28. Lin, L. W., "MEMS post-packaging by localized heating and bonding", *Ieee Transactions on Advanced Packaging,* **23**, 608-616, (2000).

29. Cheng, Y. T., Lin, L. W., and Najafi, K., "Localized silicon fusion and eutectic bonding for MEMS fabrication and packaging", *Journal of Microelectromechanical Systems,* **9**, 3-8, (2000).

30. Kagan, V. A., Bray, R. G., and Kuhn, W. P., "Laser transmission welding of semi-crystalline thermoplastics - Part I: Optical characterization of nylon based plastics", *Journal of Reinforced Plastics and Composites,* **21**, 1101-1122, (2002).

31. Kagan, V. A., and Pinho, G. P., "Laser transmission welding of semicrystalline thermoplastics - Part II: Analysis of mechanical performance of welded nylon", *Journal of Reinforced Plastics and Composites,* **23**, 95-107, (2004).

32. Lin, L. W., "Thermal challenges in MEMS applications: phase change phenomena and thermal bonding processes", *Microelectronics Journal,* **34**, 179-185, (2003).

33. Jee, Y., and Woodard, O. C., "Laser Application in Packaging of Very Large-Scale Integrated Chips", *Journal of Vacuum Science & Technology B,* **8**, 1789-1793, (1990).

34. Hayward, J. D., "Optimization and Reliability Evaluation of a Laser Inner Lead Bonding Process", *Ieee Transactions on Components Packaging and Manufacturing Technology Part B-Advanced Packaging,* **17**, 547-553, (1994).

35. Tao, Y., Malshe, A. P., and Brown, W. D., "Investigation of laser-assisted bonding for MEMS packaging", *International Journal of Nonlinear Sciences and Numerical Simulation,* **3**, 427-431, (2002).

36. Kim, J., and Xu, X. F., "Excimer laser fabrication of polymer microfluidic devices", *Journal of Laser Applications,* **15**, 255-260, (2003).

37. Luo, C., and Lin, L. W., "The application of nanosecond-pulsed laser welding technology in MEMS packaging with a shadow mask", *Sensors and Actuators a-Physical,* **97-8**, 398-404, (2002).

38. Mescheder, U. M., Alavi, M., Hiltmann, K., Lietzau, C., Nachtigall, C., and Sandmaier, H., "Local laser bonding for low temperature budget", *Sensors and Actuators a-Physical,* **97-8**, 422-427, (2002).

39. Wild, M. J., Gillner, A., and Poprawe, R., "Locally selective bonding of silicon and glass with laser", *Sensors and Actuators a-Physical,* **93**, 63-69, (2001).

40. Hatano, M., Moon, S., Lee, M., Suzuki, K., and Grigoropoulos, C. P., "Excimer laser-induced temperature field in melting and resolidification of silicon thin films", *Journal of Applied Physics,* **87**, 36-43, (2000).

41. Xu, X., Grigoropoulos, C. P., and Russo, R. E., "Nanosecond-time-resolution thermal emission measurement during pulsed excimer-laser interaction with materials", *Applied Physics a-Materials Science & Processing,* **62**, 51-59, (1996).

42. Chen, G., and Tien, C. L., "Thermally-Induced Optical Nonlinearity During Transient Heating of Thin-Films", *Journal of Heat Transfer-Transactions of the Asme,* **116**, 311-316, (1994).

43. Abraham, E., and Halley, J. M., "Some Calculations of Temperature Profiles in Thin-Films with Laser-Heating", *Applied Physics a-Materials Science & Processing,* **42**, 279-285, (1987).

44. Bloisi, F., Vicari, L., Cavaliere, P., Martellucci, S., Quartieri, J., Mormile, P., and Pierattini, G., "Laser-Induced Thermal Profiles in Thermally and Optically Thin-Films", *Applied Physics B-Photophysics and Laser Chemistry,* **47**, 67-69, (1988).

45. Burgener, M. L., and Reedy, R. E., "Temperature Distributions Produced in a 2-Layer Structure by a Scanning Cw Laser or Electron-Beam", *Journal of Applied Physics,* **53**, 4357-4363, (1982).

46. Jellison, G. E., and Lowndes, D. H., "Optical-Absorption Coefficient of Silicon at 1.152-Mu at Elevated-Temperatures", *Applied Physics Letters,* **41**, 594-596, (1982).

47. Schmidt, H., Scholze, H., and Kaiser, A., "Contribution to the Kinetics of Glass-Formation from Solutions", *Journal of Non-Crystalline Solids,* **48**, 65-77, (1982).

48. Bansal, C., and Srinivasan, V., "Microscopic Theory for the Glass State", *Physics Letters A,* **75**, 420-422, (1980).

Chapter 3

1. Helztel, A., Theppakuttai, S., Howell, J., Chen, S., "Analytical and Experimental Investigation of Laser-Microsphere Interaction for Nanoscale Surface Modification", *Journal of Heat transfer, in press*, (2005).

2. Petersen, K. E., "Silicon as a Mechanical Material", *Proceedings of the Ieee,* **70**, 420-457, (1982).

3. Yuan, B., and Sharpe, W. N., "Mechanical testing of polysilicon thin films with the ISDG", *Experimental Techniques,* **21**, 32-35, (1997).

4. Sharpe, W. N., Yuan, B., and Edwards, R. L., "A new technique for measuring the mechanical properties of thin films", *Journal of Microelectromechanical Systems,* **6**, 193-199, (1997).

5. Sharpe, W. N., Vaidyanathan, R., Yuan, B., Bao, G., and Edwards, R. L., "Effect of etch holes on the mechanical properties of polysilicon", *Journal of Vacuum Science & Technology B,* **15**, 1599-1603, (1997).

6. Lang, W., "Silicon microstructuring technology", *Materials Science & Engineering R-Reports,* **17**, 1-55, (1996).

7. Weller, D. et al., "Ion induced magnetization reorientation in Co/Pt multilayers for patterned media", *Journal of Applied Physics,* **87**, 5768-5770, (2000).

8. Terris, B. D., Weller, D., Folks, L., Baglin, J. E. E., Kellock, A. J., Rothuizen, H., and Vettiger, P., "Patterning magnetic films by ion beam irradiation", *Journal of Applied Physics,* **87**, 7004-7006, (2000).

9. Reyntjens, S., and Puers, R., "A review of focused ion beam applications in microsystem technology", *Journal of Micromechanics and Microengineering,* **11**, 287-300, (2001).

10. Rubanov, S., and Munroe, P. R., "FIB-induced damage in silicon", *Journal of Microscopy-Oxford,* **214**, 213-221, (2004).

11. Ali, M. Y., and Hung, N. P., "Surface roughness of sputtered silicon. II. Model verification", *Materials and Manufacturing Processes,* **16**, 315-329, (2001).

12. Ali, M. Y., and Hung, N. P., "Surface roughness of sputtered silicon. I. Surface modeling", *Materials and Manufacturing Processes,* **16**, 297-313, (2001).

13. Gago, R., Vazquez, L., Cuerno, R., Varela, M., Ballesteros, C., and Albella, J. M., "Nanopatterning of silicon surfaces by low-energy ion-beam sputtering: dependence on the angle of ion incidence", *Nanotechnology,* **13**, 304-308, (2002).

14. Schmidt, B., Bischoff, L., and Teichert, J., "Writing FIB implantation and subsequent anisotropic wet chemical etching for fabrication of 3D structures in silicon", *Sensors and Actuators a-Physical,* **61**, 369-373, (1997).

15. Prestigiacomo, M., Roussel, L., Houel, A., Sudraud, P., Bedu, F., Tonneau, D., Safarov, V., and Dallaporta, H., "Studies of structures elaborated by focused ion beam induced deposition", *Microelectronic Engineering,* **76**, 175-181, (2004).

16. Melngailis, J., Mondelli, A. A., Berry, I. L., and Mohondro, R., "A review of ion projection lithography", *Journal of Vacuum Science & Technology B,* **16**, 927-957, (1998).

17. Tseng, A. A., "Recent developments in nanofabrication using ion projection lithography", *Small,* **1**, 594-608, (2005).

18. Dial, O., Cheng, C. C., and Scherer, A., "Fabrication of high-density nanostructures by electron beam lithography", *Journal of Vacuum Science & Technology B,* **16**, 3887-3890, (1998).

19. Hu, S. F., Weng, W. C., and Wan, Y. M., "Fabrication of silicon nanowire structures based on proximity effects of electron-beam lithography", *Solid State Communications,* **130**, 111-114, (2004).

20. Borini, S., Rossi, A. M., Boarino, L., and Amato, G., "Patterning of porous silicon by electron-beam lithography", *Journal of the Electrochemical Society,* **150**, G311-G313, (2003).

21. Snow, E. S., and Campbell, P. M., "Fabrication of Si Nanostructures with an Atomic-Force Microscope", *Applied Physics Letters,* **64**, 1932-1934, (1994).

22. Bo, X. Z., Rokhinson, L. P., Yin, H. Z., Tsui, D. C., and Sturm, J. C., "Nanopatterning of Si/SiGe electrical devices by atomic force microscopy oxidation", *Applied Physics Letters,* **81**, 3263-3265, (2002).

23. Ara, M., Graaf, H., and Tada, H., "Atomic force microscope anodization of Si(111) covered with alkyl monolayers", *Japanese Journal of Applied Physics Part 1-Regular Papers Short Notes & Review Papers,* **41**, 4894-4897, (2002).

24. Santinacci, L., Djenizian, T., and Schmuki, P., "Atomic force microscopy-induced nanopatterning of Si(100) surfaces", *Journal of the Electrochemical Society,* **148**, C640-C646, (2001).

25. Campbell, P. M., Snow, E. S., and McMarr, P. J., "AFM-based fabrication of Si nanostructures", *Physica B,* **227**, 315-317, (1996).

26. Snow, E. S., Campbell, P. M., and McMarr, P. J., "AFM-based fabrication of free-standing Si nanostructures", *Nanotechnology,* **7**, 434-437, (1996).

27. Matsumoto, K., Takahashi, S., Ishii, M., Hoshi, M., Kurokawa, A., Ichimura, S., and Ando, A., "Application of Stm Nanometer-Sire Oxidation Process to Planar-Type Mim Diode", *Japanese Journal of Applied Physics Part 1-Regular Papers Short Notes & Review Papers,* **34**, 1387-1390, (1995).

28. Held, R., Vancura, T., Heinzel, T., Ensslin, K., Holland, M., and Wegscheider, W., "In-plane gates and nanostructures fabricated by direct oxidation of semiconductor heterostructures with an atomic force microscope", *Applied Physics Letters,* **73**, 262-264, (1998).

29. Salling, C. T., "Direct patterning of Si(001) surfaces by atomic manipulation", *Journal of Vacuum Science & Technology B,* **14**, 1322-1326, (1996).

30. Iwasaki, H., Yoshinobu, T., and Sudoh, K., "Nanolithography on SiO_2/Si with a scanning tunnelling microscope", *Nanotechnology,* **14**, R55-R62, (2003).

31. Dumas, P., Gu, M., Syrykh, C., Hallimaoui, A., Salvan, F., and Gimzewski, J. K., "Nanostructuring of Porous Silicon Using Scanning-Tunneling-Microscopy", *Journal of Vacuum Science & Technology B,* **12**, 2067-2069, (1994).

32. Abeln, G. C., Lee, S. Y., Lyding, J. W., Thompson, D. S., and Moore, J. S., "Nanopatterning organic monolayers on Si(100) by selective chemisorption of norbornadiene", *Applied Physics Letters,* **70**, 2747-2749, (1997).

33. Oishi, T., Goto, A., Pihosh, Y., Kasahara, A., and Tosa, A., "Silicon microstructure fabricated by laser micro-patterning method combined with wet etching process", *Applied Surface Science,* **241**, 223-226, (2005).

34. Mucklich, F., Lasagni, A., and Daniel, C., "Laser interference metallurgy-periodic surface patterning and formation of intermetallics", *Intermetallics,* **13**, 437-442, (2005).

35. Mei, P., Boyce, J. B., Lu, J. P., Ho, J., and Fulks, R. T., "Pulsed laser crystallization and doping for thin film transistors", *Journal of Non-Crystalline Solids,* **266**, 1252-1259, (2000).

36. Huang, S. M., Hong, M. H., Luk'yanchuk, B. S., Lu, Y. F., Song, W. D., and Chong, T. C., "Sub-50 nm nanopatterning of metallic layers by green pulsed laser combined with atomic force microscopy", *Journal of Vacuum Science & Technology B,* **20**, 1118-1125, (2002).

37. Li, L. P., Lu, Y. F., Doerr, D. W., Alexander, D. R., Shi, J., and Li, J. C., "Fabrication of hemispherical cavity arrays on silicon substrates using laser-assisted nanoimprinting of self-assembled particles", *Nanotechnology,* **15**, 333-336, (2004).

38. Huang, S. M., Hong, M. H., Lu, Y. F., Lukyanchuk, B. S., Song, W. D., and Chong, T. C., "Pulsed-laser assisted nanopatterning of metallic layers combined with atomic force microscopy", *Journal of Applied Physics,* **91**, 3268-3274, (2002).

39. Leviatan, Y., "Study of near-Zone Fields of a Small Aperture", *Journal of Applied Physics,* **60**, 1577-1583, (1986).

40. Betzig, E., and Trautman, J. K., "Near-Field Optics - Microscopy, Spectroscopy, and Surface Modification Beyond the Diffraction Limit", *Science,* **257**, 189-195, (1992).

41. Ohtsu M., a. H. H., *Near-field Nano-optics* (Kluwer Academic, New York, 1999).

42. Halfpenny, D. R., and Kane, D. M., "A quantitative analysis of single pulse ultraviolet dry laser cleaning", *Journal of Applied Physics,* **86**, 6641-6646, (1999).

43. Hasegawa, M., Ikawa, T., Tsuchimori, M., Watanabe, O., and Kawata, Y., "Topographical nanostructure patterning on the surface of a thin film of polyurethane containing azobenzene moiety using the optical near field around polystyrene spheres", *Macromolecules,* **34**, 7471-7476, (2001).

44. Watanabe, O., Ikawa, T., Hasegawa, M., Tsuchimori, M., Kawata, Y., Egami, C., Sugihara, O., and Okamoto, N., "Transcription of near-field induced by photo-irradiation on a film of azo-containing urethane-urea copolymer", *Molecular Crystals and Liquid Crystals,* **345**, 629-634, (2000).

45. Ikawa, T., Mitsuoka, T., Hasegawa, M., Tsuchimori, M., Watanabe, O., and Kawata, Y., "Azobenzene polymer surface deformation due to the gradient force of the optical near field of monodispersed polystyrene spheres", *Physical Review B,* **64**, -, (2001).

46. Lu, Y., Theppakuttai, S., and Chen, S. C., "Marangoni effect in nanosphere-enhanced laser nanopatterning of silicon", *Applied Physics Letters,* **82**, 4143-4145, (2003).

47. Moreno, F., and Gonzalez, F., *Light Scattering from Microstructures* (Springer, 1998).

48. Munzer, H. J., Mosbacher, M., Bertsch, M., Zimmermann, J., Leiderer, P., and Boneberg, J., "Local held enhancement effects for nanostructuring of surfaces", *Journal of Microscopy-Oxford,* **202**, 129-135, (2001).

49. Watanabe, O., Ikawa, T., Hasegawa, M., Tsuchimori, M., and Kawata, Y., "Nanofabrication induced by near-field exposure from a nanosecond laser pulse", *Applied Physics Letters,* **79**, 1366-1368, (2001).

50. Fischer, U. C., and Zingsheim, H. P., "Sub-Microscopic Pattern Replication with Visible-Light", *Journal of Vacuum Science & Technology,* **19**, 881-885, (1981).

51. Morita, M., Matsumoto, M., Usui, S., Abe, T., Denkov, N., Velev, O., and Ivanov, I. B., "Interfacial Properties and Emulsion Stability in Fluorinated Oil Nonfluorinated Oil Surfactant(S) Systems", *Colloids and Surfaces,* **67**, 81-93, (1992).

52. Velev, O. D., Denkov, N. D., Paunov, V. N., Kralchevsky, P. A., and Nagayama, K., "Capillary Image Forces .2. Experiment", *Journal of Colloid and Interface Science,* **167**, 66-73, (1994).

53. Kralchevsky, P. A., Paunov, V. N., Denkov, N. D., and Nagayama, K., "Capillary Image Forces .1. Theory", *Journal of Colloid and Interface Science,* **167**, 47-65, (1994).

Chapter 4

1. Geiger, G., "Glass in Electronic Packaging Applications", *American Ceramic Society Bulletin,* **69**, 1131-&, (1990).

2. Illyefalvi-Vitez, Z., "Laser processing for microelectronics packaging applications", *Microelectronics Reliability,* **41**, 563-570, (2001).

3. Stuart, B. C., Feit, M. D., Rubenchik, A. M., Shore, B. W., and Perry, M. D., "Laser-Induced Damage in Dielectrics with Nanosecond to Subpicosecond Pulses", *Physical Review Letters,* **74**, 2248-2251, (1995).

4. Campbell, E. E. B., Ashkenasi, D., and Rosenfeld, A., "Ultra-short-pulse laser irradiation and ablation of dielectrics", *Lasers in Materials Science,* **301**, 123-144, (1999).

5. Mao, X. L., Mao, S. S., and Russo, R. E., "Imaging femtosecond laser-induced electronic excitation in glass", *Applied Physics Letters,* **82**, 697-699, (2003).

6. Davis, K. M., Miura, K., Sugimoto, N., and Hirao, K., "Writing waveguides in glass with a femtosecond laser", *Optics Letters,* **21**, 1729-1731, (1996).

7. Wang, J., Niino, H., and Yabe, A., "One-step microfabrication of fused silica by laser ablation of an organic solution", **68**, 111-113, (1999).

8. Zhou, G. S., Fauchet, P. M., and Siegman, A. E., "Growth of Spontaneous Periodic Surface-Structures on Solids During Laser Illumination", *Physical Review B,* **26**, 5366-5381, (1982).

9. Sipe, J. E., Young, J. F., Preston, J. S., and Vandriel, H. M., "Laser-Induced Periodic Surface-Structure .1. Theory", *Physical Review B,* **27**, 1141-1154, (1983).

10. Leamy, H. J., Rozgonyi, G. A., Sheng, T. T., and Celler, G. K., "Periodic Regrowth Phenomena Produced by Laser Annealing of Ion-Implanted Silicon", *Applied Physics Letters,* **32**, 535-537, (1978).

11. Tsukada, N., Sugata, S., Saitoh, H., and Mita, Y., "Surface Ripples in Laser-Photochemical Wet Etching of Gallium-Arsenide", *Applied Physics Letters,* **43**, 189-191, (1983).

12. Tsukada, N., Sugata, S., and Mita, Y., "New Experimental-Evidence of Surface Ripples on Gallium-Arsenide in Laser Annealing", *Applied Physics Letters,* **42**, 424-426, (1983).

13. Brueck, S. R. J., and Ehrlich, D. J., "Stimulated Surface-Plasma-Wave Scattering and Growth of a Periodic Structure in Laser-Photodeposited Metal-Films", *Physical Review Letters,* **48**, 1678-1681, (1982).

14. Osgood, R. M., and Ehrlich, D. J., "Optically Induced Microstructures in Laser-Photodeposited Metal-Films", *Optics Letters,* **7**, 385-387, (1982).

15. Jain, A. K., Kulkarni, V. N., Sood, D. K., and Uppal, J. S., "Periodic Surface Ripples in Laser-Treated Aluminum and Their Use to Determine Absorbed Power", *Journal of Applied Physics,* **52**, 4882-4884, (1981).

16. Maracas, G. N., Harris, G. L., Lee, C. A., and Mcfarlane, R. A., "Origin of Periodic Surface-Structure of Laser-Annealed Semiconductors", *Applied Physics Letters,* **33**, 453-455, (1978).

17. Young, J. F., Sipe, J. E., and Vandriel, H. M., "Regimes of Laser-Induced Periodic Surface-Structure on Germanium - Radiation Remnants and Surface-Plasmons", *Optics Letters,* **8**, 431-433, (1983).

18. Vanvechten, J. A., "Experimental Tests for Boson Condensation and Superconductivity in Semiconductors During Pulsed-Beam Annealing", *Solid State Communications,* **39**, 1285-1291, (1981).

19. Soileau, M. J., "Ripple Structures Associated with Ordered Surface-Defects in Dielectrics", *Ieee Journal of Quantum Electronics,* **20**, 464-467, (1984).

20. Temple, P. A., and Soileau, M. J., "Polarization Charge Model for Laser-Induced Ripple Patterns in Dielectric Materials", *Ieee Journal of Quantum Electronics,* **17**, 2067-2072, (1981).

21. Cline, H. E., and Anthony, T. R., "Non-Equilibrium Morphology of Liquid Inclusions Migrating in Solids", *Journal of Applied Physics,* **48**, 5096-5104, (1977).

22. Anthony, T. R., and Cline, H. E., "Surface Rippling Induced by Surface-Tension Gradients During Laser Surface Melting and Alloying", *Journal of Applied Physics,* **48**, 3888-3894, (1977).

23. Emelyanov, V. I., Konov, V. I., Tokarev, V. N., and Seminogov, V. N., "Formation of Periodic Surface Ripples under the Action of Pulsed Carbon-Dioxide Laser-Radiation on Fused-Silica", *Journal of the Optical Society of America B-Optical Physics,* **6**, 104-114, (1989).

24. Wilson, R. J., and Houle, F. A., "Composition, Structure, and Electric-Field Variations in Photodeposition", *Physical Review Letters,* **55**, 2184-2187, (1985).

25. Ehrlich, D. J., and Brueck, S. R. J., "Laser Photochemical Fabrication of Phase-Controlled 160-Nm Period Gratings by Stimulated 2nd-Order Surface Plasma-Wave Scattering", *Applied Physics Letters,* **47**, 216-218, (1985).

26. Mosbacher, M., Chaoui, N., Siegel, J., Dobler, V., Solis, J., Boneberg, J., Afonso, C. N., and Leiderer, P., "A comparison of ns and ps steam laser cleaning of Si surfaces", *Applied Physics a-Materials Science & Processing,* **69**, S331-S334, (1999).

27. Young, J. F., Sipe, J. E., Preston, J. S., and Vandriel, H. M., "Laser-Induced Periodic Surface Damage and Radiation Remnants", *Applied Physics Letters,* **41**, 261-264, (1982).

28. Dickinson, J. T., Shin, J. J., and Langford, S. C., "The role of defects in laser induced positive ion emission from ionic crystals", *Applied Surface Science,* **96-8**, 316-320, (1996).

29. Dickinson, J. T., Shin, J. J., and Langford, S. C., "Laser-induced emission of neutral atoms and molecules from electron-irradiated NaNO3", *Applied Surface Science,* **96-8**, 326-331, (1996).

30. Ashkenasi, D., Varel, H., Rosenfeld, A., Noack, F., and Campbell, E. E. B., "Pulse-width influence on the laser-induced structuring of CaF2 (111)", *Applied Physics a-Materials Science & Processing,* **63**, 103-107, (1996).

31. Varel, H., Ashkenasi, D., Rosenfeld, A., Herrmann, R., Noack, F., and Campbell, E. E. B., "Laser-induced damage in SiO_2 and CaF2 with picosecond and femtosecond laser pulses", *Applied Physics a-Materials Science & Processing,* **62**, 293-294, (1996).

32. Soileau, M. J., Vanstryland, E. W., and Williams, W. E., "Laser-Light Induced Bulk Damage to Optics", *Proceedings of the Society of Photo-Optical Instrumentation Engineers,* **541**, 110-122, (1985).

33. Soileau, M. J., Williams, W. E., Mansour, N., and Vanstryland, E. W., "Laser-Induced Damage and the Role of Self-Focusing", *Optical Engineering,* **28**, 1133-1144, (1989).

34. Bloembergen, N., "Light Waves Interact - a Citation-Classic Commentary on Interactions between Light Waves in a Nonlinear Dielectric by Armstrong,J.A., Bloembergen,N., Ducuing,J. And Pershan,P.S." *Current Contents/Engineering Technology & Applied Sciences,* 10-10, (1991).

35. Costache, F., Henyk, M., and Reif, J., "Modification of dielectric surfaces with ultra-short laser pulses", *Applied Surface Science,* **186**, 352-357, (2002).

36. Reif, J., Costache, F., Henyk, M., and Pandelov, S. V., "Ripples revisited: non-classical morphology at the bottom of femtosecond laser ablation craters in transparent dielectrics", *Applied Surface Science,* **197**, 891-895, (2002).

37. Costache, F., Henyk, M., and Reif, J., "Surface patterning on insulators upon femtosecond laser ablation", *Applied Surface Science,* **208**, 486-491, (2003).

38. Leiderer, P., Mosbacher, M., Boneberg, J., Bartels, C., Lang, F., Afonso, C., and Baeuerle, D., "Investigation of particle removal from silicon surfaces by means of dry and steam laser cleaning", *Ultra Clean Processing of Silicon Surfaces V,* **92**, 133-134, (2003).

39. Munzer, H. J., Mosbacher, M., Bertsch, M., Zimmermann, J., Leiderer, P., and Boneberg, J., "Local held enhancement effects for nanostructuring of surfaces", *Journal of Microscopy-Oxford,* **202**, 129-135, (2001).

40. Mosbacher, M., Munzer, H. J., Zimmermann, J., Solis, J., Boneberg, J., and Leiderer, P., "Optical field enhancement effects in laser-assisted particle removal", *Applied Physics a-Materials Science & Processing,* **72**, 41-44, (2001).

41. Fourrier, T., Schrems, G., Muhlberger, T., Heitz, J., Arnold, N., Bauerle, D., Mosbacher, M., Boneberg, J., and Leiderer, P., "Laser cleaning of polymer surfaces", *Applied Physics a-Materials Science & Processing,* **72**, 1-6, (2001).

42. Crisp, M. D., Boling, N. L., and Dube, G., "Importance of Fresnel reflections in laser surface damage of transparent dielectrics", *Applied Physics Letters,* **21**, 364-366, (1972).

Chapter 5

1. Klar, T.A., Perner, M., Grosse, S., Plessen, G., Spirkl, W., and Feldmann, J., "Surface-plasmon resonances in single metallic particles", *Physical Review Letters* **80,** 4249-4252 (1998).

2. Raether, H., *Surface plasmons*, Springer, Berlin, 1988.

3. Hutter, E., and Fendler, H., "Exploitation of localized surface plasmon resonance", *Advanced Materials*, **16,** 1685-1706, (2004).

4. Sambles, J.R., Bradbery, G.W., and Yang, F., "Optical excitation of surface plasmons: an introduction", *Contemporary physics*, **32,** 173-183, (1991).

5. Murray, W.A., Astilean, S., Barnes, W.L., "Transition from localized surface plasmon resonance to extended surface plasmon-polariton as metallic nanoparticles merge to form a periodic hole array ", *Physical Review B*, **69,** 165407/1-7, (2004).

6. Grand, J., de la Chapelle, M.L., Bijeon, J.-L., Adam, P.-M., Vial, A., Royer, P., "Role of localized surface plasmons in surface-enhanced Raman scattering of shape-controlled metallic particles in regular arrays ", *Physical Review B*, **72,** 33407/1-4, (2005).

7. Sonnichsen, C., *Plasmons in metal nanostructures*, in *Department of Physics*. 2001, Ludwig-Maximilians-University of Munich: Munich.

8. Sönnichsen, C., Franzl, T.,Wilk, T., von Plessen, D., and Feldmann J., "Drastic reduction of plasmon damping in gold nanorods", *Physical Review Letters*, **88,** 077404/1-4, (2002).

9. Boyd, G.T., Yu, Z.H., and Shen, Y.R., "Photoinduced luminescence from the noble metals and its enhancement on roughened surfaces", *Physical Review B*, **33,** 7923-7935, (1986).

10. Mohamed, M.B., Volkov, V., Link, S., and El-Sayad, M.A., "The 'lightning' gold nanorods: fluorescence enhancement of over a million compared to the gold metal", *Chemical Physics Letters*, **317,** 517-523, (2000).

11. Wilcoxon, J.P., Martin, J.E., Parsapour, F., Wiedenman, B., and Kelley, D.F., "Photoluminescence from nanosize gold clusters", *Journal of Chemical Physics*, **108,** 9137-9143.

12. Liedberg, B., Nylander, C., Lundstrom, I., "Surface plasmon resonance for gas detection and biosensing", *Sensors and Actuators* **4,** 299-304, (1983).

13. Yuk, J.S., Jung, J.W., Jung, S.H., Hong, D., Han, J.A., Kim, Y.M., Ha, K.S., "Analysis of protein interactions on protein arrays by a wavelength interrogation-based surface plasmon resonance biosensor", *Proteomics*, **4,** 3468-3476, (2004).

14. Zhavnerko, G., Ha, K.S. Biosensor applications: surface engineering. In:. in *Encyclopedia of Nanoscience and Nanotechnology*. 2004: Marcel Dekker

15. Myszka, D.G., Rich, R.L., "Implementing surface plasmon resonance biosensors in drug discovery", *Pharmaceutical Science and Technology Today* **310-317**, (2000).

16. He, L., Musick, M.D., Nicewarner, S.R., Salinas, F.G., Benkovic, S.J., Natan, M.J., and Keating, C.D., "Colloidal Au-enhanced surface plasmon resonance for

ultrasensitive detection of DNA hybridization", *Journal of the American Chemical Society*, **122,** 9071–9077, (2000).

17. Yu, C.Y., Chen, L.L., Luo, H.B., Chen, J., Cheng, F., Gui, C.S., Zhang, R.H., Shen, J.H., Chen, K.X., Jiang, H.L., and Shen, X., "Binding analyses between human PPAR {gamma}-LBD and ligands - surface plasmon resonance biosensor assay correlating with circular dichroic spectroscopy determination and molecular docking", *European Journal of Biochemistry*, **271,** 386–397, (2004).

18. Shannessy, D.J., Brighamburke, M., Soneson, K.K., Hensley, P., and Brooks, I. , "Determination of rate and equilibrium binding constants for macromolecular interactions using surface plasmon resonance - use of nonlinear least squares analysis methods", *Analytical Biochemistry*, **212,** 457–468, (1993).

19. Moskovits, M., "Surface-enhanced spectroscopy", *Review of Modern Physics*, **57,** 783, (1985).

20. Kneipp, K., Wang, Y., Kneipp, H., Itzkan, I., Dasari, R.R., and Feld, M. S., "Population pumping of excited vibrational states by spontaneous surface-enhanced Raman scattering", *Physical Review Letters*, **76,** 2444, (1996).

21. Nie, S.a.E., S.R., "Probing single molecules and single nanoparticles by surface enhanced Raman scattering", *Science*, **275,** 1102, (1997).

22. Shalaev, V., *Nonlinear Optics of Random Media: Fractal Composites and Metal-Dielectric Films*, Springer, Berlin, 2000.

23. Krenn, J., Wolf, R., Leitner, A., and Aussenegg, F., "Near-field optical imaging the surface plasmon fields of lithographically designed nanostructures", *Optics Communications*, **137,** 46, (1997).

24. Maier, S.A., Barclay,P.E., Johnson, T.J., Friedman, M.D., and Painter, O.A.P.L., 071103 (2005). "Experimental demonstration of fiber-accessible metal nanoparticle plasmon waveguides for planar energy guiding and sensing", *Applied Physics Letters*, **86**, (2005).

25. Bozhevolnyi, S.I., Volkov, V.S., Devaux, E., Ebbesen, T.W., "Channel plasmon-polariton guiding by subwavelength metal grooves", *Physical Review Letters*, **95,** 046802/1-4, (2005).

26. Weeber, J.C., Krenn, J.R., Dereux, A., Lamprecht, B., Lacroute, Y., Goudonnet, J.P., "Near-field observation of surface plasmon polariton propagation on thin metal stripes", *Physical Review B*, **64,** 045411/1-9, (2001).

27. Krenn, J.R., Lamprecht, B., Ditlbacher, H., Schider, G., Salerno, M., Leitner, A., Aussenegg, F.R., "Non-diffraction-limited light transport by gold nanowires", *Europhysics Letters*, **60,** 663-669, (2002).

28. Ditlbacher, H., Krenn, J.R., Schider, G., Leitner, A., Aussenegg, F.R., "Two-dimensional optics with surface plasmon polaritons", *Applied Physics Letters*, **81,** 1762-1764, (2002).

29. Bozhevolnyi, S.I., Volkov, V.S., Leosson, K., Boltasseva, A., "Bend loss in surface plasmon polariton band-gap structures", *Applied Physics Letters*, **79,** 1076-1078, (2001).

30. Luoa, X., and Ishihara, T., "Surface plasmon resonant interference nanolithography technique", *Applied Physics Letters*, **84,** 4780-4782, (2004).

31. Srituravanich, W., Fang, N., Sun, C., Luo, Q., and Zhang, X., "Plasmonic Nanolithography", *Nano Letters*, **4,** 1085-1088, (2004).

32. Kik, P.G., Maier, S.A., Atwater, H.A. Plasmon printing - a new approach to near-field lithography. in *Nanopatterning - From Ultralarge-Scale Integration to Biotechnology. Symposium (Materials Research Society Symposium Proceedings)*. 2002.

Vita

Senthil Prakash Theppakuttai Komaraswamy was born on 30th May 1977 in Salem, India; the first son of Mr. Komaraswamy and Mrs. Nalina. He received his Bachelor of Science (Mechanical Engineering) from The National Institute of Technology, Jamshedpur, India in 1998. He earned his Master of Science (Industrial Engineering) from Iowa State University in 2001.

Since 2002 Senthil Theppakuttai has pursued his Doctorate in Mechanical Engineering under the guidance of Dr. Shaochen Chen at The University of Texas at Austin. His research focused on overcoming the diffraction limit of light for the application of lasers in nanomanufacturing.

Permanent address: 226/146, EB Engineers Colony II,
Alagapuram Kattur,
Salem, Tamil Nadu – 636016
India

This dissertation was typed by the author.